SPECTRAL PHASE SHAPING FOR NON-LINEAR SPECTROSCOPY AND IMAGING

Sytse Postma

Promotiecommissie

Voorzitter	prof. dr. W. J. Briels
Promotor	prof. dr. J. L. Herek
Assistent Promotor	dr. ir. H. L. Offerhaus
Overige leden	prof. dr. K. J. Boller
	prof. dr. N. F. van Hulst
	prof. dr. W. van der Zande
	prof. dr. ir. H. J. W. Zandvliet
Paranimfen	ir. R. V. A. van Loon
	ir. W. H. Peeters

Cover design: F. Muijzer

SPECTRAL PHASE SHAPING FOR NON-LINEAR SPECTROSCOPY AND IMAGING

PROEFSCHRIFT

ter verkrijging van
de graad van doctor aan de Universiteit Twente,
op gezag van de rector magnificus,
prof. dr. W. H. M. Zijm,
volgens besluit van het College voor Promoties
in het openbaar te verdedigen
op donderdag 11 september 2008 om 15.00 uur

door

Sytse Postma

geboren op 10 januari 1980
te Apeldoorn

Dit proefschrift is goedgekeurd door:

 prof. dr. J. L. Herek (promotor)
 dr. ir. H. L. Offerhaus (assistent promotor)

Contents

Chapter 1

Introduction

1.1 Introduction to this thesis

There is a historic interest in understanding the way organisms function. Since the first practical microscope was built by Antoni van Leeuwenhoek (around 1660), information was collected about single cell organisms, muscle fibers, red blood cells, yeast plants, and much more. Throughout the following centuries, the improvement of lenses yielded more precise optical images. Nowadays, with electron beam imaging, even nanometer resolution is achieved from which the structure of dried cells has been established in great detail.

Most optical imaging is based on scattering by refractive index changes or on absorption. For a better understanding of processes occurring in a cell, chemical selective images of cells are required. Chemically selective imaging can be based on labeling the molecules of interest with fluorescent dyes. Unfortunately these dyes are often large and sometimes toxic. Another possibility is based on the vibrational frequencies of the molecule itself, which is inherently molecule specific and requires no labeling.

As early as 1928, it was established experimentally that materials emit red-shifted light when they are illuminated [1]. Later, this process was called Raman scattering after the experimental pioneer. Conventional incoherent light sources and the detection with photographic plates confined Raman spectroscopy to materials with a relatively high Raman cross-section. Since the invention of the laser in 1960, Raman spectroscopy has become applicable to more systems. Two disadvantages of the Raman process are that it can be overwhelmed by fluorescence, and that it has a low cross-section. The Raman process can be stimulated by applying two lasers with a frequency difference matching the vibrational energy [2]. This process is

called Stimulated Raman and is the basis for Coherent Anti-Stokes Raman Scattering (CARS).

To analyze an unknown substance through CARS, the difference frequency must be scanned and the measured CARS signal must be compared to known molecular spectra (also referred to as molecular fingerprints). Traditionally this is done with pulses in the picoseconds range which had the advantage that the selectivity is high because only one vibration line (of one species) is addressed [3,4]. Instead of scanning the frequency difference it is also possible to apply all difference-frequencies at the same time using a broad excitation bandwidth. Several techniques have been developed to investigate molecular vibrational bands [5-11]. In a mixed sample, multiple vibrational resonances, possibly of multiple species, are generally located in the applied frequency range. For excitation of only one species the laser pulse has to be customized to excite only one specific species.

Femtosecond pulses can be manipulated in the spectral domain. Figure 1.1 shows a so-called 4f-configuration described by Weiner [12]. With this setup, a short laser pulse can be converted into an arbitrary shape in the time domain by changing properties of light in the spectral domain.
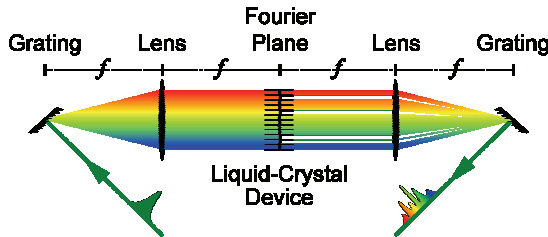
Figure 1.1: Schematic of a 4f spectral modulator with a liquid crystal device as active control element [13].

The manipulation can be done with holographic masks [14], electro-optic crystals [15], acousto-optic crystals [16], or liquid crystal spatial light modulators [12,17,18]. Due to the flexibility and the possibility to apply spectral phase shaping for laser sources with a high repetition rate (100 MHz), liquid crystal light modulators are often used for spectral phase shaping. One or more liquid crystal devices are used to control the amplitude, phase, and/or polarization. Many of the modulators currently in use are quite large; ~6 cm for 640 separate pixels, which requires a large distance to spread the spectrum of the pulse over the pixels. As such, the entire spectral pulse shaping setup often has a footprint of more than 2000 cm^2 even for a folded arrangement [19-21]. In this way a highly compact spectral phase shaper setup of only 70 cm^2 is designed, built and tested. The setup contains a small, high-resolution one-dimensional liquid-

crystal modulator with 4096 pixels spread over 7.4 mm and 600 effective addressable elements (degrees of freedom). The spectral phase shaping setup is compressed to the point where the monochromatic spot size is comparable to the size of the effective addressable elements.

This thesis treats a new method for chemical identification based on a spectral phase shaping technique. Such control of the interaction of laser pulses with molecules could find application for analytical methods for chemical identification One example may be to detect differences in the folding of proteins. The concept involves the design of smart phase profiles that identify specific species or states according to the vibrational fingerprint of the species. If this detection succeeds, it can be used for diagnosis of prion-based diseases in mammals [22], such as Bovine Spongiform Encephalopathy (BSE) in cattle and Creutzfeldt-Jakob disease in humans. First steps towards CARS spectroscopy and microscopy in the vibrational region, where proteins can be identified ($330 - 1500$ cm^{-1} [23]), are described in this thesis.

The following four steps have been realized:
1. Design and realization of a spectral phase shaper with a bandwidth of 60 THz as well as the evaluation of several calibration methods.
2. Two-photon fluorescence experiments. These experiments show that not only the absolute amplitude of the second harmonic field, but that also the phase is of importance for the two-photon fluorescence yield.
3. CARS spectroscopy in the vibrational region around 3000 cm^{-1}. The experiments served to achieve the first insights into CARS with shaped spectral phase. A method to perform spectroscopy on integrated CARS signals is presented.
4. CARS microscopy with shaped pulses based on integrated CARS signals.

The following three sections will introduce the subjects of two-photon fluorescence, CARS spectroscopy, and CARS imaging.

1.2 Two-photon fluorescence

Multi-photon interactions are of wide interest since the invention of mode-locked laser sources provided access to the necessary (peak) intensities [24]. Microscopy based on multi-photon effects has the advantage that the measured images are inherently confocal, which eliminates the need for a pinhole used in single-photon fluorescence [25]. With a spectral phase

shaper, it is possible to selectively excite fluorescent probe molecules by amplitude shaping of the calculated spectral second harmonic intensity [26]. Here, the spectral phase of the fundamental field is shaped such that the calculated second harmonic spectrum overlaps more efficiently with the absorption band of one fluorescent probe than with that of another fluorescent probe.

It is shown that both the amplitude of the second harmonic field and the phase are of importance for the yield of two-photon fluorescence processes. Furthermore, our measurements indicate that it is possible to enhance the two-photon fluorescence yield compared to excitation by a transform limited pulse. When intermediate resonances are present, the possibility of enhancement of the two-photon fluorescence yield above the yield for transform limited pulses has previously been shown by Silberberg and co-workers [27]. In contrast this enhancement is shown for the case where no intermediate molecular resonances are present in the target emitters.

1.3 CARS spectroscopy

CARS has been used successfully for spectroscopy and microscopy since the development of (tunable) pulsed laser sources [2,28,29]. In CARS, molecular vibrations are excited coherently by the pump (ω_p) and Stokes (ω_s) pulses. Subsequently a probe (ω_{pr}) pulse, which is often derived from the same pulse as the pump, generates the anti-Stokes (ω_c), i.e. CARS, signal ($\omega_c = \omega_p - \omega_s + \omega_{pr}$).

In figure 1.2 four methods (a-d) are presented that all induce the CARS effect:

(a) A CARS spectrum can be measured using narrowband laser sources (~ 1 cm^{-1}) and subsequently tuning the difference frequency between the pump and Stokes pulses ($\omega_p - \omega_s$) [3,4,30].

(b) A more direct way to obtain a CARS spectrum is multiplex CARS, with a broadband (~ 500 cm^{-1}) Stokes pulse. In this method, the CARS signal is measured on a spectrometer [31-34].

(c) Single pulse CARS, where ω_p, ω_s, and ω_{pr} are all part of the same broadband pulse, has also been investigated in conjunction with spectral phase and amplitude shaping [5-11]. In practice, this technique reaches only vibrational frequencies below 1500 cm^{-1}.

(d) A fourth scheme involves spectrally shaped broadband pump and probe pulses, in combination with an independent narrowband Stokes pulse. With this doubly-shaped pulse scheme, a new phase shaping strategy that enables extraction of the frequencies, the bandwidths and the relative cross-sections of vibrational lines is presented in this thesis.

The resonant CARS signal is always accompanied by an inherent non-resonant background such as depicted in figure 1.2(e) for scheme (d).
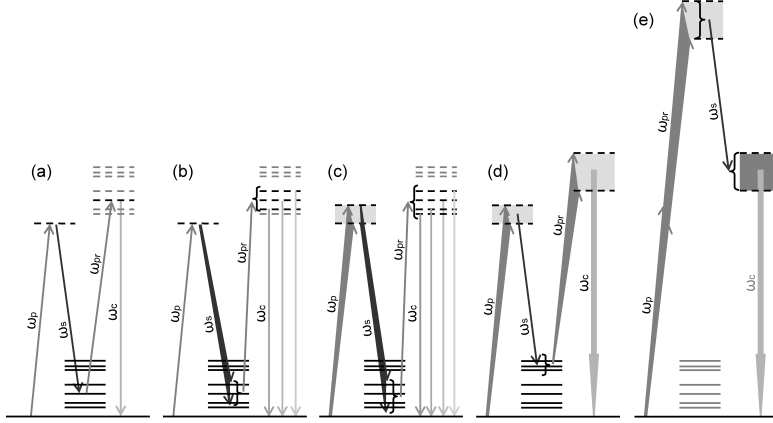

Figure 1.2: CARS energy schemes a) Narrowband CARS, b) Multiplex CARS, c) Pump and Stokes broad, d) Pump and probe broad, e) Non-resonant energy scheme.

The experiment combines a tunable broadband Ti:Sapphire laser, synchronized to a ps-Nd:YVO mode-locked laser, and a high resolution spectral phase shaper are employed. This method allows for spectroscopy of vibrational resonances with a precision better than 1 cm^{-1} for isolated lines in the high vibrational resonance frequency region around 3000 cm^{-1}. In this spectral region, strong and separated O-H, C-H, and N-H lines are located, which facilitates the demonstration of the technique. Furthermore, a scheme to reject the non-resonant CARS signal from materials that have no resonances in the frequency range covered by the pump minus Stokes spectra is presented. A demonstration is given of spectroscopy and microscopy on the integrated spectral response.

1.4 CARS imaging

CARS techniques for imaging of biological samples have already been established [28,33,35-37]. The combination of vibrational spectroscopy and nonlinear microscopy provides a direct technique to localize and identify the structures of different chemical compositions [28]. In this thesis, a method is presented to obtain chemical selectivity using broadband pump and probe pulses that are spectrally phase shaped. The Stokes pulse, in contrast, has a narrow bandwidth.

Imaging with sub-100 fs laser pulses has several drawbacks. The first drawback is multi-photon-induced damage, due to high peak intensities [38].

The second drawback is the inherent non-resonant background, which accompanies the resonant CARS signal [39]. Spectral phase shaping reduces the first drawback, because it lowers the peak intensity. The second drawback can also be tackled with spectral phase shaping. For pure non-resonant materials in the vibrational region under investigation, this non-resonant signal can be completely suppressed.

We demonstrate chemically selective imaging of polystyrene (PS) and polymethylmethacrylate (PMMA) beads. With the aid of the spectral phase shaper, images based on CARS signals generated in PS and PMMA beads are obtained for two profiles, which differ only in the sign of the spectral phase. The difference between these images shows a clear contrast for the beads of choice. We also give an outlook regarding the use of phase profiles incorporating the complete molecular response profile.

1.5 Thesis outline

This thesis describes the development of a spectral phase shaper for novel non-linear spectroscopy and imaging.

Chapter 2 discusses the design choices, realization, and calibration of the spectral phase shaper setup. Two methods to measure the shaped pulses are discussed.

Chapter 3 shows two-photon fluorescence experiments performed on various samples. The shown results indicate an enhancement of the two-photon fluorescence relative to the two-photon fluorescence response for a transform limited pulse. These measurements also show that the phase of the second harmonic field is of importance for the two photon fluorescence process.

Chapter 4 discusses spectral phase shaped CARS spectroscopy. Theory and experiments based on spectral phase shaped pump and probe pulses are presented. The experiments indicate that a resolution better than 1 cm^{-1} is possible with the setup and the method used. Also a technique is described for locking two independent mode-locked laser sources, with a jitter of only 60 fs rms for a bandwidth of 0.04 to 100 Hz. Next, high resolution CARS spectroscopy on the integrated spectral response is shown. Furthermore, a scheme is presented to remove the non-resonant background generated in non-resonant materials.

Chapter 5 discusses spectral phase shaped CARS imaging and shows that the techniques presented in this thesis are capable of selectively imaging different materials, based on the chemical composition of the materials. The expected imaging contrast is calculated for phase profiles that incorporate the vibrational spectrum of the molecules of interest.

Chapter 2

Compact high-resolution spectral phase shaper

2.1 Introduction

Manipulation of femtosecond laser pulses is an active field of research. Applications include coherent control of energy transfer in molecules [40], selective Raman spectroscopy and microscopy [26,41], separation and detection of isotopes and molecules [42], probing of femtosecond structural dynamics of macromolecules [43,44] and coherent laser control of physicochemical processes [45-48].

Shaping of femtosecond pulses can not be accomplished in the time domain because there are as yet no electronic modulators available that operate in the range of 100 to 1000 THz. Therefore femtosecond pulses are manipulated in the spectral frame. Manipulation can be achieved using holographic masks [14], electro-optic [15], acousto-optic [16], or liquid crystal spatial light modulators (SLM) [12,17,21]. In the latter method the modulator is placed at the plane where the spectrum of the pulse is spatially imaged [49]. Many of the modulators currently in use are quite large, e.g. ~6 cm for 640 separate pixels, which requires a certain distance to spread the spectrum of the pulse over the electrodes. As such, the entire spectral pulse shaping setup requires often more than 2000 cm^2, even for a folded arrangement [19-21]. In contrast, this chapter presents details of the design, building and testing of a highly compact setup of 70 cm^2, containing a small high-resolution one-dimensional liquid-crystal modulator (LCM) with 4096 pixels spread over 7.4 mm.

This chapter explains the design choices for the spectral phase shaper (2.2), provides a short explanation of the type of liquid crystals used in SLMs, the

operation of the liquid crystal device (LCD) (2.3), and the calibration of the LCD (2.4). Methods to calibrate the frequency spread over the pixels are discussed (2.5). A variant on the Frequency Resolved Optical Gating (FROG) technique, used to measure the amplitude and phase profile of the shaped pulses, is developed and discussed (2.6). The method used to generate pulses with a flat spectral phase profile at a specific location in the experiments is explained (2.7).

2.2 Design justification

The type of experiments conceived for this design involve controlling the spectral phase of pump and probe pulses for Coherent Anti-Stokes Raman Scattering (CARS) spectroscopy and microscopy in the fingerprint region of proteins (330 – 1500 cm^{-1} [23]). The ultimate goal is the identification of the folding of proteins, which can be used for diagnosis of prion based diseases [22]. Two examples of these kinds of diseases are Bovine Spongiform Encephalopathy (BSE) in cattle and Creutzfeldt-Jakob disease (CJD) in humans.

2.2.1 Design considerations

The considerations used for the design of the spectral phase shaper setup are as follows:

1. The difference frequency between the pump and Stokes laser beam should cover a range of 1170 cm^{-1} (35 THz), resulting in a spectral intensity FWHM of 30 THz for the pump pulses.
2. No more than 2.5% of the energy of the laser pulses may remain unaffected by the spectral phase shaper. For an intensity spectrum with a FWHM of 30 THz this requirement means that at least 60 THz of the spectrum of the pump and probe laser pulses should be controlled.
3. The required resolution is 4 cm^{-1} (0.12 THz).
4. The peak power should be less than 1 MW for the imaging in order to prevent damage [39].
5. For real time imaging, with a certain phase profile applied to the pump and probe pulses, of a movie of 256 X 256 pixels and 15 frames per second, processing of about a million pixels per second is required. This requirement leads to a minimum repetition rate of the laser source of 1 MHz.
6. A small spectral phase shaper setup is preferred.
7. Components are preferably commercially available.

8. The laser source for the shaped light pulse is centered at a wavelength of 800 nm.

2.2.2 Choice of light modulator

Considerations 2, 3, 5, 6, and 7 are considerations that influence the choice for the light modulator. Considerations 2 and 3 enforce a minimum requirement of 500 degrees of freedom on the shaper. From consideration 5 it can be concluded that the pattern formed by the light modulator should be stable for time scales up to a second or that it should be refreshed for every laser pulse. The refresh rate of the spectral phase profile should be at least 1 MHz if the phase profiles have to refresh for each pulse. Commercially available AOMs and EOMs have refresh rates on the order of 100 kHz [12]. If it is not possible to update the required pattern for each pulse at the MHz repetition rate of a laser source, the pattern should remain on the device without degradation, which is not the case for AOMs and EOMs. In case of holographic masks the pattern can be kept stable for the required measurement time, however for each different experiment a new mask is required. LCDs have the advantage that patterns can be programmed onto the LCD and remain stable until a new pattern is applied. Therefore an LCD has been chosen as active element to control the spectral phase. Many of the modulator setups currently in use are quite large (~6 cm for 640 separate pixels) [22]. Here, consideration 6 in combination with the requirement of a minimum of 500 degrees of freedom led to the choice of an LCD with 4096 electrodes spread over 7.4 mm. The chosen device is reflective, which negates the need for a second pair of dispersive and focusing elements. It is mentioned in the specifications of this device that, due to electric field crosstalk, the number of degrees of freedom is 600. These specifications lead to the conclusion that this LCD is in compliance with the stated considerations.

The chosen LCD places the following extra considerations on the choice of the focusing element and the dispersive element:

1. the size of the LCD is 6 mm by 7.4 mm (x, y),
2. the outer dimensions are 55 mm by 39 mm (x, y),
3. the pixels are along the longest direction (y),
4. the damage threshold is 5 W/cm^2,
5. the maximum phase retardation is 10 rad.

2.2.3 Choice of focusing element

To spatially map the different directions of the light onto the LCD, a lens or a curved mirror is required. The focusing element maps each direction to a

position with a defined monochromatic spot size on the LCD. To define a maximum for the monochromic spot size it is assumed that the required 500 degrees of freedom translate to a feature size of 14.8 μm (7.4 mm/500) and that it is allowed to approximate the combination of the optical crosstalk source (due to the finite monochromatic spot size) and the electric field crosstalk in a Pythagorean way. The electric field crosstalk has, in this approximation, a feature size of 12.3 μm (7.4 mm/600). With this approximation a maximum of 8.2 μm for the monochromatic spot size is obtained. This spot size is chosen to be the e^{-2} intensity diameter. Here, the beam diameter is twice the distance from the beam axis to where the optical intensity drops to e^{-2} (≈13.5%) of the value on the beam axis. At this radius, the electric field strength drops to e^{-1} (≈37%) of the maximum value. A monochromatic *spherical* focal spot size of 8.2 μm would imply that the complete spectrum would be focused on $6.2 \cdot 10^{-4}$ cm^2 (8.2 μm · 7.4 mm). With the specified damage threshold of the LCD the maximum average laser power should be no larger than 3 mW in order not to exceed the damage threshold. The maximum permissible power can be increased by the use of a cylindrical lens or mirror, which generates a monochromatic focal line. The required focal distance, for a collimated entrance beam, can be calculated using equation 2.1 [52]:

$$f(\lambda) = \frac{\pi \cdot w_0 \cdot w_l}{4\lambda} ,$$ 2.1

where w_0 is the diameter in the focus where the intensity is e^{-2} of the maximum intensity, w_l is the diameter just before the focusing element where the intensity is e^{-2} of the maximum intensity, and λ is the wavelength. The e^{-2} intensity diameter from the laser is measured to be 2.5 mm, which is used here. For a wavelength of 800 nm this results in a focal distance of 20 mm.

A cylindrical lens or a cylindrical mirror can be used as the focusing element. The lens can be used on axis, but introduces dispersion and chromatic aberrations. The mirror is inherent achromatic but needs to be used at an angle which introduces coma and astigmatism. In order to make a choice the effects of these four points are discussed.

The first point is chromatic aberration. Chromatic aberrations in a lens cause different wavelengths to have different focal distances. Due to this effect the size of the beam in the liquid crystal layer varies as a function of wavelength. Secondly the different focal distances result in the reflected light from the LCD not being collimated by the lens for all wavelengths.

The focal distance for a plano-convex cylindrical lens can be described using equation 2.2 [50]:

$$f(\lambda) = \frac{R}{n(\lambda) - 1},$$

2.2

where R is the radius of curvature of the cylindrical lens and n is the refractive index which depends on the wavelength. The refractive index as function of wavelength can be described with a Sellmeier equation, which is given in equation 2.3 [51]:

$$n(\lambda) = \sqrt{A + \frac{B}{1 - \frac{C}{\lambda^2}} + \frac{D}{1 - \frac{E}{\lambda^2}}},$$

2.3

where λ is the wavelength in micrometers. The first and second terms represent, respectively, the contribution to refractive indices owing to higher-energy and lower-energy band gaps of electronic absorption whereas the last term accounts for a decrease in refractive indices owing to lattice absorption.

If, the liquid crystal layer is not located at the focal distance for all wavelengths, the intensity e^{-2} diameter of the beam at the interface with the liquid crystals and the HR layer can be calculated by [52]:

$$w_B(\lambda) = w_0(\lambda) \sqrt{1 + \left(\frac{f(\lambda) - f_c}{z_0(\lambda)}\right)^2},$$

2.4

where f_c is the focal distance of the central wavelength, w_0 is the e^{-2} diameter of the beam in the focus as in equation 2.1, and z_0 is the Rayleigh length of the focus, which is defined as follows:

$$z_0(\lambda) = \frac{\pi \cdot w_0^2(\lambda)}{4\lambda},$$

2.5

The divergence of the light for the different wavelengths after refocusing can be calculated with equation 2.6 [50]:

$$\Phi(\lambda) = \tan^{-1}\left(\frac{2f_c - 2f(\lambda)}{f_c \cdot f(\lambda) - f(\lambda)^2}\right),$$

2.6

Figure 2.1 shows the e^{-2} intensity beam diameter as a function of wavelength at three interfaces; the interface from the ITO layer to the liquid crystal layer, the interface of the liquid crystals to the high reflective dielectric

coating, and the interface between the liquid crystal layer to the ITO layer. Figure 2.10 shows a schematic diagram of the LCD, where the different interfaces are shown. The divergence of the beam after reflection and refocusing by the cylindrical lens is given on the right axis of figure 2.1. The calculations are done for a commercially available BK7 plano-convex lens with a curvature of 10.3 mm (as available from Thorlabs).
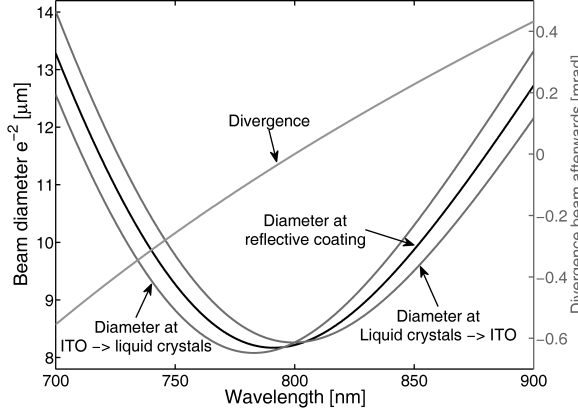

Figure 2.1: Focal size as a function of wavelength. The divergence of the reflected light after refocusing is given on the right.

The e^{-2} intensity beam diameter varies from 8 to 14 μm in the graph, which results in lower spectral resolution for off-center wavelengths in the designed spectrum. 94.4% of the energy of the specified laser pulse, defined by the design considerations 1 and 8 in section 2.2.1, is located between 750 and 850 nm, which correspond to an e^{-2} intensity beam diameter between 8 and 10 μm for 94.4% of the spectrum. The focal distance for the simulated lens at a wavelength of 900 nm is 20.236 mm. The focal distance of this lens at a wavelength of 700 nm is 20.076 mm. The difference in focal distance is hence 160 μm. Suppose the experiment is not placed close to the spectral phase shaper setup, but for example at 2 meter distance. The different divergence between the spectral parts of the laser pulse results in a different entrance diameter at the lens (or objective) at the location of the sample. The difference between the divergence for 750 and 850 nm is about 0.5 mrad. For an entrance beam diameter of 2.5 mm, the entrance diameter size for the focusing element for the experiment varies from 2 to 3 mm for wavelengths between 750 and 850 nm, resulting in the inverse ratio for the diameter of the beam in the focus at the experiment location according to equation 2.1. This issue complicates the understanding of experiments.

An achromatic lens, for example the AC080-020-B (Thorlabs), which is made from LAKN22 and SFL6, decreases the magnitude of these two problems; the maximum difference in focal length for the different

wavelengths in the region of 700 to 900 nm is 9 µm according to the specifications and the divergence after refocusing decreases approximately in the first order with the same factor, which gives a divergence difference for 750 and 850 nm of 30 µrad. This divergence means that after 2 meter of propagation, the diameter of the beam for the different colors has changed approximately 60 µm between 750 and 850 nm, which is small relative to the entrance beam diameter of 2.5 mm. In this case the beam diameters at the HR layer are dominated by the size of the wavelength. The achromatic aberration changes the beam diameter at the focus by approximately 1%; which is calculated with equation 2.4. The achromatic lens used in this example is spherical, but by ordering a custom made achromatic cylindrical lens this problem can be solved.

The second point is dispersion. The phase profiles used in the experiments should be based on a flat phase profile to have control of the actual phase in experiments. Therefore all dispersion in the setup should be compensated for. An extra lens creates extra dispersion; this dispersion can be compensated with the LCD if the dispersion does not exceed the maximum phase retardation of the LCD, which is 10 radians. Eventually 2π phase steps can be used to compensate large values of dispersion. The disadvantage of 2π phase steps is that due to crosstalk between pixels the phase step comes with a phase profile. A prism compressor can be used to compensate the first order dispersion. The remaining dispersion has to be compensated for by the LCD. If more dispersion must be compensated, a combination of a prism and grating compressor is able to compensate the first and second-order dispersion [53].
The focusing lens is not the only element which causes dispersion. Propagation through air, the output coupler of the laser, and the cover window of the LCD should also be taken into account. For this calculation the propagation length through air is taken as 5 m, 10 mm of propagation through BK7 glass is assumed for the output coupler and twice the cover window. Fused silica prisms are used for the prism pair, because this type of prism compressor adds a relatively low amount of second-order dispersion [54]. Three different cases for focusing the light onto the LCD are considered; a cylindrical lens of BK7 with a thickness of 3.3 mm, an achromatic cylindrical lens with an overall thickness of 3.6 mm (which is, for this example, equally divided between LAKN22 and SFL6), and a gold coated cylindrical mirror, which adds no extra dispersion. The Sellmeier equations for the glass types are taken from literature [51, 55], and the Edlen equation with its constants for calculating the refractive index of air is taken from literature [56]. The Edlen equation is based on resonances, just as the Sellmeier equations, with additions to take pressure, temperature and the gas

mixture into account. Here we use a temperature of 295 K, air pressure of 1.012 bar, hydrogen level of 40%, and a gas mixture consisting of N_2 (78,09%), O_2 (20.95%), Ar (0.93%), and CO_2 (0.03%).

Figure 2.2 shows the remaining phase (after subtracting the constant and linear spectral phase) for the three cases as function of wavelength that the LCD has to compensate, to get a flat phase profile. The calculations in figure 2.2 are for the case that the prism compressor is adjusted to compensate for all quadratic spectral phase contributions (first order dispersion). A constant spectral phase influences the field underlying the envelop of the pulse, the linear spectral phase shifts the pulse in time, and higher order spectral phase results in lower peak power of the pulse and longer time durations [53]. Therefore it is allowed to subtract the constant and linear spectral phase.
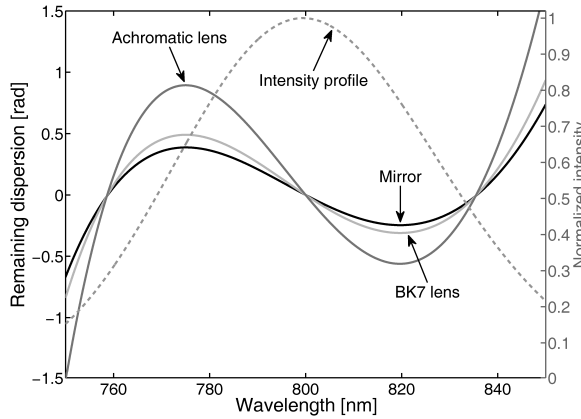

Figure 2.2: Remaining dispersion for three cases for focusing light on the LCD. The dashed line indicates the intensity profile of laser pulse from the design constraints.

The distances between the two prisms used in figure 2.2 are 648 mm for the mirror, 819 mm for the cylindrical BK7 lens, and 1597 mm for the achromatic lens. 5.5% of the energy of the laser pulse specified from the design constraints falls outside of this graph. For the center part only 2.5 rad phase shift from the total range of 10 rad on the LCD is required to compensate for the dispersion. In the case of the BK7 lens even less compensation is required.

The third point is astigmatism. The off-axis incidence on a cylindrical mirror results in an elliptical focus. The dimensions of the casing of the LCD (55·38 mm^2) limit the possibilities for a small angle of incidence on the cylindrical mirror. Figure 2.3 shows the actual size of the LCD with its case combined with a cylindrical mirror and a unspecified dispersive element, the chosen focal distances are 20 mm and 50 mm. The choice of the dispersive element is discussed in section 2.2.4.
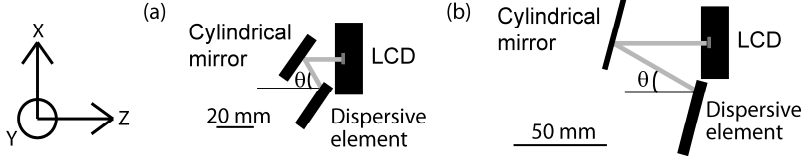
Figure 2.3: Schematic of the LCD for two layouts: A) Where the focal distance is 20 mm (θ = 70º). B) Where the focal distance is 50 mm (θ = 30º).

One result of the non normal incidence on the cylindrical mirror is a larger focal distance which is described by the following equation [57]:

$$f_{eff} = \frac{f}{\cos \frac{1}{2} \theta},$$
<div align="right">2.7</div>

where θ equals twice the angle of incidence on the curved mirror (indicated in figure 2.3), and f is the designed focal distance (figure 2.3). Due to the small distances (20 mm) between the components, where a laser beam with an e^{-2} intensity diameter of 2.5 mm has to be directed, the angle θ is in the order of 70º. Astigmatism increases the focal distance, but this increase is constant and for 70º the effective focal distance is 1.22 times the focal distance for normal incidence. This effect can compensated for, according to equation 2.1, with a smaller focal distance for non normal incidence or a bigger entrance beam diameter to achieve the same size for the monochromatic focal spot. Figure 2.3 shows a possible layout for a focal distance of 50 mm and a θ of 30º. In that case the focal distance is increased with 1.035 times the focal distance for normal incidence. Non normal incidence on a cylindrical mirror causes also coma which is the fourth point. Figure 2.4 shows a schematic graph indicating the reason behind coma.
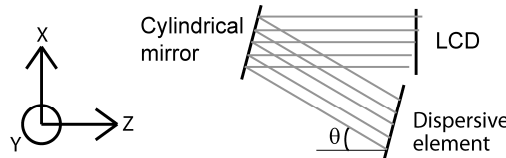

Figure 2.4: Illustration of coma caused by non normal incidence to a cylindrical mirror. All lines have the same length. The focusing and spatial spreading of the spectrum occurs in the y-direction. Note that this figure is not exaggerated.

The optimal position for the LCD is where the high reflective dielectric layer is placed at the focal distance of the cylindrical mirror for the center of the beam (highest intensity). The e^{-2} diameter of the beam at the liquid crystal layer depends on the wavelength and the difference between the focal point and the liquid crystal layer which depends on the spatial position of the beam in the x-direction as indicated in figure 2.4. The equation to calculate the beam waist is shown in equation 2.8, which is a variant on equation 2.4.

$$w_B(h,\lambda) = w_0(\lambda)\sqrt{1 + \left(\frac{d(h) - f_c}{z_0(\lambda)}\right)^2} \quad , \qquad\qquad 2.8$$

where w_B is the e^{-2} intensity diameter of interest, w_0 and z_0 are as in equation 2.1 and 2.5, f_c is the distance between the cylindrical mirror to the LCD for the center of the beam and $d(h)$ is the distance from the cylindrical mirror to the LCD depending on the spatial beam location in the x-coordinate.

The divergence of the light for the different wavelengths after refocusing can be calculated with equation 2.9 [50].

$$\Phi(h) = \tan^{-1}\left(\frac{h}{BFL \vee FFL}\right) = \tan^{-1}\left(|h|\frac{2d(h) - 2f_c}{2d(h)\cdot f_c - f_c^2}\right), \qquad 2.9$$

where *BFL* and *FFL* are the distances between the mirror and the back and front focal plane.

Figure 2.5 shows, for the two layouts presented in figure 2.3, the e^{-2} intensity beam diameter as a function of the position of the beam in the x plane, with the center of the beam at zero, at the interface of the liquid crystals to the high reflective dielectric coating. The divergence of the beam after reflection and refocusing by the cylindrical mirror is given on the right axis of figure 2.4. The wavelength used in this calculation is 800 nm. For the case of a focal distance of 50 mm the entrance e^{-2} diameter is elongated form 2.5 to 6.25 mm in the y-direction to achieve the same monochromatic spot size in the center.

For the design with a focal distance of 50 mm and a θ of 30º the e^{-2} intensity beam diameter varies from 8 to 43 µm within the e^{-2} intensity profile of the beam in the x-direction. This focal diameter results in a lower spectral resolution, which limits the number of degrees of freedom. For the case of a focal distance of 20 mm and a θ of 70º, the spectral resolution is significant lower. The divergence is for a focal distance of 50 mm and a θ of 30º 0.7 mrad within the e^{-2} intensity diameter of the beam in the x-direction. This non zero divergence after the reflection from the LCD and refocusing changes the Gaussian beam profile to a comet beam profile.

The comparison of the cylindrical achromatic lens and the cylindrical mirror leads to the conclusion that the disadvantages of an achromatic cylindrical lens are small and correctable. These disadvantages are preferable to the distorted spatial beam profile caused by a cylindrical mirror.
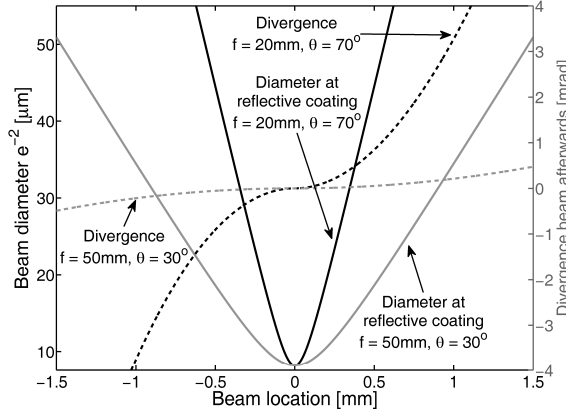
Figure 2.5: Focal size as a function of displacement in the x-direction from the center of the beam. The divergence of the reflected light after refocusing is given on the right.

2.2.4 Choice of dispersive element

The dispersive element should be able to disperse 60 THz of the spectrum over 7.6 mm, in combination with a lens with a focal distance of 20 mm. The central frequency of the spectrum is specified to be 800 nm (375 THz). Hence the spread over the LCD is from 741 nm (405 THz) to 870 nm (345 THz). Design consideration 7 in section 2.2.1 indicates that it is preferable that all components are available commercially. Two common dispersive elements are gratings and prisms.

For gratings, groove densities of 300, 600, 830, and 1200 lines per mm are considered, all of which are commercially available from Edmund Optics. The assumption is made that the grating is placed under an angle ϕ such that the light in the negative first order is diffracted at the same height as the incident beam for the center frequency (375 THz). Furthermore, it is assumed that the LCD is oriented with the pixels in the y-direction. The angle under which the grating is placed implies a correction for the grating period (d). The grating equation with this correction is given in equation 2.10 [50].

$$sin(\beta_m) = \frac{m\lambda}{d\cos\phi} - \sin\phi \, , \qquad\qquad 2.10$$

where m is the diffraction order (-1), d is the period of the grating, and β_m is the angle of the diffracted beam of the mth order. The actual vertical displacement of the different wavelengths for the negative first order projected in the y-direction corrected for ϕ is given in equation 2.11:

25

$$h(\lambda) = f \cdot \tan\left(\sin^{-1}\left(\frac{\lambda}{d\cos\phi} - \sin\phi \right) - \phi \right), \qquad\qquad 2.11$$

The spectral spread is given by the difference in the wavelengths for which equation 2.11 gives a height which equals plus and minus half the height of the active area of the LCD.

For prisms, materials of BK7, SF10, and fused silica are considered. For these prism materials, the angles are calculated under the assumption that the prism has a top angle chosen such that both the incoming and outgoing light beams hit the surface approximately at the Brewster angle for the center wavelength [53]. The wavelengths for which the diffracted light is focused at the edges of the active area of the LCD are calculated for the case that light with a wavelength of 800 nm is sent to the center pixel of the LCD. The constants for the Sellmeier equations to calculate the refractive index are taken from literature [51,55].

The spectral spread across the LCD as well as per pixel is given in table 2.1 for the different dispersive elements and a set of focal distances. The comparison of different focal distances is valid when considering that a (reflective) beam expander can be used to make the monochromatic focal spot size the same for all cases.

Dispersive element	Spectral spread [nm] for different focal distances (Spectral spread per pixel [GHz])				
	f=10 mm	f=15 mm	f=20 mm	f=30 mm	f=50 mm
Grating with 300 lines/mm	0-1912 (>10000)	5-1573 (>10000)	198-1389 (317)	397-1198 (123)	558-1041 (61)
Grating with 600 lines/mm	235-1317 (256)	415-1162 (113)	510-1077 (76)	606-988 (47)	684-914 (27)
Grating with 830 lines/mm	411-1140 (114)	537-1040 (66)	603-984 (47)	669-926 (30)	722-877 (18)
Grating with 1200 lines/mm	591-960 (48)	661-916 (31)	697-890 (23)	732-862 (15)	760-838 (9)
BK7 prism	143-7528 (502)	146-7181 (491)	150-6864 (478)	159-6326 (449)	179-5529 (396)
SF10 prism	243-8400 (293)	247-8068 (287)	251-7743 (282)	261-7191 (270)	284-6328 (246)
Fused silica prism	119-7373 (606)	124-7037 (580)	130-6731 (553)	141-6210 (508)	164-5436 (433)

Table 2.1: The resulting spectral spread across the LCD and per pixel presented for a set of selected dispersive optics and a set of focal distances.

From the numbers presented in table 2.1 it is clear that a single prism is unable to spread the spectrum of the laser pulse over the active area of the LCD in the given focal distances. So if a single prism is used as dispersive element, the spectral resolution is low (>1 THz). The case that matches the best with the design considerations is the case with a grating of 1200 lines per mm in combination with a lens with a focal distance of 30 mm. This combination matches the best with the consideration that light from 741 to 870 nm should fall on the LCD, by choosing a center wavelength of 808 nm the spectral spread changes to 740 to 870 nm. It also matches with the required resolution of 0.12 THz (15 GHz · 4096 / 500 = 0.123 THz).

2.2.5   The current setup

The optimal choices for the focusing and dispersive elements as described in sections 2.2.2 and 2.2.3 are not used in practice. Instead, the elements on hand were a cylindrical mirror with a focus distance of 51.7 mm and a grating with 800 lines per mm. In front of the spectral phase shaper a cylindrical beam expander is placed, which expands the vertical entrance size from an e^{-2} diameter of 2.5 mm to an e^{-2} diameter of 10 mm to get a four times smaller monochromatic focal spot size. A schematic of the design of the built spectral phase shaper is shown in figure 2.6.
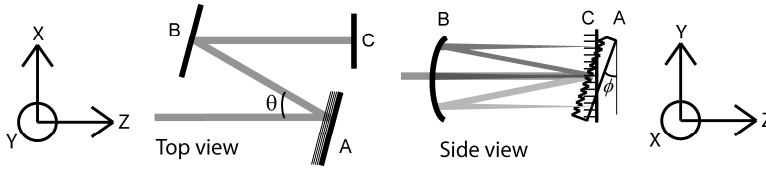

Figure 2.6: Schematic (top and side) view of the spectral phase shaper. (A) grating, (B) cylindrical mirror, (C) spatial light modulator.

The actual monochromatic spot diameter and the mapping of frequency to pixel number of this setup are of interest. Figure 2.7 shows the monochromatic focal size (e^{-2} intensity diameter) for different angles of incidence on the curved mirror and for different wavelengths. The lines in figure 2.7 are calculated with equations 2.1 and 2.7. The horizontal axis displays the wavelength and the vertical axis gives the e^{-2} intensity diameter. The focal spot sizes are given for four different deflection angles (θ), the angles are 0, 20, 30, and 40º. The definition of θ is indicated in figure 2.6.

The angle of incidence on the curved mirror in the design is 15º ($\theta = 30º$). For light with a wavelength of 800 nm, the monochromatic e^{-2} radius is calculated to be 2.5 μm, which means that the monochromatic focal diameter is less than 3 pixels (e^{-2}).
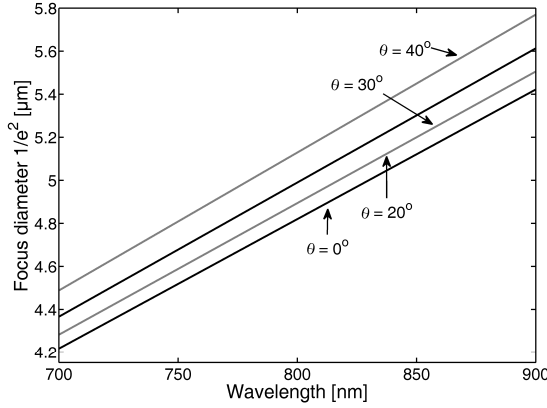
Figure 2.7: e^{-2} intensity diameter of the monochromatic spot size for different deflection angles (θ) on the curved mirror.

The spectral spread across the different pixels of the LCD is shown in equation 2.12. The equation is based on an optical layout where the laser beam reflects off the grating in the horizontal plane. Furthermore, the grating is placed under an angle ϕ, which is visualized in figure 2.6. This shaper setup gives, in combination with equation 2.9, the following equation which relates the pixel number for different wavelengths and angles:

$$X = \frac{f_{eff}}{1.8\mu m} \tan\left[\sin^{-1}\left(\frac{m\lambda}{d\cos\phi} + \sin\phi \right) + \phi \right] + X_0, \qquad 2.12$$

where X is the pixel number, m is the diffraction order (-1), ϕ is the angle between the vertical plane of the grating (also indicated in figure 2.6), 1.8 μm is the spacing of the pixels of the SLM, d is the period of the grating, and X_0 is the pixel number at the height of incidence (tan[…] = 0). The refraction angles of the grating are directly calculated to a corresponding height in the y-direction at the SLM and the factor 1.8 μm and X_0 are used to translate height to pixel number.

The wavelength for which the negative first order diffraction is refracted in the horizontal plane is the wavelength that is focused on pixel X_0. This wavelength depends on the angle (ϕ) under which the grating is placed. Figure 2.8 shows which wavelength falls on which pixel, for different values of the angle ϕ (18, 19, and 20º); these angles are indicated in figure 2.6. The horizontal axis provides pixel number, and the vertical axis provides the wavelength. This figure shows the effect of the angle ϕ in equations 2.12. A change in X_0 changes the pixel number for all wavelengths with that change; in practice this parameter is based on the vertical position of the LCD. The conclusion can be drawn that, to map frequency or wavelengths to pixel number, three fitting parameters are required: f_{eff}, ϕ, and X_0.
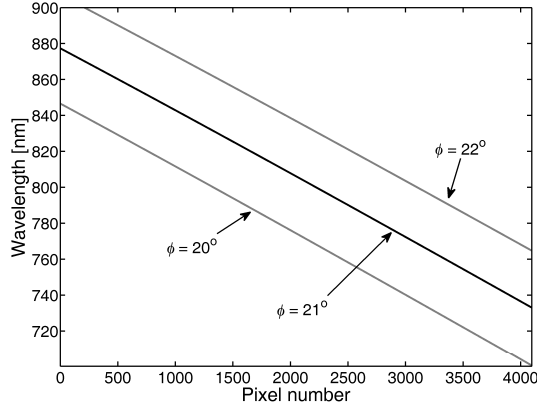
Figure 2.8: The spread of the spectrum across the LCD for different angles of ϕ.

2.3 Liquid crystal device (LCD)

The term 'liquid crystals' is used to indicate substances that exhibit properties between those of a conventional liquid, and those of a solid crystal [58]. For instance, a liquid crystal flows like a liquid, but the molecules in the liquid crystal are arranged or oriented in an ordered manner. There are different types of liquid crystal phases, which can be distinguished based on their optical properties. A liquid crystal phase that can be used for SLMs is the nematic phase, where the molecules have no positional order, but they do have long-range orientation order [59]. The molecular orientation (and hence the materials optical properties) can be controlled by an applied electric field. The optical property which is varied in case of phase shaping SLMs is the effective refractive index. Figure 2.9 shows a schematic view of this effect for an LCD with different voltages across the liquid crystals layer.
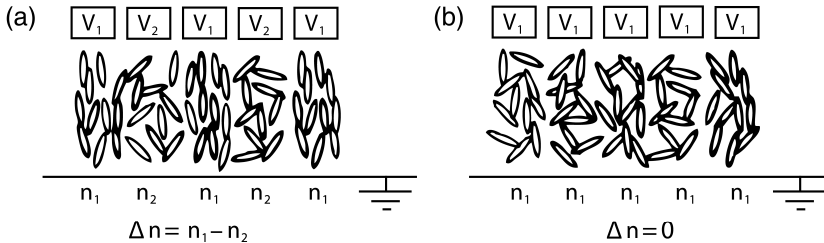

Figure 2.9: Visualization of the basic principle of liquid crystal devices. n_1 and n_2 represent the effective refractive index for the compartments. V_1 and V_2 indicate the voltages over a compartment. A) charged in a pattern, B) uncharged.

The schematic of the selected LCD is shown schematically in figure 2.10. It consists of a linear array of 4096 electrodes, 1 μm by 6 mm each, with a pitch of 1.8 μm. The electrodes are covered with a dielectric reflection coating. The layer of liquid crystals has a thickness of 6.9 μm. A cover glass with a thickness of 2 mm and a transparent electrode on the lower side is placed on top.
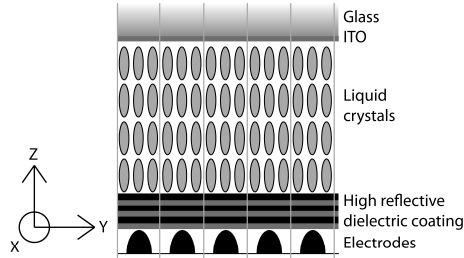

Figure 2.10: Schematic diagram of the LCD. Vertical grey lines indicate pixels.

The electric field from one electrode also influences liquid crystals above other electrodes, due to the spacing between the single front electrode (ITO) and the back electrodes. The spacing between the single front and back electrodes results in electric field crosstalk. Therefore it is impossible to have sharp optical path length differences for adjacent pixels, where a pixel is defined as the spatial domain of one electrode indicated with the gray lines in figure 2.10. The effect of the electric field crosstalk is shown in figure 2.11. The device is specified to have 600 degrees of freedom which means that the smallest features are about seven pixels wide. The absolute location of each feature can be controlled with a precision of one pixel.

The pixels of this LCD can be individually set using an 8 bit grey value. This value is applied to the pixels via an ISA interface card that can be controlled through Labview and C++. The value written to the LCD can be changed at a rate of 2 kHz. Note that this rate is the refresh rate of the voltages applied to the different pixels, which is not equal to the time it takes for the liquid crystals to stabilize to the new voltages. This stabilization time is about 150 to 200 ms, as is shown in section 2.4.4. The reflection coefficient of the high reflective dielectric layer is 85% [60].
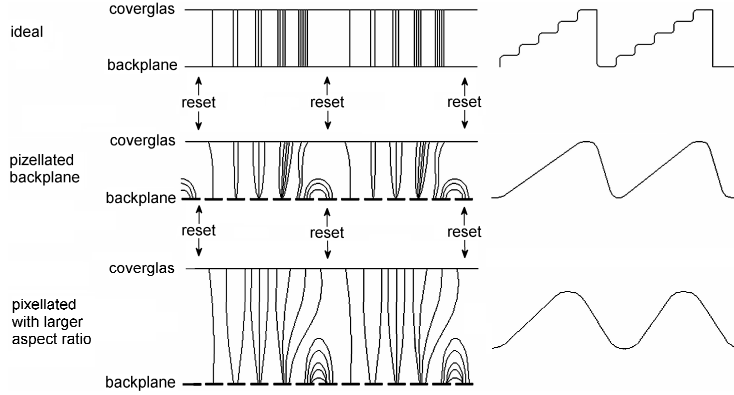
Figure 2.11: Visualization of the effect of the electric field crosstalk [61].

2.4 Calibration of the LCD

The calibration is done with laser light from the Ti:Sapphire oscillator in continuous wave operation. A slit in the laser cavity is used to control the wavelength. The calibration is based on simulating a grating on the LCD. The setup is shown schematically in figure 2.12.
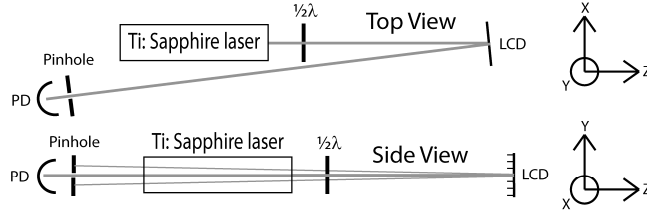

Figure 2.12: Schematic of the calibration layout. LCD is the liquid crystal device and PD is a photodiode. Only the -1, 0, and +1 diffraction orders are shown.

The laser beam from the Ti:Sapphire laser is rotated to vertical polarization using an achromatic half wave plate. The LCD requires vertical polarized light, due to the orientation of the liquid crystals. In the horizontal plane the angle of incidence is measured to be 8 mrad. This angle increases the distance through the LCD by a factor of $3 \cdot 10^{-5}$, which is negligible relative to the depth resolution of 8 bit. The intensity in the zero-order diffraction is measured with a photodiode and the other diffraction orders are blocked by a pinhole. The pattern sent to the LCD consists of a number of pixels with a 'low' value followed by a number of pixels with a 'high' value. This pattern is repeated until the LCD array is filled. For a period of 128 pixels, the

grating constant is 230.4 μm (128·1.8μm). The angles for the different diffracted orders are given by [50]:

$$\theta_m = \sin^{-1}\left(\frac{m\lambda}{d}\right),$$ 2.13

where m is the diffraction order, λ is the wavelength, and d is the grating constant. For a period of 128 pixels, $\theta_{\pm 1}$ is ± 3.5 mrad (or $\pm 0.2°$). The photodiode is placed at 3 m distance from the LCD, where the spacing between the zero and first order is 10 mm, which is twice the e^{-2} diameter of the laser beam at that point, so that overlap between the different orders is negligible. For larger periods the overlap between the orders is increased and for smaller periods the electric field crosstalk is more pronounced.

2.4.1 Electric field crosstalk

Due to the distance between the front electrode and the back electrodes, the electric field applied to one pixel spreads over several pixels of the LCD. The electric field crosstalk behavior depends on the electrode size and shape, the size of the gap between the electrodes, the thickness of the dielectric high reflective coating, and the thickness of the liquid crystals layer. The schematic diagram of the LCD in figure 2.10 indicates the used x, y, and z axes.

Here the effect of the spreading of the field is approximated by a simulation of the voltages in the LCD. The LCD is simulated with a grid size of 200 nm. The ITO layer has a voltage of 0 V and the electrodes have voltages of 0 or 1 V. For each point in the simulated LCD a voltage is calculated by taking the average of the surrounding points. The grid points that simulate the electrodes are kept on the starting values. This calculation is repeated until the voltages change per iteration is such that continuing the iteration process has a negligible effect on the outcome of the simulation. To increase the iteration speed as starting condition a linear voltage dependence is taken over the z-direction, which is the solution for two charged plates [62]. A correction of the grid size for different electrostatic permittivities is put into the thickness of the dielectric coating.

The difference voltage between the ITO layer and the interface between the high reflective dielectric coating and the liquid crystals is the effective voltage over that part of the liquid crystal device. To compensate for the voltage drop over the dielectric coating the calculated voltage drops over the liquid crystals are divided by the voltage drop over the liquid crystal when all pixels are charged with 1 V. This value is used as the normalized effective value in figure 2.13. Figure 2.13 shows the effective pattern on the LCD according to simulations with 10000 iterations for three values of the effective thickness of the dielectric coating (1, 5, and 10 μm) for a square

pattern with a period of 40 pixels. The horizontal axis represents the pixel number and the vertical (sub) axes represent the normalized effective value. The lowest vertical axis shows the programmed values. The other three represent the effective phase profile for the thickness of the dielectric coating.
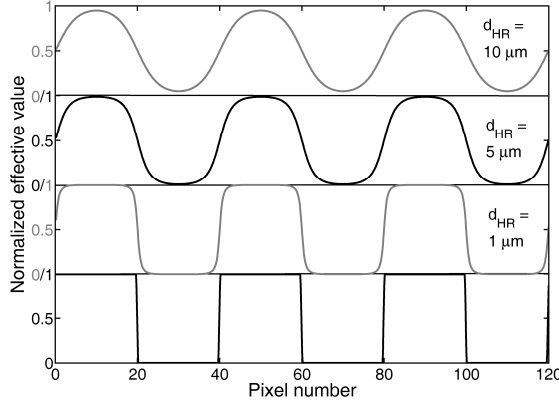

Figure 2.13: Visualization of electric field crosstalk for a pattern with feature size of 20 pixels for different thickness of dielectric coating (d_{HR} = 1, 5, and 10 μm). The lowest graph shows the applied setting.

As can be seen from figure 2.13, for a thicker dielectric coating the average modulation depth of a simulated grating lowers for the same programmed values. The thickness of the dielectric coating can be estimated by modulating the grey value depth of the simulated grating on the LCD and measure the light which is diffracted in the zero-order for the different settings. The expected intensity in the zero-order diffraction for a square pattern is [63]:

$$I_{m=0} = I \cdot \left(\tfrac{1}{2}\cos(\varphi) + \tfrac{1}{2} \right),\qquad\qquad 2.14$$

where φ is the average phase difference between the high regions and low regions. Here the assumption is made that equation 2.14 is also valid for non square patterns. Figure 2.14 shows the measured intensity of the zero-order diffraction as a function of the modulation depth in grey values for 5 different feature sizes (8, 16, 32, 64, 128 pixels), where feature size is here defined as half of the period of the period setting applied to the LCD. The Ti:Sapphire laser is operated in continuous wave at 795 nm. The low value of the grating pattern was kept at a grey value 30 and the high value is varied. The horizontal axis provides the difference between the low and the high value, and the vertical axis shows the measured intensity on the photodiode divided by the photodiode intensity for a pattern with only zeros.
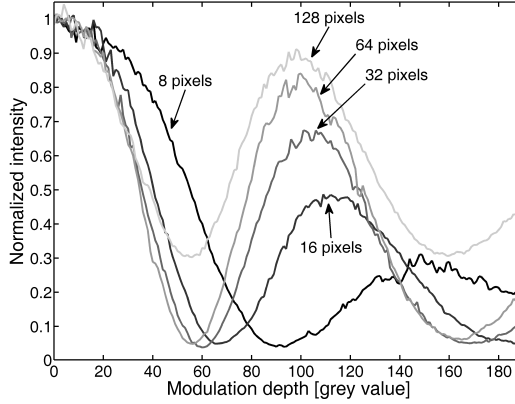
Figure 2.14: Normalized measured intensity of the zero-order diffraction for 5 different feature sizes.

Several effects can be observed in figure 2.14:

A) the minima are non zero. The non zero minima can be ascribed to reflections from interfaces of the protective window and the ITO layer, which are not modulated by the liquid crystals. The non modulated light intensity gives rise to an offset of the measured signal.

B) the large offset in case of a feature size of 128. This offset is caused by the small diffraction angle between the different diffraction orders, so that a part of the plus and minus first order diffraction orders is detected. This effect does not influence significantly the location of the minima and maxima, because the light what is diffracted out of the zero-order is less efficient detected at the photodiode.

C) the difference in height of the maxima for the different feature sizes for an effective modulation depth of 2π. Due to the crosstalk the effective phase pattern is not flat as it should be for truly sharp 2π phase steps. Therefore light is diffracted. This effect gets more pronounced with a higher number of effective 2π phase steps.

D) the position of the minima and maxima for different feature sizes. From this difference the thickness of the dielectric reflective layer is extracted, because the same average resulting modulation depth of the LCD is required to achieve a minimum. The thickness of the reflective dielectric coating has a given value for this LCD, but the relative influence of this thickness can be changed by varying the feature size. Figure 2.15 shows measurements and calculations according the numerical simulation for three different thicknesses of the reflective dielectric coating (d_{HR} = 1, 3, 5, 10, and 15 µm). One parameter is used to calculate the lines in figure 2.15 and that parameter is the average amount of effective phase retardation with an increase of 1 grey value. This value is 0.0625 rad/(grey value) and is subtracted out of the measurements for large

feature sizes. The wavelength for this measurement is 799 nm. The horizontal axis represents the size of the features in pixels, and the vertical axis shows the required modulation in grey value for an effective modulation depth of π. The lower level in grey values of the simulated grating is 30.

For the calculated lines in figure 2.15 the following steps are taken. First an effective phase profile is calculated with the model described in this section. The next step involves a Fourier transformation where the first term is used to give the amount of calculated zero-order diffraction. This calculation is done for a set of modulation depths with increasing difference between the low and high grey values of the simulated grating. From these results the required grey value difference is extracted to achieve a minimum in the zero order diffraction, which is the grey value required for an effective π-phase step.
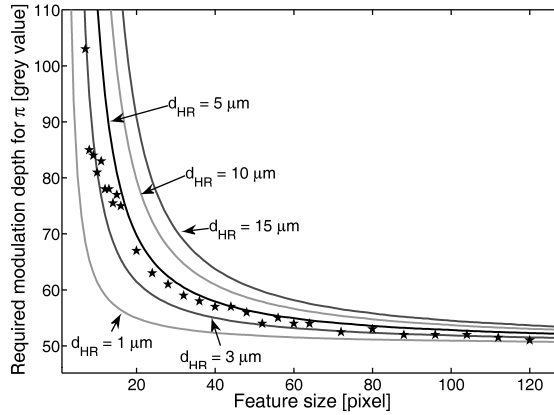

Figure 2.15: Required modulation depth for an effective π phase step, as a function of feature size. Stars represent the measurements and the lines show calculations for different thicknesses of the reflective dielectric coating.

The results presented in figure 2.15 show that the measured values are between or on top of the calculated line for a thickness of 3 µm and 5 µm. The effect of the electric field crosstalk is at largest for small feature sizes; therefore the thickness of the dielectric reflective coating is estimated to be 4 µm. This value is used to compensate the programmed grey values to the LCD to obtain the phase profile of interest. Note that large retardation between adjacent pixels is not possible with this device.

2.4.2   Rotation versus grey value

The electric field crosstalk is estimated in the previous section. In this section the retardation per grey value is calibrated, which is done with simulated gratings on the LCD. To limit the effect of the electric field

crosstalk a feature size of 64 pixels is chosen. As is explained in the start of section 2.4, a negligible part of the other diffraction orders reach the photodiode.

To get an impression of the retardation per grey value as a function of grey value, a grating pattern with a feature size of 64 pixels is sent to the LCD with low values of 0, 50, 100, 150 and 200, and high value increasing from the low value up to 255. Figure 2.16 shows the intensity in the zero-order for the low values, normalized to the zero-order intensity when only zeros are sent to the LCD. Only the trace up to the first minimum is shown for clarity. The horizontal axis represents the high value of the simulated grating and the vertical axis shows the normalized zero-order signal. The wavelength of the laser for this measurement is 843 nm.
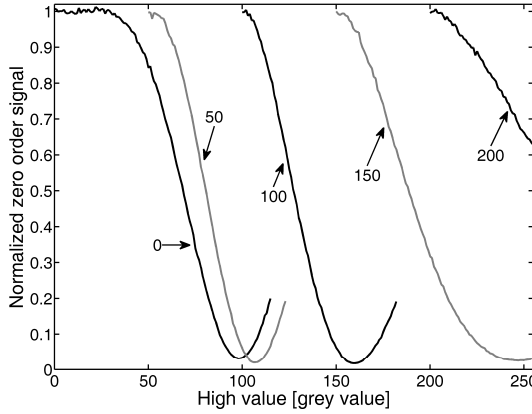

Figure 2.16: Normalized zero-order signal. (Low grey value indicated in the graph, high grey value is shown on the x axis.)

From figure 2.16 it can be concluded that for the first 25 grey values there is hardly any phase retardation. Furthermore, the phase retardation per grey value is not constant over the remaining range of grey values, because the shape of the lines is not constant. Therefore the phase retardation per grey value has to be measured for all of the 256 grey values.

In equation 2.14 the zero-order diffraction efficiency is given for a phase retardation of φ for a square pattern. The inverse of that equation gives φ as function of the intensity. Fitting the inverse of that equation, to the measurements shown in figure 2.16, results in the retardation per grey value change. For this fitting procedure a correction for the non zero value of the zero-order signal in the minima is required. In case of the measurements shown in figure 2.16 this non zero minima is 0.02 from the maximum normalized intensity. The expected grating depth depends as follows on the zero-order diffraction intensity:

$$\varphi_m = \cos^{-1}\left(2 \cdot \frac{I_{meas} - I_{other}}{I_{norm}} - 1\right).$$ 2.15

This procedure is repeated for a set of parameters and finally averaged to minimize the effects of noise that makes the calibration less accurate. Averaging on longer time scales is not possible due to a drift on the order of 20% at low frequencies. The set of parameters are that the low values of the simulated gratings are varied from 1 to 140 in steps of 1, for each of these values the high value is changed until a minimum is found and these traces are then smoothed and matched to equation 2.15. The same is done in the other direction where the high values are varied from 255 to 110 in steps of 1, for each of these values the low value is lowered from the high value to zero or until a minimum is found. The smoothing is based on a second-order Savitzky-Golay filter taking on both sides 5 neighboring values into account; this filter leaves the underlying linear and quadratic slope intact [64]. Figure 2.17 shows the phase retardation per grey value after averaging the results of the 286 individual traces. The horizontal axis provides the grey value and the vertical axis on the left provides the retardation per grey value. The integrated phase retardation is shown on the right axis. The wavelength is 843 nm and a correction factor of 1.03 is applied to correct for the electric field crosstalk as is described in section 2.4.1.

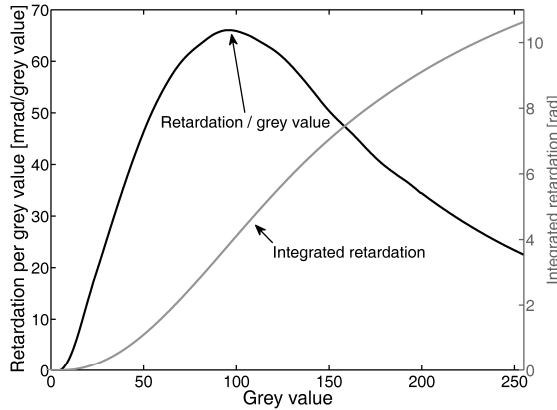*Figure 2.17: Retardation per grey value in mrad per grey value as a function of grey value. The integrated retardation is given on the right axis.*

The total retardation of this LCD for 843 nm is 3.4π rad. In the region around grey values of 100 the smallest possible controllable retardation is about 65 mrad (for 843 nm). Furthermore it can be seen that grey values below 20 have a negligible effect on the total retardation.

2.4.3 Dispersion of the birefringence

In the previous section the phase retardation for different grey values for 843 nm was derived. In this section the dispersion of the birefringence is discussed. The birefringence of a liquid crystal can be approximated as [65]:

$$\Delta n(T, \lambda) = G(T) \frac{\lambda^2 (\lambda^*)^2}{\lambda^2 - (\lambda^*)^2} ,$$ 2.16

where $G(T)$ contains the temperature dependence, λ^* is the mean resonance wavelength, and λ is the wavelength of the applied light. One parameter in the function $G(T)$ is the degree of order of the nematic liquid crystals, which decreases gradually as the temperature rises due to thermal agitation of liquid crystal molecules. This disorder results in a $G(T)$ of zero when the temperature is above the nematic-isotropic phase transition. Here the assumption is made that the variations in temperature are such that $G(T)$ can be approximated as a constant. The retardation of the light reflected from the LCD is what can be measured. This retardation is here described as:

$$\Delta \varphi(\lambda) = \frac{2 \cdot G \cdot d_{LC} \zeta}{\lambda} \frac{\lambda^2 (\lambda^*)^2}{\lambda^2 - (\lambda^*)^2} \propto \frac{\lambda}{\lambda^2 - (\lambda^*)^2} ,$$ 2.17

where G is the resulting value for $G(T)$, ζ is a measure for the alignment of the liquid crystals, d_{LC} is the thickness of the liquid crystal layer. Measuring the constant λ^*, which dominates the shape of the dependence of the birefringence, is here done by determining the required grey value difference, for a square pattern with a feature size of 64, to achieve the first minimum in the zero-order diffraction order as function of wavelength. This measurement is repeated 50 times for each measured wavelength and the grey value difference to acquire the first minimum is averaged. The black squares in figure 2.18 shows the measured retardation versus wavelength divided by the retardation for 800 nm. The error bars indicate the standard deviation of the different measurements for the measurements for that wavelength. The line is a least square fit according to equation 2.17.

The fit parameter for λ^* is 251 nm. The fit matches the measurements with a $1-R^2$ of $2.6 \cdot 10^{-2}$. With this fit, the retardation per grey value, measured for a wavelength of 843 nm, can be extended for the complete spectrum of the Ti:Sapphire oscillator. These results are used to calculate the grey values which have to be sent to the LCD to get required phase function of the spectrum for the experiments.
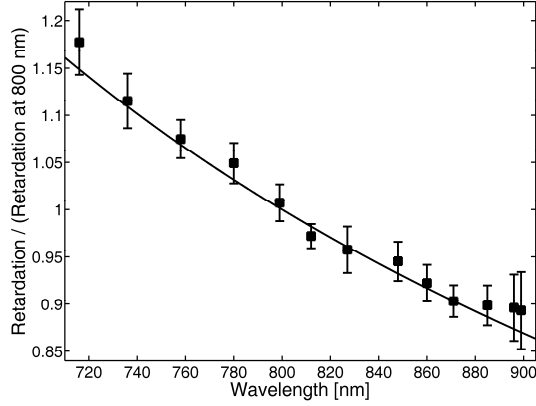
Figure 2.18: Relative birefringence for different wavelengths. The line is a least squares fit from equation 2.17 ($1-R^2 = 2.6 \cdot 10^{-2}$).

2.4.4 Reprogramming time

The controller of the LCD has a maximum refresh rate of 2 kHz. However, the time it takes for the liquid crystals to stabilize is significantly longer as is demonstrated in figure 2.19. The horizontal axis represents the time in ms after the pattern on the LCD is changed from a grating pattern, with a modulation depth of 50 grey values (low value 30) and a feature size of 64 pixels to a pattern of only zeros and changing the grating pattern from a pattern of only zeros to the pattern with a modulation depth of 50 grey values. The vertical axis represents the zero-order diffraction intensity normalized to the value in the case of a pattern with only zeros.

Figure 2.19: Transient behavior of the LCD between two patterns. One pattern consists of only zeros; the other contains a square wave pattern.

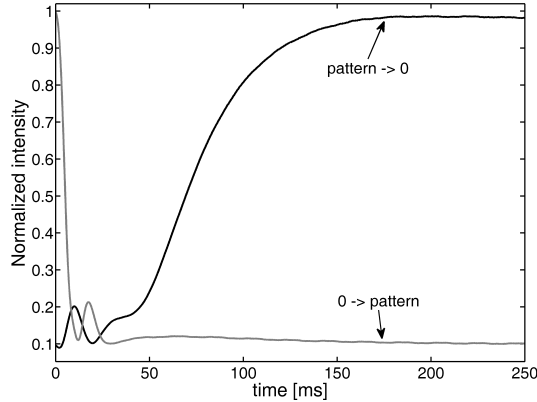From figure 2.19 it can be concluded that a minimum waiting time of 150 to 200 ms is required to make sure that the liquid crystals have adapted to the new voltages.

2.5 Frequency calibration

In this chapter three methods are described to map pixel number on the liquid crystal device to frequency or wavelength. The first method is based on amplitude shaping and requires a spectrograph. The second method is based on creating a local maximum in the Second Harmonic Generation (SHG) spectra and requires a spectrograph and an SHG crystal. The third method is based on the creation of pulse sequences and requires a second-order interferometric autocorrelator, e.g. based on a scanning Michelson interferometer and a Light Emitting Diode (LED) as a two-photon detector. These three methods are compared and conclusions are drawn about their usefulness.

2.5.1 Amplitude shaping

For SLMs that are meant to control the amplitude of the spectrum, it is possible to map frequency to pixel number by setting the transmission of the SLM for selected pixels to zero and measure which parts of the spectrum are affected [66]. Although the spectral shaper discussed in this thesis is a one-dimensional phase-only modulator, amplitude shaping is possible. By applying a phase profile with a spatial extent smaller than the monochromatic spot size, so that light is diffracted beyond the numerical aperture of the system and is thereby not detected. This technique was published by the Squier group [60].

Figure 2.20 shows the effect of a phase step on the spectrum of the laser pulses. The steepness of the step contains spatial frequencies that cause diffraction beyond the numerical aperture of the system. The first 2597 pixels have a grey value of 80 and the remaining pixels have a grey value of 140. The spectrum is recorded on a spectrometer with a resolution of 0.27 nm (Avantes, AvaSpec-3648-DCL-10-OSC). The horizontal axis provides the frequency, and the vertical axis represents the intensity, normalized to the maximum measured intensity in case only zeros are sent to the LCD.

The dip in the spectrum is at a frequency of 367.2 THz (816.4 nm). The spectral location of this dip gives the frequency of the light that falls on this pixel for the alignment during this measurement. By measuring the

frequency of the dip in the spectra for a set of phase steps at different pixel numbers the calibration of the frequency versus pixel number data is measured. Figure 2.21 shows the frequencies of the dips with a fit according to equation 2.12.
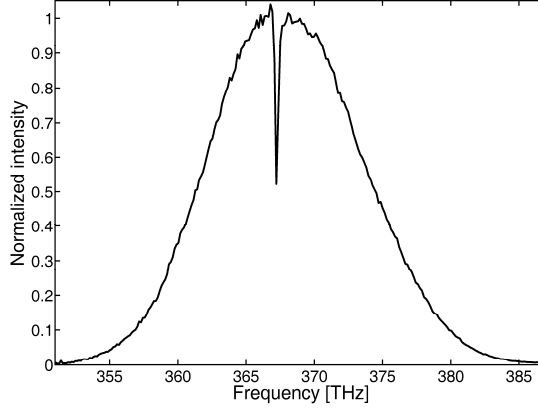
Figure 2.20: Measured normalized fundamental spectrum with a phase step at pixel number 2597.

The measurements fit well with the equation 2.12 as is shown in figure 2.21 $(1-R^2 = 2.2 \cdot 10^{-4})$. The small sudden changes in the measurements points are caused by pixelation of the spectrometer. Due to the sharp feature of the dip there is no interpolation applied to improve the frequency mapping with pixel number. The accuracy of this method depends on the resolution of the spectrometer. In this case the resolution is 0.27 nm, which gives at 800 nm (375 THz) a resolution of 0.13 THz. The average frequency spacing per pixel on the LCD is here 14 GHz. This resolution results in a frequency uncertainty per measurement of 9 pixels (0.13 THz).

Figure 2.21: Measured frequencies (symbols) of the dips caused by a sharp phase jump in the spectrum. The curve is the least squares fit according to equation 2.12.

2.5.2 Peak shaping in the SHG spectrum

An alternative method that relies only on pure phase shaping is based on shaping the spectral phase at the fundamental wavelength in such a way that dist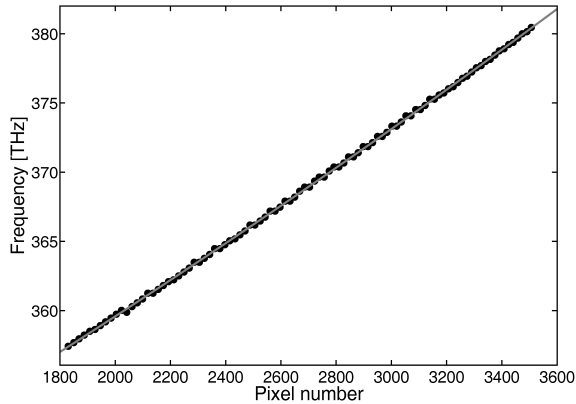inct features are created in the second harmonic spectrum. This method requires an SHG crystal and a spectrometer. A *thin* ($\sim 10\ \mu$m) crystal is required to prevent phase matching criteria from distorting the effect of the applied phase shapes. The amount of second harmonic power generated (P_{SH}) can be approximated using equation 2.18 [67]. This equation applies to a continuous wave illumination, neglects the effects of depletion, and contains a plane wave approximation.

$$P_{SH} = \frac{2cd_{eff}^2 P_F^2 l^2}{n_F^2 n_{SH} \omega_F^2 \varepsilon_0 A}\,\text{sinc}^2\!\left(\frac{\Delta kl}{2}\right) \ \wedge \ \text{sinc}(x) \equiv \frac{\sin(x)}{x}\,, \qquad 2.18$$

where d_{eff} is the effective non linear constant, P_F is the power at the fundamental frequency, l is the length of the crystal, $n_{F,SH}$ are refractive indices for the fundamental and the second harmonic, ω_F is the fundamental angular frequency, A is the (effective) area of the cross-section of the beam and Δk is the phase mismatch ($k(2\omega) - 2k(\omega)$). Although this equation is not for pulsed laser sources, it holds for each spectral component in the spectrum of a pulsed source and as such can be used to evaluate the SHG spectrum. The amount of SHG power depends quadratically on the input power and (for perfect phase matching or $\Delta k = 0$) quadratically on the length of the crystal. Here critical phase matching in BiB$_3$O$_6$ (BIBO) is used. This crystal material has a non-linear constant d_{eff} of 3 to 3.5 pm/V for SHG of 750 to 1100 nm light [68]. The crystal is cut at 28.9º (for SHG at 800 nm in the yz plane type I (e+e → o) phase matching) [69] Figure 2.22 shows the calculated SHG efficiency, for different thicknesses of BiBO crystals. The constants of the Sellmeier equations, from which the refractive indices are calculated, are taken from literature [70]. The horizontal axis shows the frequency, and the vertical axis shows the normalized SHG efficiency, normalized at 375 THz for a crystal thickness of 1 mm.

A BiBO crystal with a thickness of 10 µm is used for mapping the frequencies with the pixel number of the LCD. With this thickness the normalized SHG efficiency remains above 0.85 for spectral region of interest. The SHG spectrum for a shaped input pulse can be approximated using equation 2.19 [71].

$$P_{SHG}(\omega) \propto \left| P_F(\omega)\exp\!\left[i\Phi(\omega)\right] \otimes P_F(\omega)\exp\!\left[i\Phi(\omega)\right]\right|^2 \qquad 2.19$$

where Φ indicates the phase function applied by the spectral phase shaper. This equation neglects phase mismatch (Δk), assumes a flat (completely non-

resonant) conversion efficiency over the full spectrum and the ω^{-2} factor is ignored. For a flat (constant) phase profile the maximum amount of SHG is generated [72].
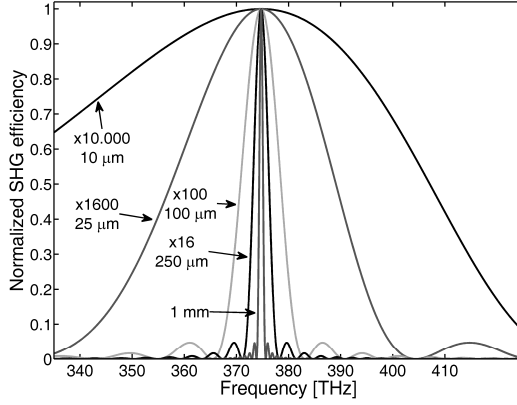
Figure 2.22: The SHG efficiency for a set of different thicknesses of BIBO crystals.

Figure 2.23 shows calculated second harmonic spectra for three different phase profiles of the fundamental spectrum, normalized to the peak value at 400 nm for $\Phi(\omega) = 0$. These calculations are done for a center frequency of 370.5 THz and intensity FWHM of 7 THz, to match with the laser spectrum of the measured spectra presented in this section. The profiles are a flat phase profile, a phase step of π in the center of the spectrum, and a phase step of π at the red side of the spectrum (366 THz). The horizontal axis shows the frequency of the second harmonic, and the vertical axis shows the intensity.

Figure 2.23: Calculated normalized SHG spectra for three phase profiles: a flat phase profile, a π phase step in the center and a π phase step at 366 THz.

The second harmonic spectra in figure 2.23 show a sharp local maximum at twice the frequency of the phase step in the fundamental spectrum. This local maximum in the SHG spectra can be explained qualitatively by

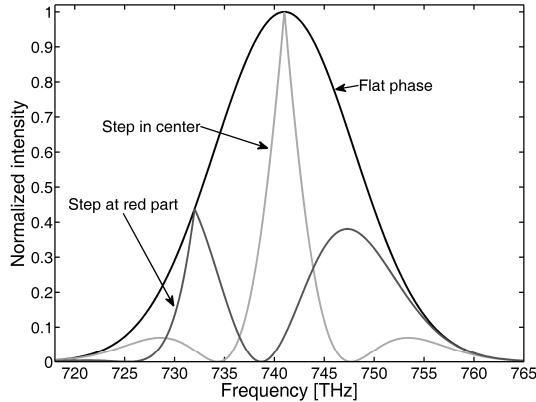considering the interference from different parts of the fundamental spectrum in the creation of the second harmonic spectrum. A specific sum frequency, e.g. 2ν, is given by the combination of all pairs of photons (frequencies) with energies $\nu + \Delta\nu$ and $\nu - \Delta\nu$. With a π phase step (from 0 to π) at frequency ν in the fundamental spectrum, an SHG photon at 2ν is generated by one photon at $(\nu - \Delta\nu)$ with a phase of 0 and one photon at $(\nu + \Delta\nu)$ with a phase of π for all $\Delta\nu$. For all these photon pairs the SHG photon has the same phase $(0 + \pi = \pi)$, which results in constructive addition of all the pairs so that the same value is reached as for a flat input phase. If a frequency is considered that is shifted with respect to 2ν, some pairs contribute with a phase of 0 (from the addition of two 0's or 2 times π) which interferes destructively with the majority of pairs that still contribute with a π phase. This interference around 2ν creates the local maximum at 2ν. The two minima at both sides of the maximum are the frequencies where the same amount of SHG photons are created by pairs of fundamental photons with the same phase (0 or π) as pairs of fundamental photons with different phase. Here the two contributions of the SHG signals interfere destructively. Figure 2.24 shows three measured spectra of the SHG, for the same spectra as displayed in 2.23. The horizontal axis shows the frequency, and the vertical axis shows the SHG spectra. The traces are normalized to the maximum SHG intensity for a flat phase profile.
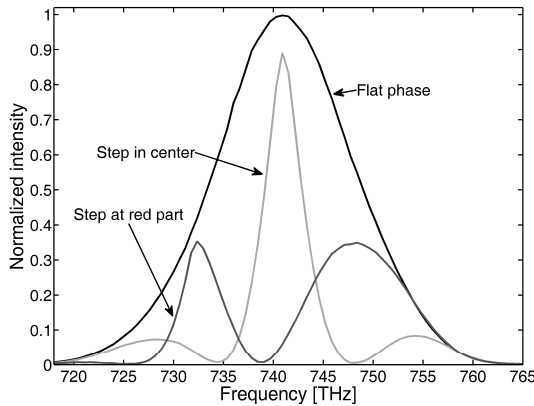
Figure 2.24: Measured normalized SHG spectra for three phase profiles. One flat phase profile and two with a π phase step in the fundamental spectrum.

The peak heights at the double frequency of the location of the phase step do not fully reach the intensity at the position of the flat profile. This lower peak height has two reasons: the first reason is that part of the power at the location of the phase step light is diffracted outside the numerical aperture of the setup (amplitude shaping); the second reason is that due to the electric field crosstalk, the effective phase profile is not a sharp phase step, which

results in some destructive interference from frequencies in the direct vicinity of the phase step.

A series of these measurements can be used to fit the peak position in the SHG spectrum to locations of the phase steps. The local maxima are here less sharp than the local minima in case of amplitude shaping, therefore interpolation of the peak frequency occurs, which removes the sudden changes in measured frequency versus pixel number. Figure 2.25 shows the frequencies of the maxima divided by 2 as a function of the position for the phase step, with a fit according to equation 2.12.

The measurement of the locations of the frequencies is reproduced very well by the model as $(1-R^2 = 8.8 \cdot 10^{-6})$. This result leads to the conclusion that this method can be used for frequency mapping to pixel number. The accuracy of this method depends on the resolution of the spectrometer. In this case the resolution is 0.27 nm, which gives at 750 THz (400 nm) a resolution of 0.26 THz. Because here the SHG signal is measured, the resolution is here equal to that of the amplitude shaping in case no interpolation of the peak frequency is occurred. Due to this interpolation this method gives a better accuracy, which is indicated by the improved value of $1-R^2$. An improvement with a factor of 25 for this value is achieved.
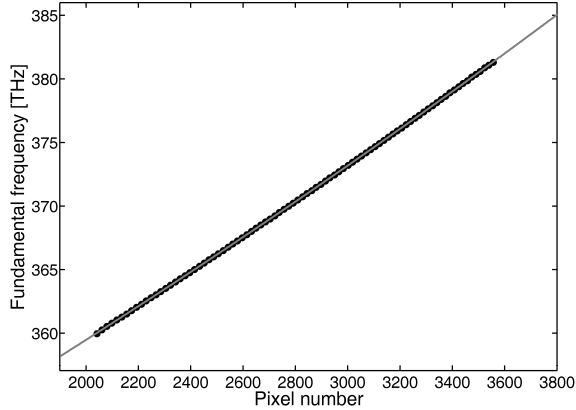
Figure 2.25: Measured frequencies (divided by 2) of the maxima in the SHG spectrum (symbols). The line is the fit to the model.

2.5.3   Frequency calibration with optical autocorrelator

The third method to map frequency to pixel number uses a second-order interferometric autocorrelator. The calibration method is based on the same profiles on the LCD as in section 2.4. Here the periodic phase function splits the original pulse into a pulse train according to the Fourier theorem. The dependence between the different orders is similar, as in section 2.4.

However instead of a spatial spread of the pulse energy, the pulse energy is spread in time. The distance in time between the pulses is inversely proportional to the periodicity in the spectral phase of the applied pattern. The separation in time between the adjusted orders is described by:

$$\Delta t = \frac{2\pi}{\Delta v},$$ 2.20

where Δv is the periodicity in the frequency domain. The intensity profile of the laser pulses is assumed to be Gaussian with a spectral intensity FWHM of 30 THz:

$$E(\omega) = e^{\frac{-(\omega - \omega_c)^2}{2\sigma^2} + i\Phi(\omega)},$$ 2.21

where ω_c is the center frequency of the laser pulse in radians/s, σ is a constant depending on the intensity FWHM (σ is 80 Trad/s for an intensity FWHM of 30 THz), and $\Phi(\omega)$ is the spectral phase function. The corresponding time profile can be calculated using the Fourier transform:

$$E(t) = F^{-1}\{E(\omega)\},$$ 2.22

Figure 2.26 shows the time profile that corresponds to a square phase pattern with a modulation depth of π radians and a spectral periodicity of 0.47 THz. The horizontal axis shows time in ps, and the vertical axis shows the intensity, which is divided by the maximum intensity for a flat phase profile. The two insets show the spectral amplitude and spectral phase.
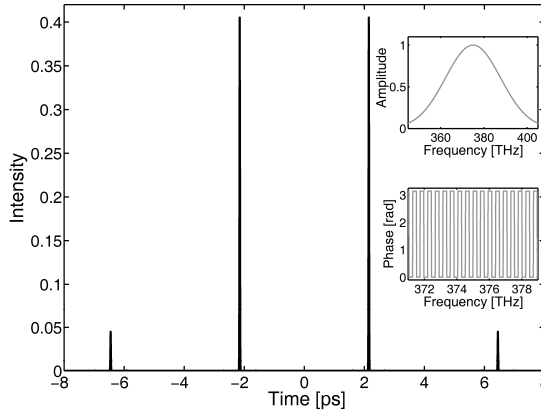
Figure 2.26: Calculated pulse sequence in the time domain, corresponding to a square spectral phase modulation of a Gaussian input spectrum (inset).

The modulation depth of π and square (50% mark/space) pattern eliminate the light at the zero-order (all even orders) diffraction in the time domain. Copies of the original pulse appear at ± 2.13 ps, ± 6.38 ps, ± 10.64 ps, etc. with the same total energy as the original pulse.

The importance of correct calibration of frequency to pixel-number and phase to grey value is demonstrated by the following graph. Figure 2.27 shows the calculated pulse profile in time for a pattern with a fixed feature size of 16 pixels and a constant modulation depth of 60 grey values. The horizontal axis represents the time in ps and the vertical axis shows intensity, (normalized for the maximum intensity for a transform limited pulse, as in figure 2.26). The maximum peak intensity is roughly a factor twelve lower compared to figure 2.27.

The variation in the periods of the phase steps in the frequency domain cause a spread of the diffracted orders (centered at ±N times 2.15 ps). The zero-order intensity is caused by the modulation depth, which is not π radians at all frequencies.
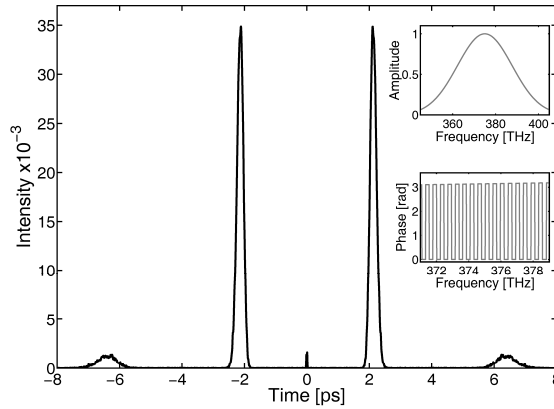
Figure 2.27: Calculated pulse in the time domain for a pattern that is not compensated for birefringence dispersion or the non-linear frequency mapping to pixel number.

To measure these pulses an interferometric second-order autocorrelator is designed and built. This autocorrelator consists of a scanning Michelson interferometer (used to delay one pulse relative to the other), and a two-photon detector. For broadband pulses the autocorrelation measured with a LED can yield a better estimate of the pulse duration than that obtained with a SHG according to the group of D. A. Wiersma [73]. This better pulse length estimation is due to the presence of material dispersion in the SHG crystal; also, spectral filtering of the SHG process due to non fulfilling phase matching criteria occur [74]. Here a GaAsP Light Emitting Diode (LED) is used as the two-photon detector. It has a linear response range from 300 to 680 nm, allowing for a two-photon response in the region of 680 – 1360 nm [73]. The material of the protective cap of the LED is carefully polished off as far as possible to minimize dispersion. The beam is split by a 2 μm thick

(45-55%) pellicle beam splitter, a pellicle is chosen in order to minimize dispersion. The light is focused into the active area of the LED by a spherical gold-coated mirror with a focal distance of 5 cm. A schematic of the setup is shown in figure 2.28.

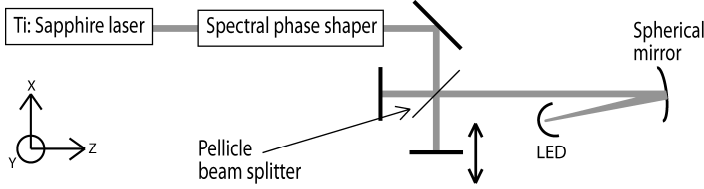*Figure 2.28: Schematic of the autocorrelator layout. An LED is used as a two-photon detector.*

The second harmonic intensity recorded on the LED can be described as [75]:

$$I(\tau) \propto \int_{-\infty}^{\infty}\left|\left(E(t)e^{i(\omega t+\phi)} + E(t-\tau)e^{i[\omega(t-\tau)+\phi(t-\tau)]}\right)^2\right|^2 \partial t \qquad 2.23$$

where τ is the optical path length delay, this τ is the path length difference divided by the speed of light. At zero delay ($\tau = 0$) the signal is equal to:

$$I(\tau = 0) \propto 2^4 \int E^4(t)\partial t , \qquad 2.24$$

At a delay of one-half of the light period, the two fields interfere destructively, cancelling the signal. For large delays, the fields can be added independently, because the pulses do not overlap for large delays, which results in a signal of 0.125 of the magnitude of the signal in the center.

Equation 2.23 assumes that recording of the current generated by the LED is slow relative to the pulse lengths and repetition rate, and that the interferometer setup is stable within a fraction of the wavelength. The first assumption is validated by using a transimpedance amplifier with a bandwidth below 100 kHz. An operational amplifier in combination with a 10 MΩ or a 100 MΩ resistor and a capacitor of 1.3 pF is used (bandwidth of 13 kHz or 1.3 kHz respectively). The second assumption is validated by restricting the lengths of the two arms of the Michelson interferometer to 5 cm and having a cover around the Michelson interferometer. The short arms and cover result in a interferometric stable setup as can be seen in the measured interferometric autocorrelator trace shown in figure 2.30.

From the time traces shown in figures 2.26 and 2.27 are the corresponding interferometric second-order autocorrelator traces calculated with equation 2.23. Figure 2.29 shows the second-order interferometric autocorrelator traces. The horizontal axes show the time difference and the

vertical axes show the intensity divided by the maximum signal at $\tau = 0$ for a flat phase profile.
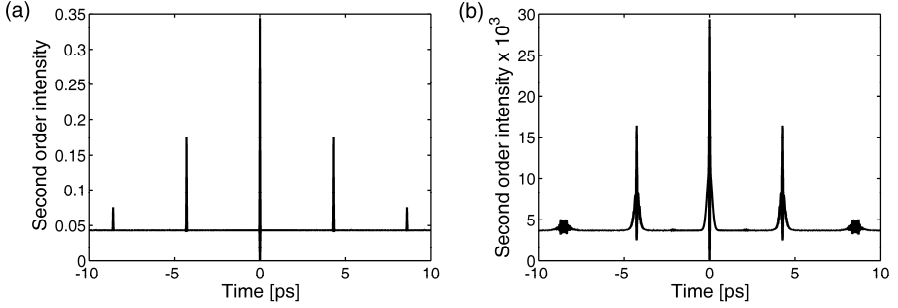
Figure 2.29: Calculated interferometric second-order autocorrelator traces of the time profiles shown in (a) figure 2.26 and (b) figure 2.27.

Figure 2.30 shows a measured interferometric autocorrelator trace for a square phase profile with a period of 0.43 THz. The horizontal axes show the time difference and the vertical axes show the signal from the LED normalized to the baseline. Due to electric field crosstalk, the effective modulation depth is less than π which causes light to remain in the center pulse, causing the feature at ± 2.4 ps.
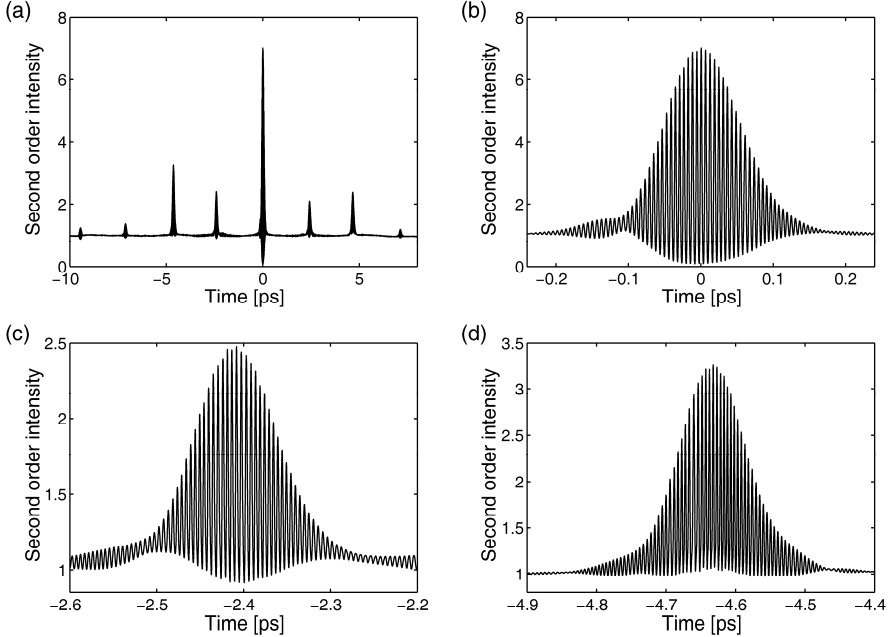
Figure 2.30: Measured interferometric second-order autocorrelator traces. (a) Complete trace; (b) the center, (c) One τ path length difference (d) Two τ path length difference.

49

By minimizing the spread in time separation of the first order, the fit parameters (f_{eff} and ϕ of equation 2.12) can be found experimentally. This minimization is done by scanning in a delay interval where all pulses with an order difference of two are interfering. The main contribution is the first and minus first order contribution, which is used to subtract the fit parameters. These parameters are subtracted by minimizing the FWHM of the interference of the pulses with an order difference of two and by checking if the temporal position of this interference feature is at the intended time difference. This FWHM minimization is done with the downhill simplex method in multidimensions algorithm [76]. This method does not yield the absolute frequency at a pixel, but it yields the frequency spacing between adjacent pixels for pixels covered by the spectrum of the laser pulse.

Autocorrelator traces should be symmetric, which is not the case in the measured trace shown in figure 2.30. This asymmetric is probably because the two paths of the interferometer do not have exactly the same losses and because of some angular misalignment. This misalignment would also explain why the maximum second-order intensity normalized to the base line at zero delay is not 8.

The laser pulse in this measurement has a center frequency of 361 THz with a spectral intensity FWHM of 15 THz. For a flat phase profile, this results in a temporal intensity FWHM of 40 fs. The temporal FWHM is 80 fs here. The difference is caused by dispersion; the phase profiles are not compensated for the higher order dispersion, as the prism compressor only compensates first order dispersion. In the example above f_{eff} and ϕ are 55 mm and 20° respectively. The accuracy of this result is not investigated. If the number of periods over the LCD is higher f_{eff} and ϕ can be estimated more precisely, because any spread in modulation frequency get more pronounced compared to transform limited length of the pulse.

The frequency mapping to the pixel numbers lacks the pixel offset (X_0 in equation 2.12). This pixel offset can be determined using this same setup. If τ is chosen such that there is no interference on the two-photon detector between the two paths, the second-order integrated intensity is given by:

$$I \propto \int_{-\infty}^{\infty} \left| \left(2E(t)e^{i(\omega t + \phi)} \right)^2 \right|^2 \partial t \, , \qquad\qquad 2.25$$

The middle (weighed average) wavelength of the pulse can be determined by sweeping a phase step sweep through the spectrum and recording where the measured second-order intensity is minimal. Figure 2.31 shows the measured signals from the LED for a phase step of π, with an initial guess of 2134 for X_0. The initial guess of X_0 influences the actual phase step, due to dispersion of the birefringence. The horizontal axis shows the pixel number of the

phase step and the vertical axis represents the measured LED signal is normalized to the case of a transform limited pulse. The dashed (grey) smooth curve in figure 2.31 is obtained by taking a Fourier transform of the spectrum (with phase step) and determining the second-order intensity using equation 2.25. The inverse of equation 2.12 is used to get the pixel number from the frequency. A FWHM of 15 THz is assumed, with a center frequency of 361 THz, X_0 of 2150, f_{eff} of 55 mm, and ϕ of 20°. The latter two are derived from the procedure with the second-order interferometric autocorrelator traces. The first two are measured with a spectrograph, so that only X_0 is used as a fit parameter for the calculated line in figure 2.31. The error in the initial guess of X_0 of 16 changes the actual phase step approximately with 2 mrad, which is negligible for the described effect and is much less than the depth resolution of the phase steps.
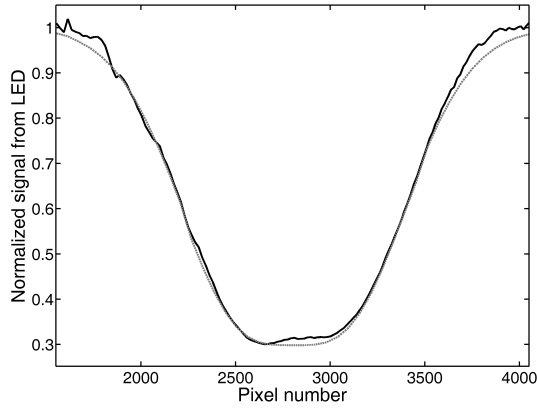
Figure 2.31: Measured signal on the LED for a phase step through the spectrum (black) and the dashed (grey) curve is a calculation.

The center of the dip in figure 2.31 gives the pixel number which corresponds to the center frequency. Together with the fundamental spectrum recorder from a spectrograph, this measurement gives the last parameter for mapping the frequency to the pixel number. The discrepancies between the calculated and measured lines are caused by the remaining dispersion.

The conclusion is that the method with the interferometric second order autocorrelator can be used as a calibration method for the frequency to pixel mapping. However it is a lengthy procedure (more than one hour), because multiple traces are required to minimize the FWHM of the interference of the orders with a difference of two and to control that this interference is at the right path length difference. Therefore it is suggested to use for mapping frequency to pixel one of the first described methods with similar accuracy.

The second-order interferometric autocorrelator described in this section is used to estimate the maximum length of pulse structures the spectral phase shaper can generate. Figure 2.32 shows the time difference between the negative and positive first order pulses. The number of periods over the LCD is varied from 0 to 320 in steps of 16. The horizontal axis shows the number of periods and the vertical axis shows the time difference.

The results shown in figure 2.32 demonstrates that this spectral phase shaper is able to control the phase of the spectrum with more than 600 features and can generate pulse structures in a controllable range of more than 8.5 ps.
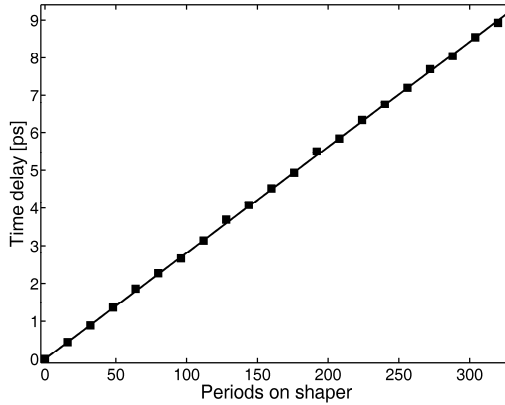
Figure 2.32: Number of periods on the LCD versus the delay time between two pulses originating from one single pulse. (■) experimental data, (—) calculated data.

2.6 AJOLOTE

Frequency Resolved Optical Gating (FROG) is often used to retrieve the spectrum and the spectral phase of a pulse [77]. Here, a new type of FROG apparatus is presented. The name for this design is: Advanced Joint Optimized Long-pulse Observation TEchnique (AJOLOTE). The schematic design is shown in figure 2.33. Note that as in AJOLOTE and FROG the carrier phase and the linear phase are not retrieved [78].

The design of the AJOLOTE is a cross between a GRENOUILLE and an XFROG [79]; the gating pulse is an unshaped pulse from the laser source (reference pulse) and the time delay parameter is scanned in a multi-shot geometry. Therefore the traces have a linear dependence with the input intensity of the spectral phase shaped pulses instead of a quadratic dependence. Furthermore, the ambiguity in the time direction of the laser pulse is removed [79] and the delay range is not limited by the crossing

angle or the spot sizes of the beams, thus a longer delay range appropriate for picoseconds-long spectral phase shaped pulses can be achieved.

Figure 2.33: AJOLOTE setup. (A) half wave plate, (B) pellicle beam splitter, (C) 4 mm BK7, (D) Cylindrical mirror (f=12 mm), (E) Cylindrical mirror (f=24 mm), (F) BIBO crystal, (G) two cylindrical lenses, (H) beam dump, (I) image plane, (J) lens, (K) filters.

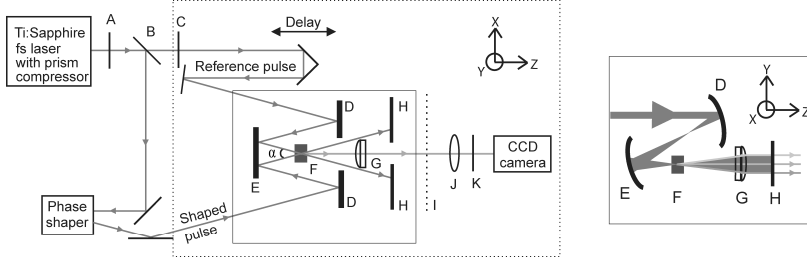The SHG crystal thickness and the choice of its material type influence the spectral range and spectral resolution of the AJOLOTE. Equation 2.26 and 2.28 describe the first two conditions for the correct operation of the GRENOUILLE design [80]. These conditions are also valid in the AJOLOTE design, because in both designs the SHG crystal acts as a frequency filter and the crystal should not distort the pulse before all of the second harmonic light is created. The first condition (equation 2.26) ensures that the fundamental and the second harmonic beams only overlap at the beginning of the crystal for all angles for which the phase matching conditions are not applied:

$$L >> \frac{\tau_p}{GVM} = \left(\frac{\tau_p}{v_g\left(\frac{1}{2}\lambda_0\right)} - \frac{\tau_p}{v_g(\lambda_0)} \right),$$
2.26

where L is the length of the SHG crystal, GVM is the group-velocity mismatch, τ_p is the pulse length of the pulse that the apparatus has to measure (chosen to be 9 ps, which is the longest pulse structure presented in Figure 2.32), $v_g(\lambda)$ is the group velocity at wavelength λ, and λ_0 is the fundamental wavelength. The group velocity v_g is defined by equation 2.27 [53]:

$$v_g(\lambda) = \frac{\partial \omega}{\partial k(\lambda)},$$
2.27

The second condition ensures that the spreading of the pulse by the group-velocity dispersion does not result in distorting the pulse structure:

$$L << \frac{\tau_c}{GVD} = \left(\frac{\tau_c}{v_g\left(\lambda_0 - \frac{1}{2}\delta\lambda_0\right)} - \frac{\tau_c}{v_g\left(\lambda_0 + \frac{1}{2}\delta\lambda_0\right)} \right),$$
2.28

where *GVD* is the group velocity dispersion, τ_c is the pulse coherence time, or a measure of the smallest temporal feature of the pulse, and $\delta\lambda$ is the spectral intensity in the spectral domain expressed in wave lengths. τ_c is given by the considerations described in section 2.2 and equals 20 fs. $\delta\lambda$ equals 64 nm. Equation 2.28 assumes a symmetric spectral intensity in the spectral domain expressed in wavelengths. Therefore the actual wavelengths at the spectral intensity FWHM of the pulse ($\lambda_0-\frac{1}{2}\delta\lambda = 769$ nm, $\lambda_0+\frac{1}{2}\delta\lambda = 833$ nm) are used to determine the thickness.

Table 2.2 shows a comparison of the following crystal types: BaB_2O_4 (BBO), BiB_3O_6 (BIBO), LiB_3O_5 (LBO), and $KTiOPO_4$ (KTP) [81, 82]. The Sellmeier equations used to calculate the *GVM*, *GVD* and the phase matching angles for 345 THz and 405 THz are taken from literature. These frequencies are the minimum and maximum frequency of the frequency range as for the design considerations of the spectral phase shaper. The d_{eff} values are taken directly from literature. The calculations are for crystals cleaved for SHG at 800 nm at normal incidence. The thicknesses are according to equation 2.26 and 2.28 in case the >> or << are replaced for an equal sign.

SHG-crystal type	9 ps GVM [mm]	20 fs GVD [mm]	Phase matching difference angle for 345 and 405 THz [mrad]	d_{eff} [pm/V]
BaB_2O_4 (BBO)	52.9	1.63	16 – 19 [83]	1.9 [87]
BiB_3O_6 (BIBO)	15.9	0.555	49 – 62 [70]	3.2 [68]
LiB_3O_5 (LBO)	73.4	2.05	36 – 44 [84]	0.85 [85]
$KTiOPO_4$ (KTP)	12.1	0.52	15 – 19 [86]	2.7 [87]

Table 2.2: Calculated thicknesses according to equation 2.26 and 2.28, the required focusing strength, and the effective non-linear strength (d_{eff}).

None of the presented crystals can fulfill both of the first two conditions. A 1 mm BIBO crystal cut at 28.9º (phase matching angle for SHG of light with a wavelength of 800 nm) in the yz plane for type I (e+e → o) was chosen to be the best compromise.

The setup of the AJOLOTE shown in figure 2.33 is in the following paragraphs described. The letters in between the brackets are linked to the letters used in figure 2.33. The polarization of the laser pulses is rotated by a half wave plate (A), to suit the LCD and the BIBO crystal (F). The pulses are split on a pellicle beam splitter (B). The reference pulse passes through a piece of BK7 glass with a thickness of 4 mm (C) to compensate for the negative chirp caused by the prism compressor. The negative chirp in the arm with the spectral phase shaper is compensated by two passes through the protective window in front of the LCD. A programmable delay stage, with a

travel range of 50.8 mm, is placed in the path of the reference pulse. This delay stage generates the path length differences between the two pulses. The total delay range is 0.34 ns, which is more than enough for the long (~9 ps) and structured pulses generated by the spectral phase shaper. The shaped pulse is sent, via the phase shaper, to the AJOLOTE. The reference and the shaped pulses are focused in the y-direction by two cylindrical mirrors (D and E), with focal distances of 12 mm and 24 mm. The BIBO crystal is placed in the center of the focus. The aperture of the BIBO crystal is 2.8 mm (x-direction) by 3.0 mm (y-direction). The diameters of the pulses are reduced by a factor of two to a spatial intensity FWHM of 1.2 mm, to reduce diffraction effects from the sides of the BIBO crystal. The adjustment of the spatial beam diameters is done with two reflective beam reducers (two spherical mirrors with a radius of curvature of 200 mm and 100 mm), one for the reference path and one for the spectral phase shaped path, these beam reducers are not shown in figure 2.33. The full angle (α) between the two beams in the x-direction is 35 mrad. The divergence in the y-direction after the two focusing mirrors is 90 mrad (half angle) resulting in a divergence of 50 mrad (half angle) in the BIBO crystal. This angle covers some of the required phase matching angles as presented in table 2.2 (49 – 62 mrad). These parameters result in a 1.7 nm intensity FWHM phase matching bandwidth for 800 nm and an operating range from 751 to 871 nm. This phase matching bandwidth is the spectral resolution. For the outer ranges the intensity FWHM phase matching bandwidth is 1.1 nm (751 nm) and 2.9 nm (871 nm). These phase matching bandwidths are those inside the crystal, the optics which project the AJOLOTE signal onto the camera influence these bandwidths as is discussed in the following paragraph.

Since the phase and the intensity of the original pulses have been encoded into the intensity of the AJOLOTE signal, the phase dispersion after the BIBO crystal does not influence the AJOLOTE trace. The two uncoated cylindrical lenses (G) are glued together with an optical adhesive (NOA60). One cylindrical lens collimates the different phase matched angles (frequency axis) along the y-axis (f =50 mm) of the image plane (I). The second cylindrical lens images the x-axis location where the doubled light is generated (f =100 mm) on the x-axis of the image plane (I). The x-axis contains time delay information for a time span that corresponds to the crossing angle α (here 58 fs). The incoming beams are blocked (H) and the image of the center beam on the image plane is projected with an uncoated 35 mm lens (J) onto the charged coupled device (CCD) camera (monochrome, Pixellink PL-A741, 1280x1024 pixels, pixel pitch 6.7 µm). The image plane is projected by a 35 mm lens onto the camera with a magnification of 0.75 to make that the projections of all the phase matching angles in use fit on the long axis of the camera. The monochromatic focal

spot size at the sensing area of the CCD camera is not taken into account in the earlier calculations for the spectral intensity FWHM of the AJOLOTE apparatus. These calculations are similar to the calculations in section 2.2.3 and not shown here. The monochromatic spot size on the active area of the CCD camera is between 64 and 74 µm. This spot size is so large due to the beam waist of 0.13 mm at the interface of the first lens which is in turn due to the phase matching criteria. The monochromatic spot size and the pixel size influence the spectral intensity FWHM on the camera. Taking the spot size and pixel size into account the spectral intensity FWHM increases at 751 nm by 18% (1.3) nm, at 800 nm by 13% (1.9 nm), and at 871 nm by 20% (3.5 nm).

One line, in the y-direction (1280 pixels), on the camera is selected for the spectral information. The time information is encoded in 20 µm space in the crystal due to the crystal length of 1 mm and an external angle between the two pulses of 35 mrad. Taken the magnification into account this length equals 2.1 pixels on the camera which is smaller than the monochromatic spot size. The temporal resolution is therefore limited to the length of the reference pulse.

The programmable delay line is used to generate the time information of the AJOLOTE trace. Two Schott BG 39 filters (K) are placed in front of the CCD camera to block scattered light from the original pulses.

The AJOLOTE trace is the square of the magnitude of the spectrum of the signal field. The signal field is the nonlinear mixing of the optical fields from the laser directly and the spectral phase shaped field. This trace is given by [88]:

$$I_{AJOLOTE}(\omega,\tau) = \left| \int_{-\infty}^{\infty} P(t) \cdot G(t-\tau) \cdot e^{i\omega t} \partial t \right|^2 , \qquad 2.29$$

where $P(t)$ is the spectral phase shaped field, $G(t\text{-}\tau)$ is the field directly from the laser which passes the programmable delay stage. To demonstrate the performance of the AJOLOTE a binary phase function with a modulation depth of π is applied to generate a pulse structure such as the example in figure 2.27. The applied spectral period in here is 2.04 THz. This phase shape results in two features which are 980 fs apart, and features with less intensity on longer time delays as explained in more detail in section 2.5.3. By scanning the delay stage an AJOLOTE trace is measured. Using an iterative algorithm [89], both the spectral and the temporal intensity and phase are retrieved. Figure 2.34 shows a measurement with the AJOLOTE and the retrieval of the shaped pulse. The AJOLOTE trace in figure 2.34(a) shows the double pulse structure. The reconstructed spectral intensity and the spectral phase are shown in figure 2.34(c). The retrieved AJOLOTE

trace, which is calculated from the spectral intensity and phase for the two pulses, is shown in figure 2.34(b).
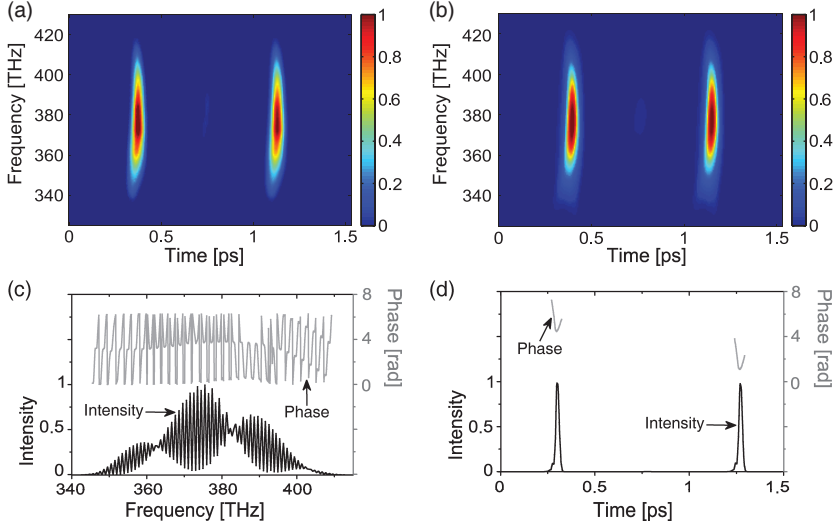

Figure 2.34: (a) Measured AJOLOTE-image, (b) retrieved AJOLOTE-image, (c) reconstructed spectral intensity and spectral phase (d) reconstructed temporal intensity and temporal phase.

The corresponding reconstructed time profile with phase is shown in figure 2.34(d). The residual quantified difference between the two AJOLOTE images equals $8.3 \cdot 10^{-3}$, according to the definition given in equation 2.30 [90]:

$$G = \sqrt{\frac{1}{N^2} \sum_{\omega,\tau}^{N} \left(I_{AJOLOTE}(\omega,\tau) - I_{Retrieved}(\omega,\tau) \right)^2} \ , \qquad 2.30$$

where N is the number of elements of the trace in the frequency axis and time axis. $I_{AJOLOTE}$ and $I_{Retrieved}$ are both normalized to the peak intensities for each. G is the root-mean square error of the difference between the experimentally generated AJOLOTE trace and the retrieved AJOLOTE trace. The applied spectral phase function is not retrieved in the phase function in figure 2.34(c). The retrieval algorithm has put higher order modulation in the amplitude of the spectrum; which is due to the restricted time window, which cuts pulses at larger delays [22]. The retrieved temporal intensity successfully recovers the time delay of 980 fs.

Unfortunately this device is not suited for measuring the complex pulse structures which can be generated by the spectral phase shaper, due to the low spectral resolution, which is significant lower than the spectral resolution of the spectral phase shaper. This design can be improved by using a thin (~10 μm) SHG crystal and a high resolution spectrometer for the

spectral filtering instead of phase matching criteria, which makes it an XFROG device.

2.7 Creating a transform-limited pulse

To have a controllable and known phase profile at the sample the incoming spectral phase must be characterized. Optimization of the SHG at the sample location ensures a transform limited pulse at the sample [91,72]. A phase profile applied to the incoming pulse with that maximizes the second harmonic intensity, has the opposite sign of the original phase profile [92]. The optimization is done by parameterization of the phase in orders of $(\omega-\omega_0)$ [93]:

$$\Phi(\omega) = \sum_{k=2}^{K} c_k \left(\frac{\omega - \omega_0}{\Delta\omega} \right)^k , \qquad\qquad 2.32$$

where $\Phi(\omega)$ is the spectral phase, ω_0 is the center angular frequency of the laser pulse, $\Delta\omega$ is the total angular frequency range of the spectral phase shaper, c_k is the parameter which has to be obtained, and K is the highest order which is taken into account. The summation starts at k equal to 2 since constant or linear phase terms only produce a carrier phase- or time-shift, respectively. The optimization loop is based on a genetic or evolutionary algorithm [94] which uses a set of random values for c_k for the first generation. The next generation consists of a mixture of the values of c_k for the best measured cases, together with random variations (mutations) to find the optimum values of c_k [93].

Here a thin (10 µm) BIBO crystal is used as SHG crystal. The SHG signal is measured with a photodiode after filtering out the fundamental light with a short pass filter and two Schott BG 38 filters. The performance of two evolutionary algorithms is tested to explore robustness and speed for this particular application, with this particular spectral phase shaper. The covariance matrix adaptation (CMA) algorithm and the derandomized adaptation (DR2) algorithm [92] are tested. The parameters for both algorithms are the same: 10 parents, 30 offspring, $K = 15$, and the mutation factor is 0.1. The other parameters are the same as used by Fanciulli et. al. [92]. Figure 2.35 shows the average, worst and best fitness values for one optimization run with the CMA algorithm. The fitness value is here defined as the second harmonic intensity divided by the SH intensity for the case only zeros are sent to the LCD. The horizontal axis shows the generation number the vertical axis shows the fitness value.
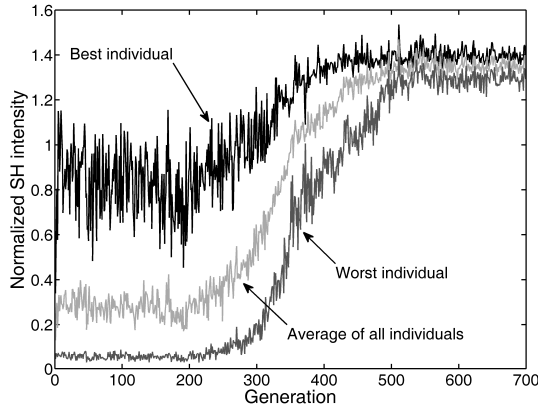
Figure 2.35: Evolution of the worst (dark grey), averaged (light grey), and best (black) SH signal of each generation. A normalized value of 1 corresponds to the SH intensity when only zeros are sent to the LCD.

The CMA algorithm requires 500 generations with each 30 individuals, before it converges in this example. This optimization run requires 15000 measurements which in total take more than one hour if a waiting time of 200 ms is applied to let the liquid crystals adapt to the new voltages and an averaging time of 40 ms is chosen for the signal of the photodiode. The same optimization is done using the DR2 algorithm. Figure 2.36 shows the fittest individual, i.e. the individual with the highest SH intensity of the generation, of each generation of the maximization process for three optimization trials with the same settings. The horizontal axis represents the generation number and the vertical axis represents the fitness value, divided by the second harmonic intensity for the case only zeros are sent to the LCD signal.
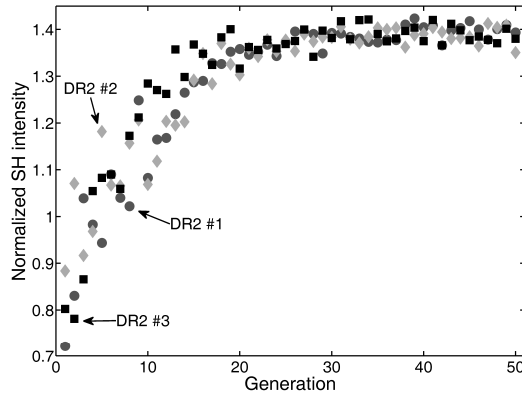

Figure 2.36: Second harmonic signal intensity of the highest individual versus generation number. A normalized value of 1 corresponds to the SH intensity when no additional phase is introduces by the LCD.

The algorithm finds the same optimum value within the noise for the three fitness curves shown in figure 2.36. All these values match with the optimum

value found by the CMA algorithm, which is shown in figure 2.35. The found c_k values are not meaningful to present here, due to the non-orthogonal choice of the basis in the search space. The phase profiles are shown in figure 2.37. The horizontal axis represents the frequency and the vertical axis represents the phase. The phase is zero at the center frequency of 366 THz and the linear overall term is removed in the frequency region between 362 to 370 THz.
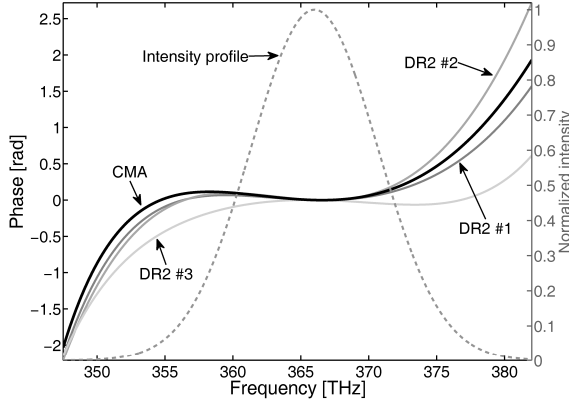

Figure 2.37: Phase profile from the optimization run using the CMA algorithm (thick, black) and three profiles from the DR2 algorithm. The dashed line indicates the intensity profile of laser pulse from the design constraints.

The phase profiles are not the same for all four cases. The CMA algorithm results in similar phase profiles as the first two cases of the DR2 algorithm. The third case of the DR2 algorithm results in a clearly different phase profile. Fanciulli et.al. found that the CMA algorithm in their case is more robust but slower [92]. The relative integrated second harmonic signal for the three cases of the DR2 algorithm are calculated with the use of equation 2.19. From the shown phase in figure 2.37 is the shown phase found by the CMA algorithm subtracted to achieve the phase that is used to calculate the relative second harmonic intensities. The spectral intensity FWHM of the laser source is here 11 THz. This bandwidth in combination with the phase profiles result in a calculated integrated second harmonic signal divided by the calculated integrated second harmonic signal for a flat phase profile (CMA case) of 0.996, 0.994, and 0.934 respectively for DR2 case one to three. The large difference with case three of the DR2 algorithm is hard to explain. Probably this large difference is a local maximum and due to some drift the difference is not significant in figure 2.36.

The conclusion is that the DR2 algorithm convergences in approximately 30 generations with the same normalized second harmonic intensity within the noise. In practice the best is to do several runs with the DR2 algorithm, to

take the solution with the highest improvement to minimize the risk of using a local maximum as the phase profile to generate a transform limited pulse.

2.8 Summary and recommendations

Following design considerations, the preferable spectral phase shaper design was presented. This design is based on a grating as dispersive element and a cylindrical achromatic lens to map the frequencies to the different pixels. The used design incorporates a cylindrical mirror. This design results in a distorted beam profile due to astigmatism and coma.

The specifications of the spectral phase shaper that has been built are according to the design considerations given in section 2.2.1. The calibration of the LCD is discussed and three methods are given to map frequency to pixel number. The calibration methods, based on peak shaping in the SHG spectrum or dip shaping in the fundamental spectrum, are presented as the preferable method to use to map frequency with pixel number.

To improve the spatial beam profile the cylindrical mirror in the shaper could be replaced by a cylindrical achromatic lens with a focal distance of 30 mm in combination with 1200 lines per mm grating in the shaper.

To measure the phase shaped pulses that are created, a second-order intensity autocorrelator is built as well as an AJOLOTE, which is a FROG-type of device. The design of the AJOLOTE has a low spectral resolution with a FWHM spread of 1.9 nm in the center of the pulse. This resolution can be improved by taking a crystal with for example a thickness of 10 µm to prevent distortion of the original pulse in the crystal and by taking a spectrograph instead of the phase matching criteria to get a measure of the different frequency components in the AJOLOTE signal. At the start of the project the AJOLOTE was intended as a calibration device for the spectral phase shaper, for which it is not useful due to the low spectral resolution. It can be used to have a qualitatively look at the chirp and the energies in the different pulse structures generated by the spectral phase shaper.

Chapter 3

Two-photon fluorescence

3.1 Introduction

With a spectral phase shaper it is possible to excite fluorescent probe molecules selectively by amplitude shaping of the calculated second harmonic (SH) spectral intensity [26]. Here the spectral phase of the fundamental is shaped such that its resulting SH spectrum overlaps with the absorption band of one fluorescent probe better than that of another fluorescent probe. With this method it is possible to address different fluorescent probes by changing the phase profile applied to the pulse shaper, provided that the absorption spectra are sufficiently different. The two-photon fluorescence signal can be enhanced above the transform limited signal, as was shown by Silberberg and co-workers in the case of intermediate resonances [27]. Here it is shown that the spectral phase of the SH intensity is important for the two-photon fluorescence efficiency. This phase dependence can also be seen in the movie attached to [26]; although it is not mentioned in the text. Furthermore, the results in this chapter indicate that it is possible to enhance two-photon fluorescence by spectral phase shaping to a level exceeding that for a transform limited pulse, without requiring intermediate molecular resonances as in [27]. Although that this chapter shows unexpected intriguing preliminary results the research had been discontinued.

This chapter begins with an explanation of the setup used for the two-photon fluorescence experiments (3.2). A short theoretical description of the SH spectrum and phase for different phase profiles applied to the fundamental spectrum is presented and discussed (3.3). The two-photon fluorescence intensity for different phase steps is shown for various systems: a variant of the green fluorescent protein, the cascade blue dye, and a sample of quantum

dots (3.4). The conclusions and discussions of the results are preliminary and further investigation is required to make it more solid.

3.2 Setup

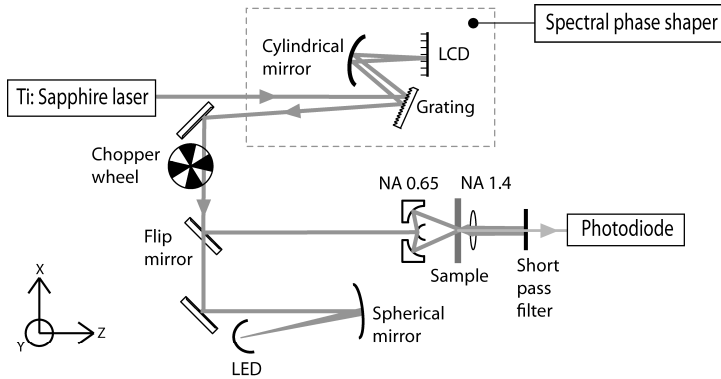The schematic design of the optical setup is shown in figure 3.1.

Figure 3.1: Schematic of the setup for two-photon fluorescence measurements.

A tunable Ti:Sapphire oscillator from KM-Labs was tuned to a center frequency of 348.6 THz (860 nm, 11628 cm^{-1}), with a spectral intensity FWHM of 15 THz (37 nm, 500 cm^{-1}) for the experiments performed on the green fluorescent proteins. The repetition rate of the oscillator was 80 MHz with pulse energy at the experiment of 0.40 nJ. In the case of the cascade blue and quantum dot measurements, the laser was tuned to a center frequency of 377 THz (795 nm, 12575 cm^{-1}), with a spectral intensity FWHM of 18 THz (38 nm, 600 cm^{-1}). The repetition rate of the oscillator was 80 MHz with pulse energy at the experiment of 0.84 nJ. The spectral phase shaper has been described in chapter 2. After the shaper, the laser light was modulated by a chopper at 170 Hz. The modulation frequency is chosen such that DC signals and the 50 Hz modulation of the main voltage and its higher harmonics are rejected. A flip mirror was used to switch between the sample and a GaAsP Light Emitting Diode (LED). The epoxy of the protective cap of the LED was carefully polished down to less than 1 mm to minimize dispersion. The LED supplied feedback information for the procedure to achieve a transform limited pulse at the active region of the LED (see section 2.7). The LED was positioned such that the same number of dielectric mirrors was used as in the path to the sample. Furthermore the path length through air was the same within 2 cm for both paths. Where a window was used in front of the sample, the same thickness of glass was placed in the path towards the LED. The sample path contained a reflective

objective with a numerical aperture of 0.65. A reflective objective was chosen to prevent dispersion and chromatic aberration. The dye or protein sample was located in a sample cell consisting of two glass plates with the solution in between. The quantum dot solution was dried on a single glass plate. The light after the sample was collected by a high NA objective (Zeiss, NA 1.4, oil immersion). After rejection of the Ti:Sapphire light by short pass filters, the fluorescence was detected on a Si-photodiode. The photodiode signal is pre-amplified and further amplified with a lock-in amplifier.

Some questions of this setup remain regarding how well the phase profiles of the pulses are defined. For the experiments on the cascade blue and the quantum dot samples is the difference in phase profiles at the LED and the location of the sample estimated. The procedure for obtaining transform-limited pulses ensures that the phase profile at the active area of the LED is flat. The found phase profile applied to the laser pulse causes a slightly negative chirp at the location of the sample due to the overcompensating for the remaining of the epoxy from the protective cap of the LED. The refractive index of the epoxy layer is given by [95]:

$$n(\lambda) = \sqrt{1 + \frac{1}{0.751 - \frac{0.0116}{\lambda^2}}} \qquad\qquad 3.1$$

where λ is the wavelength in micrometers. The non-linear spectral phase added by the epoxy cover is mainly quadratic. The difference in spectral phase for the center frequency and the frequencies at intensity FWHM is 0.25 rad (0.08π rad) per mm of remaining epoxy. The difference dispersion through air can be neglected, because 1 cm of air adds only 0.5 mrad phase difference between the center frequency and the frequencies at the spectral intensity FWHM.

3.3 Calculations of the SH field and intensity

The calculations in this section demonstrate how a change in the sign of a phase step applied to the laser spectrum has no influence on the spectral intensity of the SH signal, but only influences the spectral phase of the SH signal. The normalized spectrum and a positive phase step of 0.5π in the fundamental spectrum are shown in figure 3.2(a). Figure 3.2(b) shows the normalized SH spectral intensity and spectral phase that belongs to the spectrum and phase of figure 3.2(a). Figures 3.2(c, d) show the same for a negative phase step of 0.5π in the center of the fundamental spectrum. These graphs are calculated with equation 2.19. The horizontal axes represent the frequency and the vertical axes represent the intensity or phase.
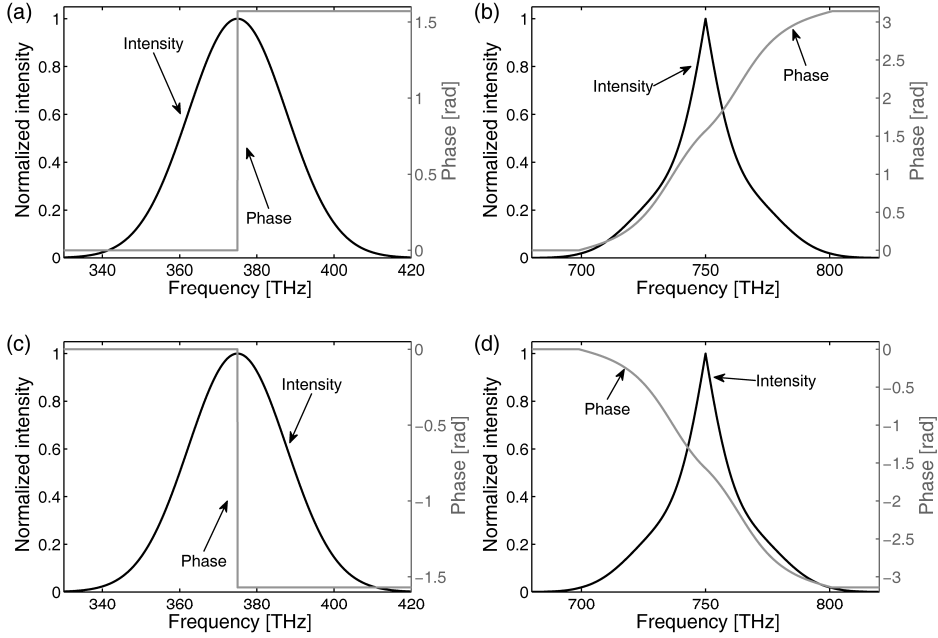
Figure 3.2: (a) Fundamental spectrum with a positive phase step of 0.5π in the center. (b) SHG spectrum and spectral phase. (c) Fundamental spectrum with a negative phase step of 0.5π in the center. (d) SHG spectrum and spectral phase.

From figure 3.2 it can be concluded that a sign change in the phase profile of the fundamental has no effect on the spectral intensity of the SH spectrum but changes the sign of the spectral phase profile for the SH spectrum. The spectral span of the phase transition from 0 to $\pm \pi$ in the SH spectrum depends on the spectral width of the fundamental spectrum. The depth of the phase step in the SH is twice the depth of the phase step in the fundamental. The center position of the phase profile in the SH spectrum is at twice the frequency of the spectral phase step location in the fundamental spectrum.

The normalized spectrum and a positive phase step of π in the fundamental spectrum are shown in figure 3.3(a). Figure 3.3(b) again shows the normalized SH spectral intensity and spectral phase. Figures 3.3(c, d) show the same for a negative phase step of π in the center of the fundamental spectrum. The horizontal axes represent the frequency and the vertical axes represent the intensity or phase.

If the spectral phase of the SH is wrapped, which means that additions or subtractions of 2π are applied until the phase is greater or equal to zero and smaller than 2π, then the spectral phase is equal for figures 3.3(b) and 3.3(d). Therefore no effect due to the sign of the spectral phase is expected in case of a π phase step applied in the fundamental spectrum. Note that this is

strictly true only for infinitely sharp phase steps. The spectral phase shaper used to apply the phase profiles has crosstalk due to the finite size of the monochromatic focal size and the electric field crosstalk (section 2.2 and 2.4). A different sign of the slope of the phase profiles therefore occurs in the regions near the two phase steps in the SH field.
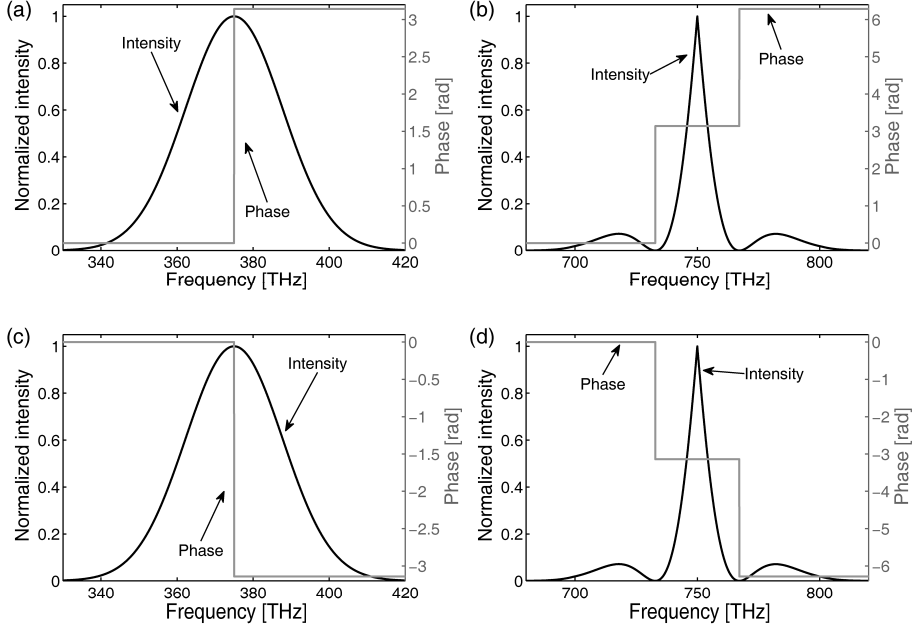

Figure 3.3: (a) Fundamental spectrum with a positive phase step of π in the center. (b) SHG spectrum and spectral phase. (c) Fundamental spectrum with a negative phase step of π in the center. (d) SHG spectrum and spectral phase.

The spectral location of the phase profile in the SH spectrum depends on the spectral location of the phase step in the fundamental spectrum. The spacing between the two phase steps in the SH spectrum depends on the width of the fundamental spectral intensity profile. Figure 3.4 shows the effect of sweeping a phase step through the fundamental spectrum on the integrated SH intensity. This is shown for 0.25π, 0.5π, and π phase steps. The horizontal axis shows the spectral location of the phase step in the fundamental spectrum and the vertical axis shows the integrated SH spectral intensity for phase step sweeps with different amplitudes of the phase steps, normalized to the integrated SH spectrum for a flat phase profile.

In the calculations shown in figure 3.4 no sharp features are present. The smooth shape reflects the non resonant behavior of the SH process; for processes where resonances are influencing the absorption or fluorescence, features are expected. An opposite phase step does not change the result

shown in figure 3.4, because the SH intensity spectrum is here integrated, and the sign of the phase has no influence on the (integrated) intensity spectrum of the SH.
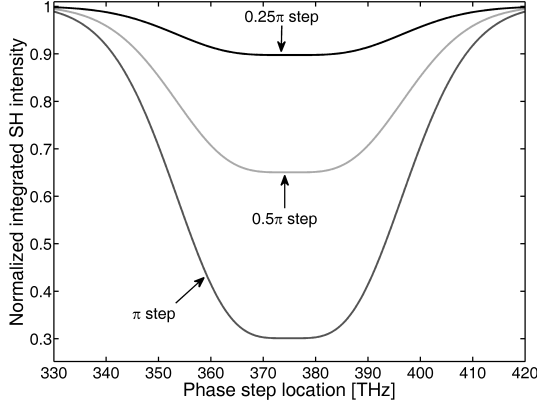

Figure 3.4: Normalized integrated SH intensity for phase step sweeps with a phase step of ¼π, ½π, and π rad.

3.4 Results

Spectral phase shaped two-photon fluorescence experiments are discussed in this section. The first experiment uses a green fluorescent protein whose linear optical properties are described in detail by C. Blum et. al. [96]. The second set of experiments concerns cascade blue dye dissolved in deionized water and dried quantum dots.

3.4.1 Green Fluorescent Protein

A specific green-emitting variant of the Discosoma protein DsRed with a fluorescence maximum at 480 nm was used [96]. The protein was dissolved in water at a concentration of 100 μM. 100 mM of NaCl is added to the water to achieve the required alkalinity for the proteins (pH 7.5). A mode-locked Ti:Sapphire laser was tuned to a center frequency of 348.6 THz (860 nm) to increase the two-photon absorbance, and lower the three photon absorption which shows a local maximum of the linear absorption cross-section at 280 nm. The spectral intensity FWHM of the laser pulse is 15 THz, and the pulse energy is 0.43 nJ at the experiment at a repetition rate of 80 MHz. The estimated focal spot size and concentration imply an average of 300 proteins in the focal volume.

The influences of positive and negative phase steps on the two-photon fluorescence signal are investigated in the experiment. The used phase steps are a positive phase step sweep of 40 grey values and a negative phase step sweep of 40 grey values. This step profile is applied to a base line grey value of 110. No correction is applied for the non linearity of the phase retardation per grey value or the birefringence behavior of the liquid crystals. From the results presented in figure 2.17 and 2.18 it is possible to calculate the used phase steps. Due to the birefringence dispersion the amplitude of the phase step is not constant over the applied spectrum. Therefore the absolute phase steps are given for the frequencies at the intensity FWHM and the center frequency. For the positive phase step of 40 grey values the absolute phase steps are 2.34 (0.745π), 2.28 (0.726π), and 2.23 (0.710π) radian for 341.1, 348.6, and 356.1 THz. For the negative phase step of 40 grey values the absolute phase steps are 2.58 (0.821π), 2.52 (0.802π), and 2.45 (0.780π) radian for 341.1, 348.6, and 356.1 THz. Furthermore the used phase profiles are applied on top of an unknown phase profile at the sample. The used setup is similar to the setup used for the results of the optimization runs (section 2.7), which generate transform limited pulses. The difference is that in this case the spectrum is red shifted which implies less dispersion than the dispersion found by the optimization run, which are shown in figure 2.37. Therefore the spectral unknown phase profile within the spectral intensity FWHM is probably varying less than 0.5 rad in comparison with the spectral phase at the center frequency.

Figure 3.5 shows the two-photon fluorescence for the applied phase profiles. The horizontal axes represent the frequency of the phase step and the vertical axes represent the detected two-photon fluorescence. The shown error bars represents the standard deviation of 50 measurements for a flat phase profile and equals 30 fW.
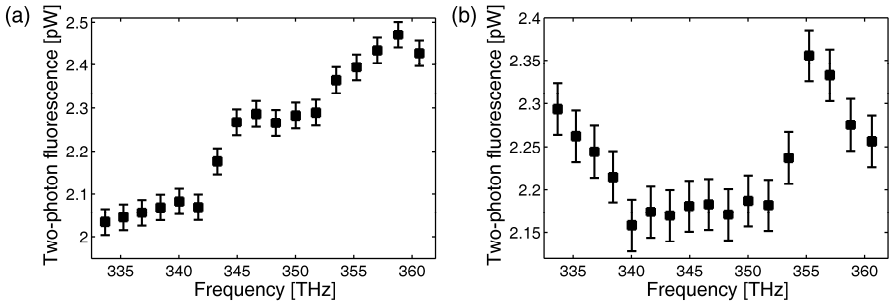

Figure 3.5: a) Two-photon fluorescence intensity for a positive phase step sweep of 40 grey values and b) two-photon fluorescence power for a negative phase step sweep of 40 grey values.

The experimental results show an increase with location of the phase step in the two-photon signal for the positive phase step sweep. For the negative

phase step a dip occurred in the center of the phase step sweep, as in the case of the calculated integrated SH field as shown in figure 3.4. To conclude the experimental results, displayed in figure 3.5, indicate that the sign of the phase is of importance. The difference in phase step size, of the positive and negative phase steps, is less than 10% from which this difference should not be expected. Also the expected phase profile at the experiment for a base line grey value of 110 gives a maximum of 0.5 radians phase difference for the frequencies at FWHM in comparison with the center frequency. However, further investigation is required to draw quantitative conclusions from the influence of the positive and negative phase steps for this system.

3.4.2   Cascade blue

In this section, the complete characterization of the spectral phase shaper is taken into account including the method to generate flat phase profiles at the active region of the LED. The Ti:Sapphire laser was tuned to a center frequency of 377 THz with a spectral intensity FWHM of 18 THz.

Three different amplitudes of the phase steps are presented; the amplitudes are 0.25π, 0.5π and π radians. The molecule is cascade blue dye (Molecular Probes) which was solved in deionized water. Figure 3.6 shows the two-photon fluorescence for positive and negative phase step sweeps for three different amplitudes of the phase step (0.25π, 0.5π, and π). The horizontal axes represent the spectral location of the phase step and the vertical axes represent the two-photon fluorescence signal divided by the two-photon fluorescence signal for a pulse with a flat phase profile.

Figure 3.6: Two-photon fluorescence for the cascade blue dye (a) for three positive phase step sweeps and (b) for three negative phase step sweeps. The amplitude of the phase step sweeps is indicated.

The results, presented in figure 3.6, show two effects. First the two-photon fluorescence signal exceeds the two-photon signal for a flat phase profile for negative phase steps in the region around 365 THz with an amplitude of 0.25π and 0.5π rad. For the positive phase step the two-photon signal is also above the signal for a flat phase profile; but only marginally. The second

effect is that the sign of the phase step has influence on the two-photon fluorescence signal. Figure 3.7 shows the difference two-photon fluorescence signal between the positive and negative phase profiles. Here the difference is defined as the two-photon fluorescence signal from the positive phase step minus the two-photon fluorescence signal from the negative phase step. The horizontal axis represents the frequency of the phase step and the vertical axis represents the difference two-photon fluorescence signal divided by the two-photon fluorescence signal in the case of a flat phase profile.
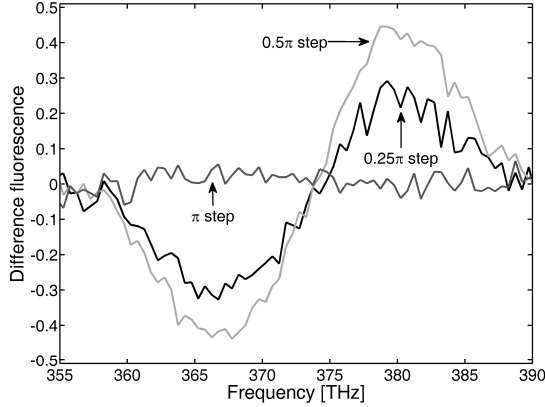
Figure 3.7: The difference two-photon fluorescence signal for the cascade blue dye between a positive phase step sweep and a negative phase step sweep for three phase step amplitudes.

The difference signals for 0.25π and 0.5π phase steps show a clear difference, which shows that the phase of the SH field has an important effect on the two-photon fluorescence signal generated in this sample. As expected, the difference signal in the case of a π phase step shows no clear difference, because the phase of the SH field for a π phase step is the same for both signs.

For comparison the same experiment is performed on the two-photon signal from an LED. Figure 3.8 shows the two-photon signal from the LED for positive and negative phase step sweeps in the spectral domain, with three different amplitudes of the phase step (0.25π, 0.5π, and π); The horizontal axes represent the spectral location of the phase step and the vertical axes represent the two-photon signal divided by the two-photon signal for pulse with a flat phase profile.

As expected for the case of a non-resonant two-photon signal from an LED no clear differences occur for a positive compared to a negative phase step sweep. This strengthens the idea that the two-photon fluorescence yield from transitions of cascade blue is sensitivity to the sign of the phase profile, as

displayed in figure 3.7. Also no enhancement above transform-limited pulses is observed in case of the LED.

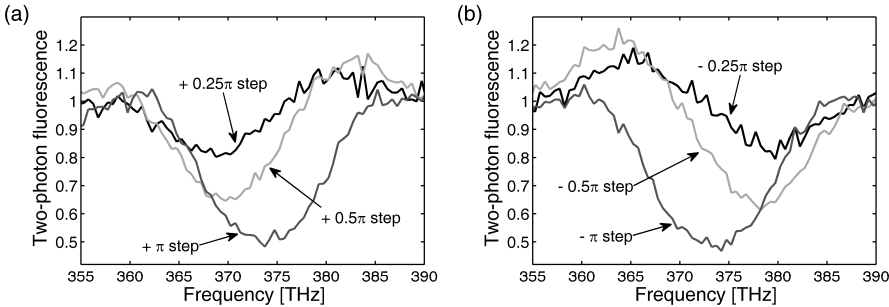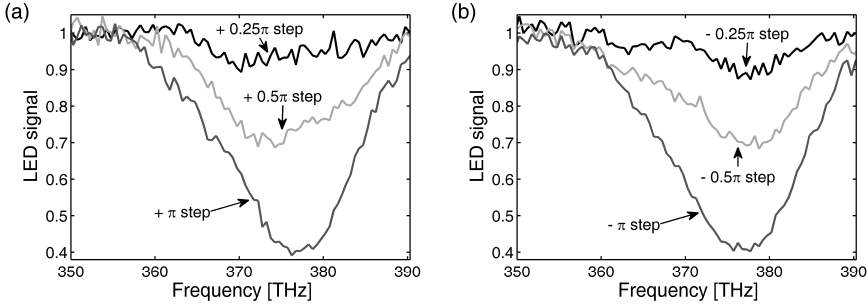*Figure 3.8: Two-photon signal of an LED (a) for three positive phase step sweeps and (b) for three negative phase step sweeps. The amplitude of the phase step sweeps is indicated.*

3.4.3   Quantum dot

This section describes the same experiment as that presented in section 3.4.2, but here dried quantum dot solution (CdSe/ZnS, Evident Technologies, ED-C11-TOL-0540) is used. The number of fluorescent particles in the focal volume is increased by drying the quantum dots on a glass plate. The higher number of fluorescent particles results in a higher signal-to-noise ratio.

Figure 3.9 shows the two-photon fluorescence of the quantum dots for positive and negative phase step sweeps in the spectral domain, with three different amplitudes of the phase step (0.25π, 0.5π, and π); in addition to the required phase profile to get a transform limited pulse. The horizontal axes represent the spectral location of the phase step and the vertical axes represent the two-photon fluorescence signal divided by the two-photon fluorescence signal for a pulse with a flat phase profile.
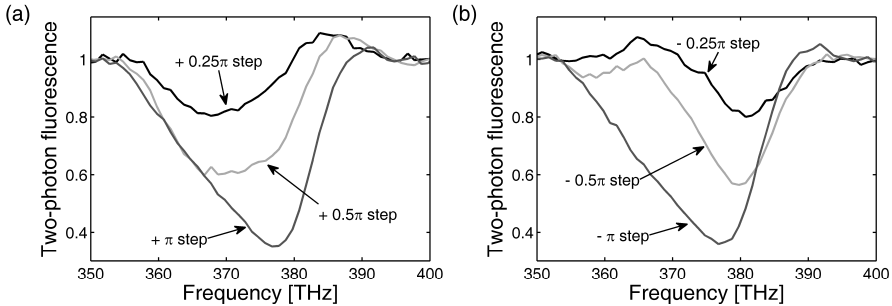

Figure 3.9: Two-photon fluorescence for the quantum dot sample (a) for three positive phase step sweeps and (b) for three negative phase step sweeps. The amplitude of the phase step sweeps is indicated.

The same observations are made from the measurements shown in figure 3.9 that are deducted from the measurements on the cascade blue dye shown in figures 3.6 and 3.7. These observations are that the two-photon fluorescence signal can exceed the two-photon fluorescence signal for a flat phase profile and that the sign of the phase step is of importance. The difference two-photon signal of the positive and negative phase steps are shown in figure 3.10. The horizontal axis represents the frequency of the phase step and the vertical axis represents the difference two-photon fluorescence signal divided by the two-photon fluorescence signal in case of a flat phase profile.
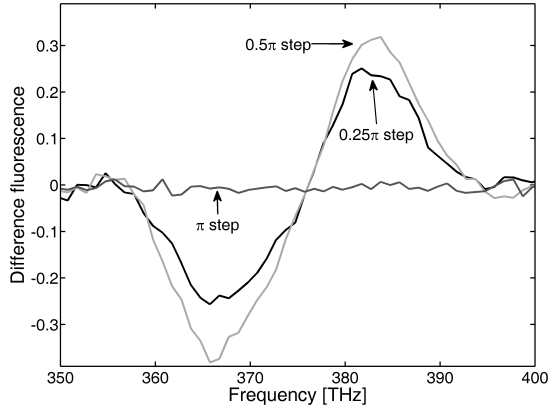
Figure 3.10: The difference two-photon fluorescence signal for the quantum dot sample of a positive phase step sweep and a negative phase step sweep for three phase step amplitudes.

The difference two-photon fluorescence signal of the quantum dot sample behaves similar as the difference signal for the cascade blue dye. However the sign of the phase step is also in this sample of influence for the two-photon fluorescence yield. This difference is this high, that is proposed, that this difference is not caused by the slight negative chirp of less than 0.25 rad phase difference for the phase of the center frequency and the frequencies at the intensity FWHM. Further investigation and theoretical work is required to understand the results shown in this section.

3.5 Summary and recommendations

It is demonstrated in this chapter that the sign of the spectral phase of the calculated SH field is of importance for the two-photon signal in resonant transitions. This is shown for a fluorescent protein, a fluorescent dye (cascade blue), and a type of quantum dots. For the cascade blue and the quantum dots, the shaped phase profiles show a response exceeding the

response for a transform limited pulse, even in cases without intermediate resonances. A non-resonant transition (LED) shows no such an increase, and is insensitive to the sign of the phase step. Some question remains on how well the phase profiles of the pulses were defined. An uncompensated negative chirp was present at the sample location, with a difference in spectral phase for the center frequency and the frequencies at intensity FWHM of less than 0.25 rad (0.08π rad).

Chapter 4

Spectral phase shaping for CARS spectroscopy

4.1 Introduction

Coherent anti-Stokes Raman scattering (CARS) has been successfully used in spectroscopy and microscopy since the development of (tunable) pulsed laser sources [2,28,29]. In CARS, molecular vibrations are excited coherently by pump (ω_p) and Stokes (ω_s) pulses. Subsequently a probe (ω_{pr}) pulse, which is often derived from the same pulse as the pump, generates the anti-Stokes (ω_c) signal ($\omega_c = \omega_p - \omega_s + \omega_{pr}$). A CARS spectrum can be measured by tuning the difference frequency of ($\omega_p - \omega_s$) [3,4,30]. A more direct way to obtain a CARS spectrum is multiplex CARS, with a broadband (~500 cm^{-1}) Stokes pulse. With this method the CARS signal is measured on a spectrometer [31-32]. Single pulse CARS, where ω_p, ω_s, and ω_{pr} are all part of the same broadband pulse, has also been investigated in conjunction with spectral phase and amplitude shaping these methods are discussed in section 4.2.

In this chapter CARS spectroscopy with spectral phase shaping of broadband pump and probe pulses in combination with an independent narrowband Stokes pulse is investigated. With this scheme a demonstration is given of phase shaping strategies to extract the frequencies, bandwidths and relative cross-sections of vibrational lines. This extraction is achieved by spectral phase shaping of both the pump and the probe pulses. A tunable broadband Ti:Sapphire laser for the pump and probe pulses and a ps-Nd:YVO mode-locked laser for the Stokes pulses are synchronized to each other. The high resolution spectral phase shaper, discussed in chapter two, is employed in the experiments described in this chapter. This method allows for spectroscopy

with a precision better than 1 cm^{-1} in the high frequency region around 3000 cm^{-1}. Strong and separated O-H, C-H, and N-H lines are located in this region; these strong lines facilitate the demonstration of the technique.

The resonant features of isolated vibrations can be amplified to such an extent that spectroscopy and microscopy can be performed at high resolution on the integrated spectral response without the need for a spectrograph.

Furthermore a strategy is presented to completely remove the non-resonant background for non-resonant materials in the frequency region covered by the difference between the pump and Stokes spectra.

This chapter starts by giving an overview of different spectral shaped CARS schemes (4.2), followed by the optical setup and the temporal locking of the mode-locked lasers (4.3). Then, simulations of the CARS signal spectrum are presented along with the methods to extract the frequency, the relative cross-section, and the width of a vibrational line (4.4). This section is followed by the measurements on acetone and a comparison to the simulations and the literature (4.5).

4.2 Introduction to broadband CARS

The term broadband is used here for laser pulses with intensity FWHM of more than 15 cm^{-1} (intensity FWHM of less than 1 ps long for a flat spectral phase). Narrowband CARS has the advantage that the selectivity is high, because only one vibration line (of one species) is addressed. In the case of broadband CARS, multiple vibration lines (possibly of multiple species) are located in the bandwidth of the laser pulses, which lowers the selectivity, on the integrated signal. Another disadvantage is the relative amount of non-resonant CARS contribution. If all three beams have the same spectral bandwidth, the non-resonant CARS signal grows quadratically and the resonant CARS signal grows to a maximum value as function of the bandwidth, for constant pulse energy [39]. Figure 4.1 shows the relative contributions of the resonant CARS and non-resonant CARS signals as a function of the pulse bandwidth for the pump and the probe pulses and a narrowband Stokes pulse. The energy in the pump and probe pulses is kept constant. The horizontal axis represents the bandwidth of the laser pulses and the vertical axis represents the relative CARS contribution divided by the CARS contributions in case of pump and probe pulses with intensity FWHM of 10 cm^{-1}. Equations 4.1 to 4.3 (section 4.4) are used in obtaining the result presented in figure 4.1.
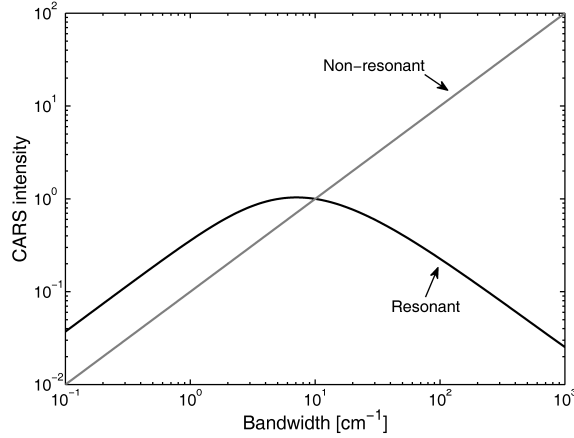
Figure 4.1: Resonant and non-resonant contributions as function of the bandwidths of the pump and probe pulse for a narrowband Stokes.

Figure 4.1 shows that both CARS contributions grow with equal speed for bandwidths which are narrow relative to the intensity FWHM of the resonance. The resonant CARS contribution decays for bandwidths which are equal or broader than the intensity FWHM of vibrational resonance, while the non-resonant CARS contribution continues in a linear way. For two broadband laser pulses the resonant CARS contribution is maximized at the square root of 0.5 times the intensity FWHM of the vibrational resonance. The resonant CARS contribution lowers for large bandwidths, because the spectral overlap of the pump (-Stokes) with the resonance decreases.

Several methods are presented to minimize the non-resonant CARS contribution relative to the resonant CARS contribution. One method is the use of a precisely defined polarization rotation of 71.6º between the pump and the Stokes beams, and measuring the CARS signal with an analyzer orientated at 120º relative to the polarization of the Stokes pulse [97]. The disadvantage of this method is that for complete cancelation of the non-resonant signal, up to 97% of the resonant CARS contribution is also rejected [98]. For broadband CARS, there are several schemes to minimize the non-resonant contribution without the use of specific polarizations. These methods employ control of the spectral properties or temporal of the broadband pulses. With control of the spectral phase not only the non-resonant contribution can be lowered, also the efficiency of the resonant CARS process, and the spectral resolution can be enhanced. Figure 4.2 indicates four different broadband resonant CARS schemes and a non-resonant scheme.
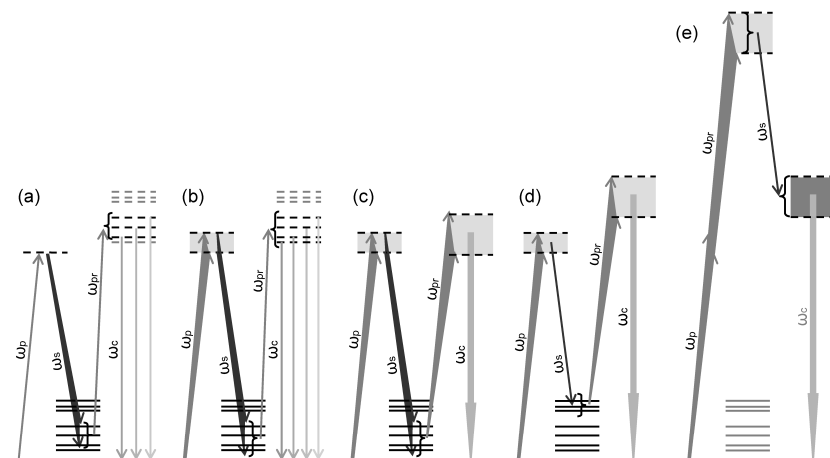
Figure 4.2: CARS energy schemes a) Multiplex CARS, b) Pump and Stokes broad, c) Pump, Stokes, and probe broad, d) Pump and probe broad, and e) Non-resonant energy scheme.

The process depicted in scheme 4.2(a) is called multiplex CARS, which uses a broadband (~500 cm^{-1}) Stokes pulse. The CARS signal is measured on a spectrometer [31-32]. In combination with amplitude shaping this scheme can be used on integrated signals by only allowing a part of the broadband Stokes pulse to contribute to the CARS signal [99].

In the scheme 4.2(b) a broadband pump and Stokes beam are employed with a relative narrowband probe pulse (~100 cm^{-1}). By shaping this probe pulse the non-resonant CARS contribution can be minimized and the resolution can be enhanced [8,100]. This method works by measuring the local maxima in the CARS spectrum. It is not possible to use integrated CARS signals, because the change in the integrated CARS signals is negligible.

Single pulse CARS, where ω_p, ω_s, and ω_{pr} are all part of the same broadband pulse, has also been investigated in conjunction with spectral phase and amplitude shaping. These experiments mainly employ broadband pump and Stokes pulses, in combination with a relatively narrow probe pulse as in figure 4.2(c). Due to the interference between the shaped pump and Stokes pulses it is possible to enhance one transition and suppress other transitions [5,6]. With various phase and/or amplitude profiles of the pump and Stokes pulses vibrational frequencies and bandwidths are retrieved [7-11]. In practice, this technique reaches only vibrational frequencies below 1500 cm^{-1}.

A broadband pump and probe and a narrowband Stokes, as depicted in figure 4.2(d), can be used for high resolution CARS spectroscopy, by applying a chirp. The chirp can be introduced by means of a grating stretcher. The selectivity is based on letting the Stokes overlap with different parts of the chirped pump and probe pulses, by delaying the Stokes pulse or

the pump and probe pulse. This method reaches a reported accuracy of 0.5 cm^{-1} [101].

In this chapter broadband pump and probe pulses are employed in combination with a narrowband Stokes pulse, as depicted in figure 4.2(d). Since the Stokes pulse comes from an independent source, the frequency difference can be set to higher vibrational frequencies (~3000 cm^{-1}). The narrowband Stokes pulse (~1 cm^{-1}) allows for direct projection of the phase profiles onto the molecule. The narrowband Stokes pulse essentially shifts the shaped pump profile to the frequency range where the vibrational resonances of interest are located without changing it. The phase profile that is programmed on the spectral phase shaper directly addresses the molecular profile just as it would in infra-red spectroscopy, without the large focal size associated with infra-red wavelengths [102]. Since the spatial phase modulator covers a range of frequencies in an almost linear way, the resolution at the difference frequency is constant. This approach is different from those approaches where the pump and Stokes beams are shaped. In the latter, vibrational frequencies are targeted by shaping the features with the spectral span of the vibrational resonance in the pump and the Stokes. In this approach a high vibrational frequency requires large spectral features in the phase profile (for example, a sinusoid of only a few periods over the full pump spectrum). This approach therefore has a low spectral resolution in the high vibrational frequency range.

Furthermore, the broad bandwidth of the probe yields a way to interfere signals from different vibrational states in the output spectrum; thereby enhancing the overall signal and suppressing the non-resonant contribution. As such, the presented approach is similar to the multi-probe approach in [103], except that it does not require distributing the energy over the pump and probe to create the multi-probe effect. Furthermore this method works on the full, spectrally-integrated response rather than a selected spectral region. Also the π-phase step introduced in the probe profile to reject non-resonant contributions as in [9,11,103] is not required here; the phase profile of the resonant molecular response itself can here be addressed. A further step in the probe profile is present in this proposed scheme as well (as the same pulse is used for the pump and probe), but this second phase step is not required for spectroscopy.

4.3 Setup

This section begins with an overall view of the optical setup that has been used, followed by the description of the method used to accomplish time overlap of the pulses from the two independent mode-locked laser sources.

4.3.1 Optical setup

A schematic of the optical setup is presented in figure 4.3.
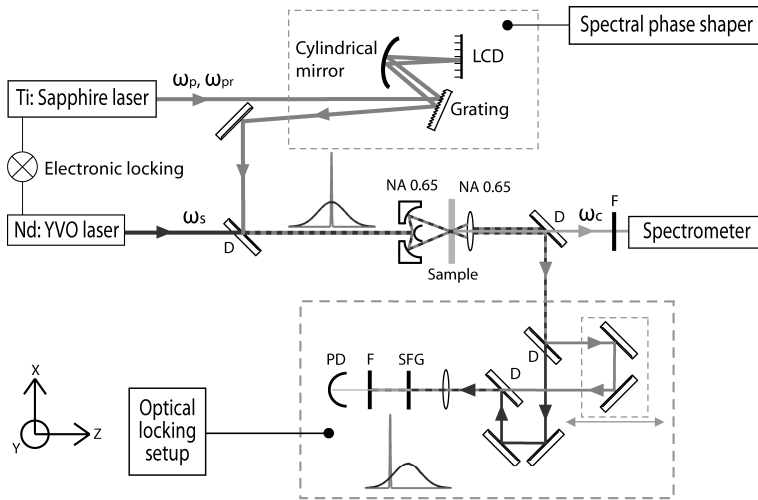

Figure 4.3: Schematic overview of the CARS setup. LCD (liquid crystal device), D (dichroic), F (short pass filter), PD (photodiode), and SFG (sum frequency generating crystal).

A tunable Ti:Sapphire oscillator from KM-Labs with a spectral FWHM of 8.4 THz (18.6 nm, 280 cm^{-1}) centered at 368 THz (815 nm, 12267 cm^{-1}) is used for the pump and probe pulses. The energy per pulse is 0.7 nJ at the location of the sample with a repetition rate of 80 MHz. The liquid crystal device (LCD) of the spectral phase shaper has 4096 pixels with a pixel size of 1 µm by 6 mm with a pitch of 1.8 µm. Usually spectral phase shaping techniques suffer from pixelation effects; in this case these are negligible because of an intentional increase in the crosstalk between pixels, which decreases the effective resolution. For the absolute positioning of the phase profiles the complete number of pixels can be used, which implies a positioning precision of 0.47 cm^{-1} (14 GHz). Further details and description of the calibration of the spectral shaper setup are discussed in chapter 2. The pulses of the Ti:Sapphire laser are pre-compressed by an external prism compressor and shaped to be transform limited (at the position of the sample) by the spectral phase shaper using the method discussed in

section 2.7. The Stokes pulse is generated by a 15 ps (1 cm^{-1}) Nd:YVO laser (281.7 THz (1064.3 nm, 9396 cm^{-1}), Spectra Physics Vanguard). The method and its accuracy for achieving time overlap of the pulses of both independent mode-locked laser sources are described in section 4.3.2. A reflective focusing objective of 0.65 NA has been chosen to prevent additional dispersion and chromatic aberration. The collection objective is a 0.55 NA regular glass objective. The collected light is recorded on a spectrometer with a resolution of 0.27 nm (Avantes, AvaSpec-3648-DCL-10-OSC). The remaining light from the laser sources is used for the optical locking scheme, which is described in section 4.3.2.

4.3.2 Locking of two mode-locked laser sources

The pulses from the Ti:Sapphire laser and the Nd:YVO laser must overlap both spatially and temporally in the sample to generate a CARS signal. Here the synchronization is based on measuring the pulses of both lasers with photodiodes and stabilizing the phase between the signals of the photodiodes by means of piezoelectric transducers [104,105]. The pulses from the Ti:Sapphire laser are measured on a Si-photodiode (circular photosensitive area with a diameter of 1 mm). For the Nd:YVO laser source an InGaAs-photodiode (circular photosensitive area with a diameter of 0.3 mm) is used. An InGaAs-photodiode has been chosen to minimize temperature dependence. The temperature dependence of the sensitivity of a Si-photodiode is large for wavelengths over 1 μm (in the order of 0.8% change in sensitivity per degree Kelvin for operation at 1064 nm) whereas it is negligible for wavelengths under 0.95 μm [106]. For InGaAs-photodiodes the temperature dependence of the sensitivity at 1064 nm is less than 0.05% per degree Kelvin [107]. Figure 4.4 shows the schematic of the locking electronics.
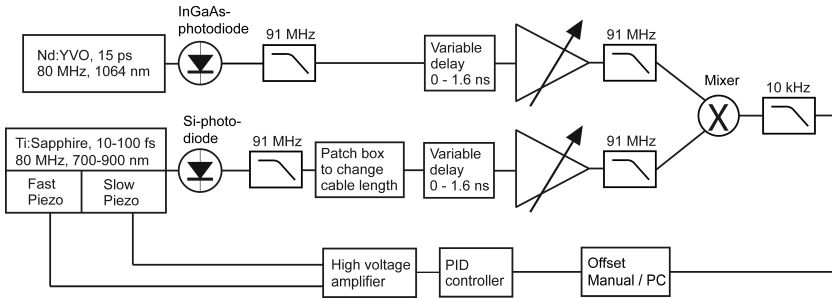

Figure 4.4: Layout of the electronic locking scheme.

The higher harmonics of the photodiode signals are reduced by means of a short pass filter with a cutoff frequency of 91 MHz, because the variable amplifiers are not specified at those frequencies. Optical delay lines on the

table are replaced by a combination of a patch box and a phase shifter. The patch box gives a coarse control of the electronic delay between the signal paths of the measured pulses of both laser by adding or removing cables with different lengths. The phase shifters (variable fine delay) add a controllable phase to the measured signals. The phase shifters have a range of 1.6 ns. The patch box and the phase shifter make it possible to overlap the pulses in the sample for zero output of the mixer. At zero output the signals of the pulses are 0.5π rad out of phase, and amplitude variations do not change the timing between both laser pulses; they only change the loop gain. The photodiode signals are amplified to a peak to peak level of 1.6 V (the specified operating value of the mixer). After the controllable amplification, low pass filters are again used to remove higher harmonics that have been introduced by the amplification electronics. The signals are combined in a mixer, after which higher frequency components are rejected by a low pass filter. To fine tune the overlap a controllable voltage can be added to the signal from the mixer. This voltage, which can also be regulated by a computer, can be used for measuring the cross correlation of both pulses and for time resolved CARS experiments [108]. The filtered mixer signal is sent to a proportional-integral-derivative (PID) controller that stabilizes this signal by generating a feedback signal. This feedback signal is amplified by a high voltage amplifier and then applied to the piezoelectric transducers in the Ti:Sapphire laser. The piezoelectric transducer that controls the position of the end mirror (after the internal prism compressor) in the Ti:Sapphire laser controls the cavity length for changes above 3 Hz and has a total range of 15 μm. The piezoelectric transducer controlling the position of the output coupler controls the cavity length for changes below 3 Hz and has a total range of 30 μm. The output coupler is mounted on a motorized translation stage, used to manually match the cavity length of the Ti:Sapphire laser to the Nd:YVO laser within the range of the piezoelectric transducers. This coarse change of the cavity length is required, as the cavity length changes by changing the bandwidth or center frequency of the Ti:Sapphire laser.

The accuracy of the locking system can not be measured by measuring the electronic feedback signal. This is due to the drift in the transit times of the signals in the electronic cables, which is affected by temperature fluctuations and deformation of the cables. The accuracy of the locking scheme is evaluated by measuring the Sum Frequency Generation (SFG) signal when the Ti:Sapphire pulse is delayed by 7 - 8 ps to coincide with the flank of the Nd:YVO pulse. The setup to delay one pulse in comparison to the other pulse is shown schematically in the lower part of figure 4.3. As long as the residual jitter is such that the overlap of both pulses is present and that the Ti:Sapphire pulse does not drift to the other flank of the Nd:YVO pulse, the

residual drift can be determined by calculating the temporal change out of the change of the SFG signal. The SFG signal is generated in a BIBO crystal cut for SFG of 800 nm and 1064 nm (19.8° in the yz-plane). Figure 4.5(a, b) shows the remaining time jitter between both pulses. The horizontal axes are the time axes and the vertical axes represent the residual jitter in ps. The upper graphs show the measured time jitter measured with a bandwidth of 2.5 kHz. The lower graphs show the time jitter measured with a bandwidth of 100 Hz.
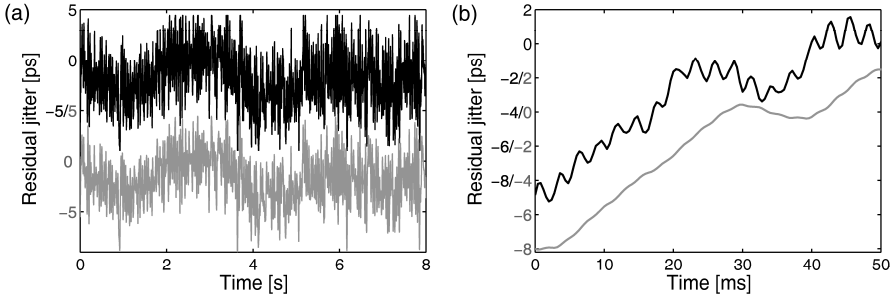

Figure 4.5: Time traces of residual jitter with electronic locking. Black line: Direct measurement. Grey line: Measured time jitter in a 100 Hz bandwidth. a) Overview, b) Zoom.

The residual jitter shown in figure 4.5 is asymmetric for high values of the residual jitter. The residual magnitude of the jitter results in clipping for positive values at the point where the Ti:Sapphire pulse reaches and overshoots the center of the Nd:YVO pulse. On the other side the accuracy is low, due to the low temporal resolution of the SFG signal when the overlap vanishes.

The conclusion is that the residual jitter of several ps results in a CARS signal with a significant noise contribution caused by the residual time jitter. In the literature two solutions are given to enhance the stability of the locking. One method involves the use of fast photodiodes and a mixer with a high bandwidth (>10 GHz) to compare the phase of a higher harmonic of the two repetition frequencies, i.e., at 14 GHz [104, 109]. Another method uses optically generated feedback signal [110]. The optical setup for this method is already implemented and used for the measurement presented in figure 4.5. The optical locking is performed after the objectives in order to prevent the loss of laser power in the sample due to the optical locking scheme.

Before the optical locking is switched on, the laser systems should first be in electronic lock. The amplification of the generated SFG signal is adjustable to stabilize the locking feedback. Figure 4.6(a, b) show the remaining timing jitter between both pulses. The horizontal axes are the time axes and the vertical axes represent the residual jitter in ps. The upper graphs present the

measured time jitter (2.5 kHz bandwidth) and the lower graphs present the time jitter for a bandwidth of 100 Hz.
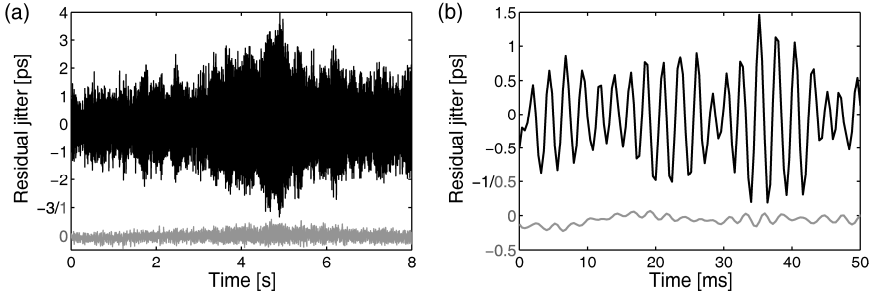
Figure 4.6: Time traces of residual jitter with optical locking. Black line: Direct measurement. Grey line: Measured time jitter in a 100 Hz bandwidth. a) Overview, b) Zoom.

The jitter in case of optical locking is decreased compared to electronic locking and is dominated by an oscillation caused by excessive loop gain. A lower loop gain results in a decrease in oscillation strength but an increase of low frequency contributions. As can be concluded from figure 4.6 the residual jitter has mainly contributions that are faster than 100 Hz. The low frequency drift is reduced significantly compared to electronic locking. Figure 4.7 shows the frequency components of the residual jitter for both locking schemes. The horizontal axis represents the frequency and the vertical axis represents the residual jitter.

Figure 4.7: The frequency components of the residual jitter in case of the electronic locking (grey) and optical locking (black) schemes.

The jitter for optical locking is reduced by more than one order of magnitude in the low frequency range (below 100 Hz) compared to electronic locking.

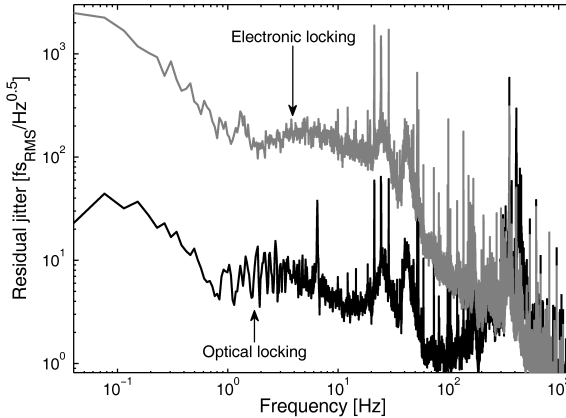The residual integrated jitter in case of electronic locking is 1.9 ps rms for a bandwidth of 0.04 to 100 Hz and the residual integrated jitter of the optical locking system is 60 fs rms for the same bandwidth.

4.4 Simulating the CARS signal

This section starts by describing the theoretical foundations of the work presented in this chapter. Two methods for extracting the frequencies of vibrational resonances are described, based on simple phase profiles. The first method is based on analyzing the CARS spectra for a set of phase profiles and the other on integrated CARS signals. Furthermore, a method is introduced for finding the (effective) line widths and the relative cross-sections of the different vibrational bands.

4.4.1 Theoretical foundations

The total CARS signal has two major contributions as shown in figure 4.2; a resonant and a non-resonant part. The resonant part originates from vibrational resonances and has the following generic form [111]:

$$\chi_R^{(3)}(\omega) = \sum_R \frac{A_R}{\omega_R^2 - \omega^2 + 2i\omega\gamma_R} \, , \qquad 4.1$$

where A_R, ω_R, and γ_R are the amplitude, frequency, and line width of the vibrational resonances. The CARS intensity can be expressed as:

$$I_{CARS}(\omega) \propto \left| P(\omega + \omega_s) \cdot e^{i\Phi(\omega+\omega_s)} \cdot \left(\chi_R^{(3)}(\omega) + \chi_{NR}^{(3)} \right) \otimes Pr(\omega) \cdot e^{i\Phi(\omega_s)} \right|^2 , \quad 4.2$$

where $P(\omega)$ and $Pr(\omega)$ are the intensity profiles of the pump and probe pulses. The spectral phase shaping is indicated by the phase function $\Phi(\omega)$. The Stokes pulse is spectrally narrow and unshaped; therefore only the frequency of the Stokes pulse is taken into account. $\chi_{NR}^{(3)}$ is the non-resonant, third-order susceptibility and is taken to be frequency-independent (flat spectral response). The CARS intensity is the summation of the square of the resonant CARS field, the square of the non-resonant CARS field and an interference term between both contributions:

$$I_{CARS}(\omega) = E_R(\omega)^2 + E_{NR}(\omega)^2 + 2E_R(\omega) \cdot E_{NR}(\omega) , \qquad 4.3$$

where E_R is the resonant CARS field and E_{NR} the non-resonant CARS field. The interference term can be used for homodyne amplification of the resonant CARS signal [31]. The influence of the interference term is discussed in this section.

The amplitude profile for a vibrational resonance is asymmetric due to the ω in the last part of the denominator in equation 4.1. This term makes the $\chi_R^{(3)}$ larger at low frequency than at high frequency. Furthermore, the local maxima of $\chi_R^{(3)}$ lie slightly below the resonance frequencies, which cause slight asymmetries in otherwise symmetric situations.

In this thesis, the profile for a certain width (2γ) of the phase step is defined as the phase profile that corresponds to a vibrational resonance profile with the same intensity FWHM (2γ):

$$\phi(\omega) = \arg\left[\frac{1}{\omega_{Step}^2 - \omega^2 + 2i\omega\gamma} \right],$$
4.4

where ω_{step} is the center frequency of the phase step. This definition for the width allows the width of the step to correspond naturally to the width of a (vibrational) transition.

4.4.2   Analyzing CARS spectra

The case of one vibrational transition with a frequency located in the center of the broadband pump minus Stokes spectrum is analyzed in this section. A positive π-phase step, spectrally located so that it compensates the phase of the vibrational resonance, is applied to the pump (and probe) pulse. The shaped pump and probe pulses are defined to have a FWHM of 7 THz (233 cm^{-1}), centered at 371.68 THz (12398 cm^{-1}, 806.6 nm). The Stokes pulse has a frequency of 281.68 THz (9396 cm^{-1}, 1064.3 nm). The frequency of the vibrational resonance is 90 THz (3002 cm^{-1}) and the intensity FWHM of this vibrational band is 300 GHz (10 cm^{-1}). A calculation of the CARS spectrum is shown in figure 4.8. The normalized spectral intensity and the spectral phase of the pump and probe pulses are shown in figure 4.8(a); the normalized intensity and spectral phase profile of the vibrational resonance are shown in figure 4.8(b). Figures 4.8(c) and 4.8(d) show the resonant and non-resonant CARS spectra respectively. The black lines represent the calculated spectra for the shaped pulse. The grey lines are for comparison and indicate the unshaped (flat phase) CARS spectra. The ratio of $\chi_R^{(3)}$ to $\chi_{NR}^{(3)}$ is chosen as 10 to 1 to reflect an average experimental situation. Note that the intensity of the vibrational band scales quadratically with the value of $\chi_R^{(3)}$.
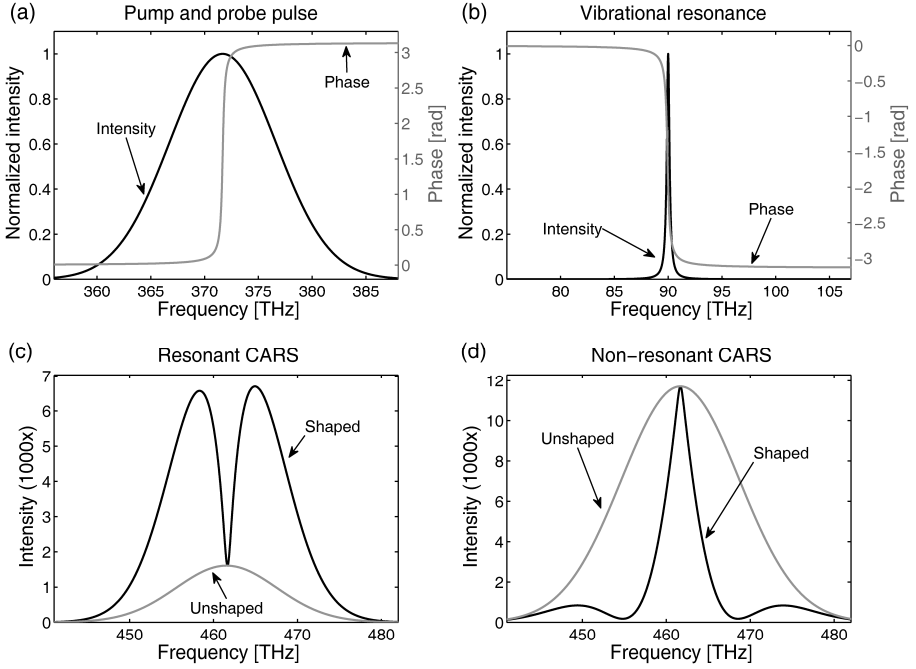
Figure 4.8: a) Spectral intensity and phase profile of the pump and probe pulse. b) Intensity and phase of a vibrational resonance. c) and d) The resonant and non-resonant CARS contribution for the spectral phase in (a) (black) and for a flat spectral phase (grey).

The asymmetry in figure 4.8(c) of the two maxima in the shaped resonant CARS spectra (about 1.5%) is caused by the frequency term in the imaginary part of the resonant third-order susceptibility (equation 4.1). With this phase step in the pump and probe pulses the resonant part is greatly enhanced (overall) compared to the unshaped case, whereas the non-resonant background has decreased.

It can be concluded from equation 4.2 that the non-resonant CARS spectrum is independent of the sign of the phase. This effect allows us to take the difference of a positive and a negative π-phase step, which result in a zero signal for non-resonant materials. The influence of a negative π-phase step for the resonant CARS signal is shown in the following simulation. Figure 4.9 shows the effect of such a negative π-phase step when the resonance and the π-phase step are located in the center of the pump minus Stokes spectrum. The normalized spectral intensity and the spectral phase of the pump and probe pulses are shown in figure 4.9(a); the normalized intensity and spectral phase profile of the vibrational resonance are shown in figure 4.9(b). Figures 4.9(c) and 4.9(d) show the resonant and non-resonant CARS spectra.
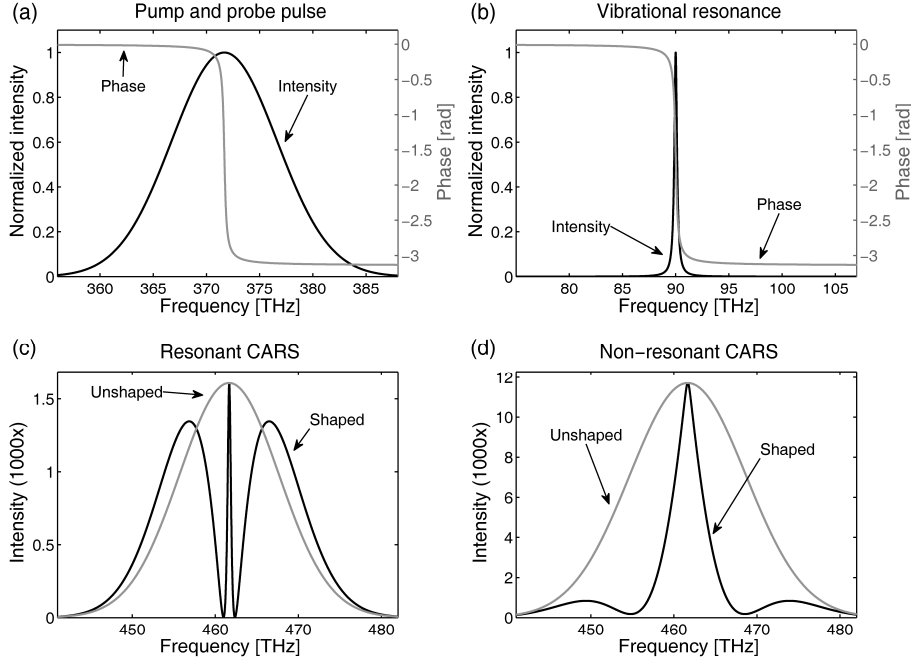
Figure 4.9: a) Spectral intensity and phase profile of the pump and probe pulse. b) Intensity and phase of a vibrational resonance. c) and d) The resonant and non-resonant CARS contribution for the spectral phase in (a) (black) and for a flat spectral phase (grey).

The negative π-phase step creates a sharp feature in the resonant and the non-resonant spectra. These features only coincide in the CARS spectrum when the π-phase step overlaps with the vibrational band. For other positions of the π-phase step, the feature in the resonant signal appears at different positions in the CARS spectrum than the feature of the non-resonant signal. In conclusion, a negative π-phase step sweep produces sharp spectral features that are easily identified in a spectrally resolved measurement. A measured CARS spectrum always contains both a resonant and non-resonant contribution, whose interference influences the strength of the feature in the integrated spectrum.

Therefore, recording the CARS spectra for each π-phase step yields more spectroscopic information than integrated CARS signals. In order to understand the spectrally resolved measurements, I consider first only the resonant contribution; then I consider only the non-resonant contribution. Finally, I discuss the total CARS signal. Figure 4.10 shows contour plots of π-phase step sweeps with (a) a positive π-phase step, (b) a negative π-phase step and (c) the difference, where the horizontal axes represent the location of the π-phase step and the resonant CARS-spectra are displayed along the

vertical axes for only the resonant contribution. Figure 4.10(d) shows the integrated resonant CARS signals for the positive and negative π-phase step sweeps. The horizontal axis represents the location of the π-phase step and the vertical axis represents the integrated resonant CARS signal.
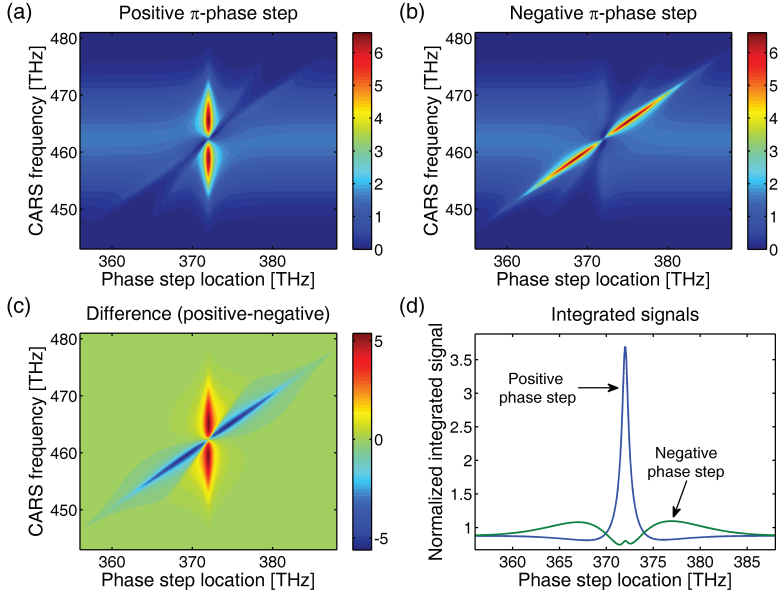

Figure 4.10: Simulation for the resonant CARS signal for one resonance. a) CARS spectra for a positive π-phase step sweep. b) CARS spectra for a negative π-phase step sweep. c) The difference between a negative and a positive π-phase step sweep. d) Integrated signals for the positive and negative π-phase step sweeps.

In the following paragraphs the resonant CARS spectrum for any position of the π-phase step is explained. This explanation is done according to the contributions of equation 4.2. The first part, the convolution of the pump and Stokes pulses, shifts the pump profile to the difference frequency without changing the phase profile. The multiplication with the resonance response can be regarded as a sampling of this shifted pump profile by the resonances of the molecule. Since the resonances have fixed positions they always sample the same part of the pump profile. At this point, the explanation has to be split into two distinctly different scenarios that are responsible for the two distinct features, vertical and with a slope of 1.

The first scenario is for a π-phase step that does not coincide with a resonance so that the result of the sampling of the shaped pump by the molecular response is just a copy of the molecular resonance response where a constant phase (0 or -π) is added to the narrow phase profile of the resonance (i.e. a negative π-phase step). The amplitude of the response is multiplied by the amplitude of the corresponding part of the pump spectrum.

For the final part of equation 4.2, the shaped probe has to be convoluted with the narrow sample. This convolution can be approximated as the creation of two copies of the (shaped) probe spectrum with opposite phase, separated by a distance equal to the width of the resonance (rather like a differentiator). The result of this combination is an almost complete cancellation of the spectrum except in the vicinity of sharp transitions (such as the shaped π-step) where a sharp feature is created. When the π-phase step scans through the profile the sharp feature moves along with the step, creating a distinct feature with a slope of 1 in figure 4.10.

The second scenario is when the applied π-phase step overlaps with (and cancels) the molecular phase step. In this scenario, the sampling results in a copy of the amplitude of the molecular response except that it now has a flat phase. Therefore in the final convolution step with the probe spectrum, the full (shaped) probe spectrum is transferred to the final spectrum. This full transfer creates a vertical feature in figure 4.10(a-c) and an integrated effect in figure 4.10(d).

The two features cross at the Stokes plus resonance frequency. The vertical features in figure 4.10(b) are less pronounced because the phase of the resonance is not completely cancelled by the negative π-phase step over the full width of the resonance. The projection on the molecule (sampling) therefore does not produce a flat phase.

The broad, weak signals to either side in figure 4.10(a, b) are due to the flat parts of the pump and probe phase profiles.

Figure 4.11 shows a contour plot of the non-resonant CARS spectrum for a π-phase step sweep. Only one contour plot is shown here, because the sign of the phase has no influence on the non-resonant CARS contribution. The horizontal axis represents the location of the π-phase step and the vertical axis represents the non-resonant CARS spectra.

The non-resonant CARS spectra for any position of the π-phase step are explained in this paragraph. The non-resonant part of the CARS signal is the convolution of the pump, Stokes, and probe without the intermediate sampling. The spectral region around the phase shift acts as a local differentiator that samples the phase shift in the probe and creates a feature in the output. When the π-phase step is swept through the spectrum, the feature (the combination of a moving differentiator sampling a moving π-phase step) moves at twice the speed of the sweep and shows up as a feature of slope 2 in figure 4.11. The broad signals to either side of figure 4.11 are due the flat parts of the pump and probe phase profiles.

The combination of the resonant and non-resonant CARS signals is asymmetric, which is caused by the asymmetric phase of the vibrational resonance on the resonant CARS signal. Figure 4.12 shows contour plots of

π-phase step sweeps with (a) positive π-phase step, (b) negative π-phase step, and (c) the difference, where the horizontal axes represent the location of the π-phase step and the CARS-spectra are displayed along the vertical axes. Figure 4.12(d) shows the integrated CARS signals for the positive and negative phase steps. The horizontal axis represents the location of the π-phase step and the vertical axis represents the integrated CARS signal.

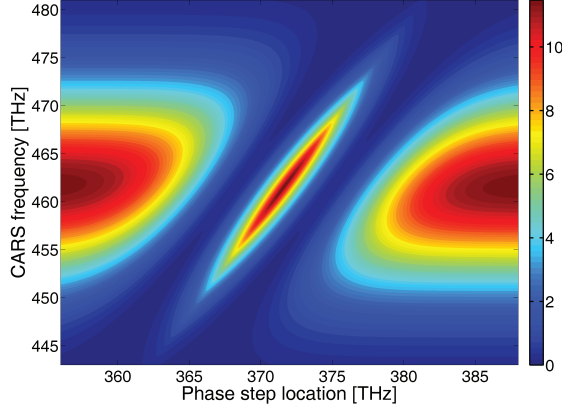*Figure 4.11: Non resonant CARS-spectra contour plot for a sweep with a positive (or negative) π-phase step.*

Figure 4.12: Simulation for the total CARS signal for one resonance. a) CARS spectra for a positive π-phase step sweep. b) CARS spectra for a negative π-phase step sweep. c) The difference between a negative and a positive π-phase step sweep. d) Integrated signals for the positive and negative π-phase step sweeps.

91

Since the non-resonant contribution is independent of the sign of the phase profiles, the difference contains only the resonant features. Note that resonant contributions from the flat parts of the phase profiles are also eliminated. However, the non-resonant contribution is still present as an overall gain factor. Since it is present in the spectral intensity because of the mixing term between the resonant and non-resonant contributions, it is also present in the difference plot, and the phase asymmetry causes an asymmetry in the difference plot.

Multiple separated resonances cause multiple features with slope 1 as well as multiple vertical features. This effect is shown in figure 4.13, which is similar to figure 4.12, but calculated for three resonances. Here these resonances are spaced 2 THz (67 cm^{-1}) apart (369.68, 371.68, and 373.68 THz), with equal strength of $\chi_R^{(3)}/\chi_{NR}^{(3)}=10$, and all 10 cm^{-1} wide.
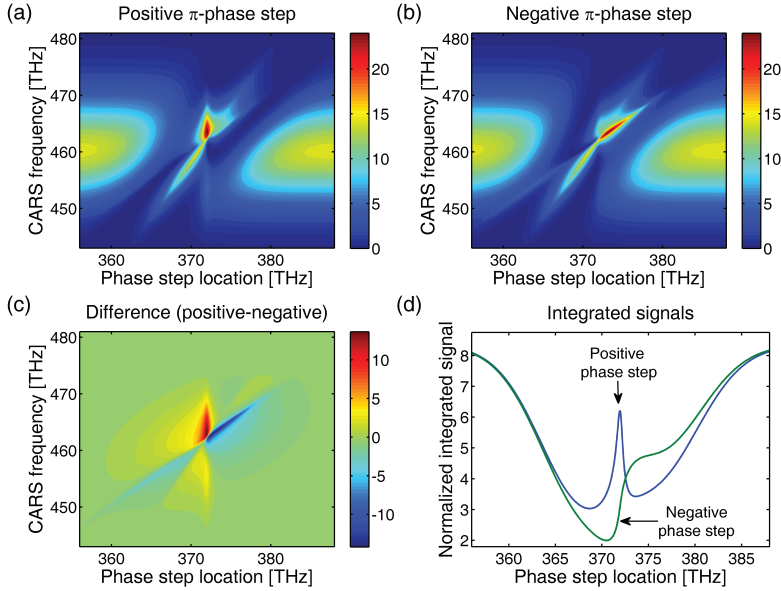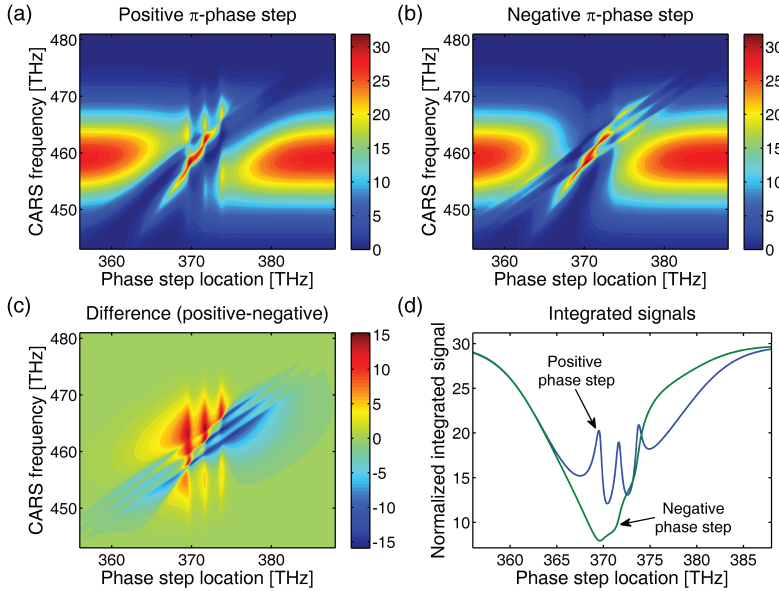

Figure 4.13: Simulation for the total CARS signal for three resonances. a) CARS spectra for a positive π-phase step sweep. b) CARS spectra for a negative π-phase step sweep. c) The difference between a negative and a positive π-phase step sweep. d) Integrated signals for the positive and negative π-phase step sweeps.

The total CARS signal is higher in figure 4.13 than in figure 4.12, due to the three vibrational resonances with the same strength as the vibrational resonance used in figure 4.12. Furthermore, all resonances are visible with the features with a slope of one and the vertical features. The resonance frequencies can be found by the crossing of the features with a slope of 1 with the non-resonant feature (slope of 2).

4.4.3   Spectroscopy on integrated signals

Spectroscopy on integrated signals has the advantage that it is not required to measure a spectrum, which increases the measurement time. In the next simulation a positive π-phase step, with of width of 10 cm^{-1} is swept through the pump and probe spectrum. Figure 4.14 shows the integrated resonant, non-resonant and the coherent sum of both contributions. The horizontal axis represents the location of the π-phase step and the vertical axis represents the integrated CARS signal, normalized to the total CARS signal for a flat spectral phase. When the compensating (positive) π-phase step is swept through the spectrum, a maximum of the integrated resonant CARS signal occurs when the π-phase step coincides with the resonance, despite the local spectral dip. The integrated non-resonant CARS signal is lowest when the π-phase step is in the center of the spectrum, and highest when the π-phase step is outside the laser spectrum. Hence, this sweeping method reveals resonances as local maxima that coincide with the position of the π-phase step.
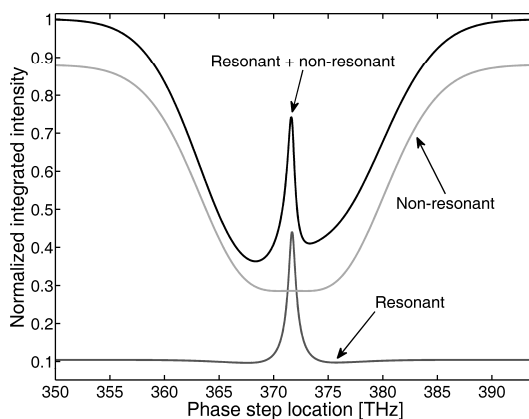
Figure 4.14: Integrated CARS signal for a sweep with a negative Lorentzian phase profile (10 cm^{-1}) (positive π-phase step).

Figure 4.14 shows furthermore that the addition of two seemingly symmetric CARS contributions (resonant and non-resonant) results in an asymmetric total CARS signal. This asymmetric shape is caused by the asymmetric phase of the vibrational resonance on the resonant CARS signal. This interference causes the local maximum of the *total* CARS intensity to occur at a slightly lower frequency for the π-phase step than the maximum of the *resonant* CARS contribution. The frequency difference in the local maximum of the total CARS signal and the maximum of the resonant contribution depends on the relative strengths of the resonant and non-resonant contributions and on the width of the π-phase step.

Further simulations show that weak resonances in the vicinity of the main vibration band shift the local maximum in the integrated CARS-signal. Also, closely spaced resonances reduce each others visibility and the visibility of transitions with a low cross-section requires a high signal-to-noise ratio for the CARS measurement. This simulation shows that resonances can be found by sweeping a phase step through the spectrum on integrated signals.

Figure 4.15 shows a simulation where the negative π-phase step, shown at the center of the band in figure 4.09, is now swept through the spectrum. The horizontal axis represents the location of the π-phase step, and the vertical axis represents the integrated CARS signal, normalized to the total CARS signal for a flat spectral phase.
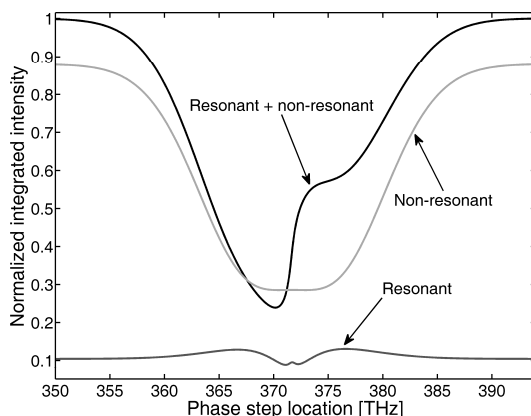
Figure 4.15: Integrated CARS signal for a sweep with a positive Lorentzian phase profile (10 cm^{-1}) (negative π-phase step).

The negative π-phase steps cause no local maxima in the integrated CARS signal, although a sudden increase is present at the location that matches the vibrational resonance. This increase is caused by more constructive interference for negative π-phase steps at higher frequency than the vibrational resonance plus Stokes. Parts of the phase profile of the resonant CARS spectra flips when a π-phase step is swept across the resonance plus Stokes frequency.

4.4.4 Extracting the line width and cross-section

The line width of one single resonance (or the effective line width of multiple closely spaced resonances) can be found by varying the 'slope' or width of the π-phase step, while keeping the step centered on the transition. When the width of a positive π-phase step matches the width of the vibrational resonance, the integrated resonant signal is maximized. Unfortunately, as the width of the π-phase step increases, the non-resonant

contribution also increases. The resonant features are again revealed by subtracting the results for a positive π-phase step from the results of a negative π-phase step. Figure 4.16 shows the integrated CARS signal for a positive π-phase step, a negative π-phase step, and the difference. The horizontal axis represents the width of the π-phase step in cm^{-1}. The integrated signal is shown on the vertical axis, normalized to the signal for a flat phase profile. The simulated vibrational resonance has a FWHM of 50 cm^{-1} (1.5 THz).
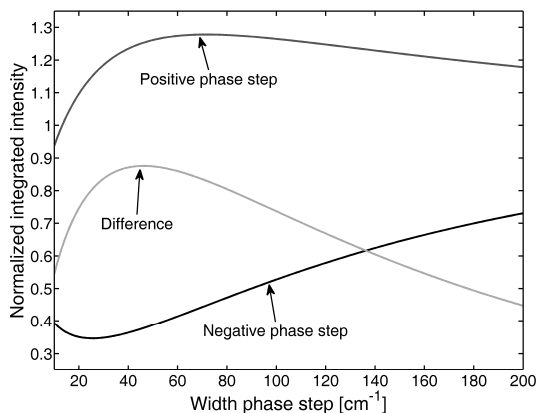
Figure 4.16: Integrated CARS signals as a function of the width of the phase profile. Dark grey line: positive π-phase step. Black line: negative π-phase step. Light grey line: the difference, for which the maximum indicates the line width of the resonance.

Figure 4.16, shows that the maximum of the difference signal does not directly yield the FWHM of the simulated vibrational resonance. The maximum also depends on the spectrum of the pump and probe pulses. But since this spectrum is known, the width can be extracted by fitting. The maximum is independent of the cross-section; the cross-section only influences the height of the difference.

Hence, the vibrational frequencies and line widths can be obtained by the previously described methods. In addition the relative cross-sections can be found by fitting the measurements to the theory, keeping the obtained frequencies and line width fixed, and varying the cross-section as a free parameter.

4.5 Measurements and discussion

Here experimental measurements that demonstrate the enhancement of the resonant part of the integrated CARS signal by use of a compensating (positive) π-phase step are presented. The molecule under investigation is acetone, which has a single strong resonance at 2923 cm^{-1} and several

neighboring weak resonances [112]. For the experiments the pump and probe pulses are identical with a center frequency of 12267 cm^{-1} (368 THz) and a spectral intensity FWHM of 277 cm^{-1} (8.3 THz). The Stokes pulse has a center frequency of 9396 cm^{-1} (282 THz) and a spectral intensity FWHM of 1 cm^{-1} (30 GHz). The acetone (Merck, purity > 99.5%) sample is sandwiched between a cover glass of thickness ~0.1 mm and a 1 mm thick microscope slide. Paraffin wax is used as spacer. First the CARS spectra are analyzed to find the vibrational resonances, then spectroscopy is performed on integrated signals and finally the effective line width and cross-sections are investigated.

4.5.1   Analyzing CARS spectra

First the non-resonant signal is investigated and compared to theory. The non-resonant signal is simulated by a second harmonic generation (SHG) process, which is the same as the non-resonant CARS process, except that the frequency of the SHG signal is higher. A π-phase step with a width of 5 cm^{-1} is swept through the spectrum of the pump and probe pulses and the SHG signal from a 10 μm thick BIBO crystal is measured. Figure 4.17 shows contour plots of measured SHG-spectra for a positive π-phase step sweep (a), a negative π-phase step sweep (b), the difference between the positive and negative steps (c), and the integrated SHG signal (d). The horizontal axes in all plots of figure 4.17 represent the location of the π-phase step, and the vertical axes show the CARS spectra (a-c) or the integrated CARS signal (d).

For the SHG process the sign of the phase clearly has no influence therefore no vertical features or features with a slope should be present in figure 4.17(c). The small vertical features present in figure 4.17(c) are ascribed to drift in the center frequency of the Ti:Sapphire laser. The small angled features remain unidentified. The overall conclusion is that figure 4.17 confirms the expectations shown in figure 4.11.

CARS spectra were measured on acetone. Figure 4.18 shows contour plots of measured spectra for a positive π-phase step sweep (a), a negative π-phase step sweep (b), the difference between the positive and negative steps (c), and the integrated CARS signal (d). The horizontal axes in all plots of figure 4.18 represent the location of the π-phase step, and the vertical axes show the CARS spectra (a-c) or the integrated CARS signal (d). The π-phase steps that were used have a width of 10 cm^{-1}.

Figure 4.17: Measurement of the SHG signals (width of 5 cm⁻¹). a) SHG spectra for a positive π-phase step sweep. b) SHG spectra for a negative π-phase step sweep. c) The difference between a positive and a negative π-phase step sweep. d) Integrated spectra for the positive and negative π-phase step sweeps.
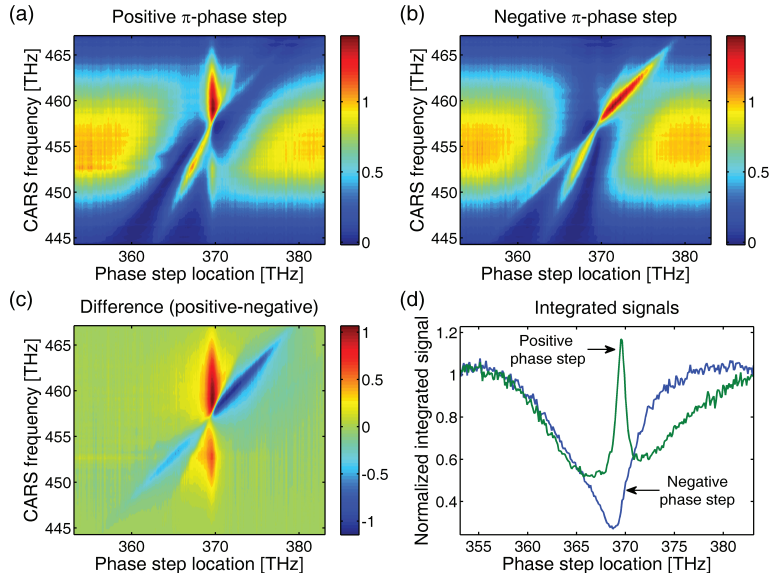
Figure 4.18: Measurement of the CARS signals (width of 10 cm⁻¹). a) CARS spectra for a positive π-phase step sweep. b) CARS spectra for a negative π-phase step sweep. c) The difference between a positive and a negative π-phase step sweep. d) Integrated spectra for the positive and negative π-phase step sweeps.

97

From the 2D plots, the main peak can be determined from the crossing point of the non-resonant feature (with a slope of 2) and the resonant feature (with a slope of 1) and is found to be 2923 cm^{-1}, matching the value from literature [112]. The other lines remain hidden in the noise of figure 4.19(c).

The signal-to-noise ratio is relative high with broad steps, as is clearly visible in figure 4.18. The resonance is visible as a feature with a slope of 1 in figure 4.18(c). Also the vertical features of the resonance are visible in figures 4.18(c) and (d).
The same measurement has been performed with a π-phase step with a width of 1 cm^{-1}. The result of this measurement is shown in figure 4.19.
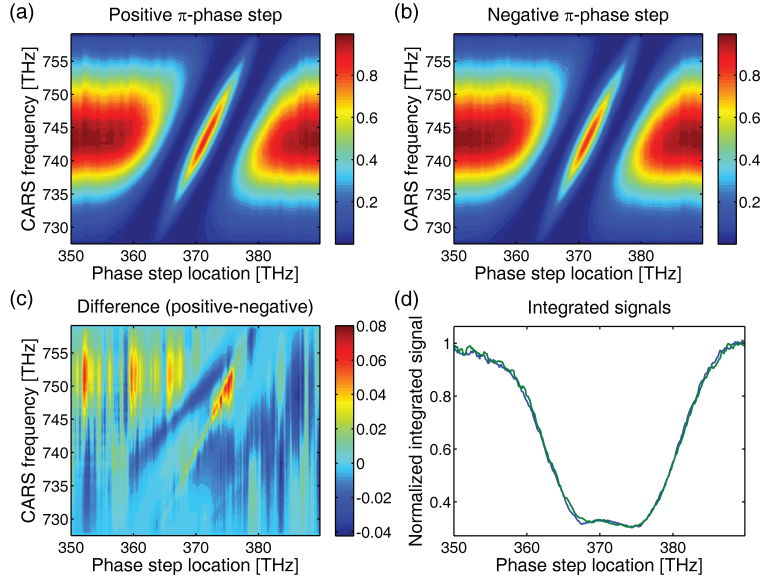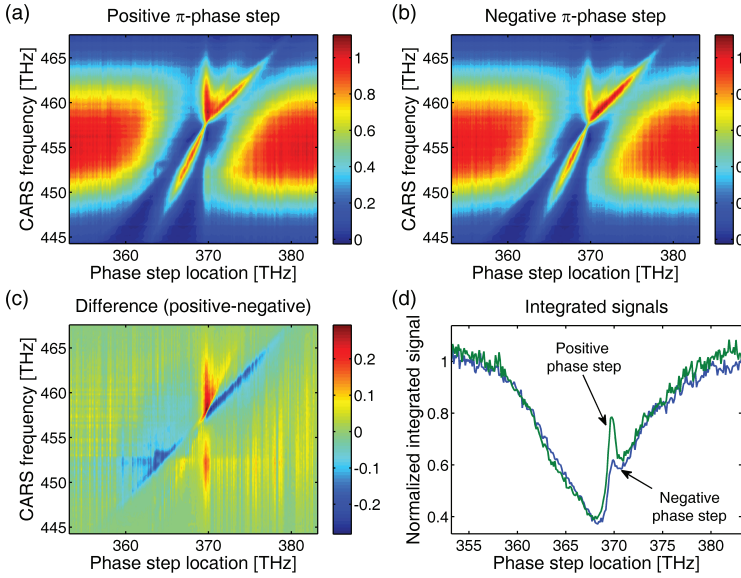

Figure 4.19: Measurement of the CARS signals (width of 1 cm^{-1}). a) CARS spectra for a positive π-phase step sweep. b) CARS spectra for a negative π-phase step sweep. c) The difference between a positive and a negative π-phase step sweep. d) Integrated spectra for the positive and negative π-phase step sweeps.

The sharper π-phase step gives a lower signal-to-noise ratio for the difference contour plot as is shown in figure 4.19(c). The advantage of the sharp π-phase step is that the integrated difference signal has only a significant value at the precise location in the pump and probe spectrum where the resonance is located. For π-phase steps at other frequencies the integrated signals are the same. With this narrow π-phase step, integrated measurements on single resonances are possible, as long as the resonance is strong enough to have a measurable difference between the positive and negative step. Other frequency regions are not influenced (as in the case of

broader π-phase steps). Therefore it is possible to selective measure one vibrational resonance with other resonances present on integrated spectra.

4.5.2 Spectroscopy on integrated signals

Figure 4.20 shows the experimental result for spectrally sweeping a positive π-phase step, with a width of 5 cm^{-1} (0.15 THz), through the pump and probe spectrum. The width of this π-phase step is a factor of four below the expected bandwidth of the main vibration [112]. The horizontal axis provides the location of the π-phase step, and the vertical axis shows the integrated CARS signal normalized to the total CARS signal for a flat spectral phase.
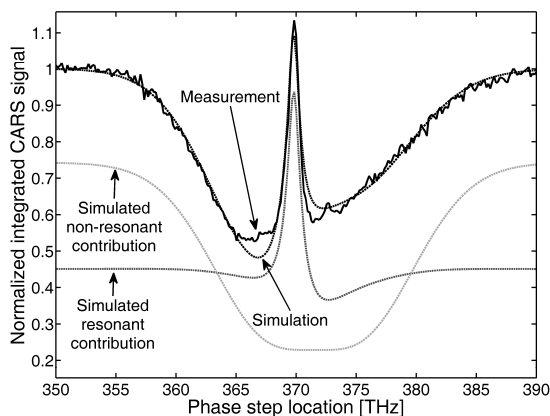
Figure 4.20: Normalized integrated CARS signal for acetone, with a positive π-phase step swept through the spectrum of the pump and probe pulses.

Figure 4.20 shows one strong resonance for a π-phase step at 369.82 THz, corresponding to a resonance frequency of 2940 cm^{-1}, slightly higher than the expected Raman frequency of 2923 cm^{-1} [112]. The shift can be explained by interference effects from the smaller vibrational resonances within a window of 100 cm^{-1} (3 THz). This example shows that the method works best for strong isolated resonances. The simulation is calculated using one vibrational resonance where the line width and the cross-section (compared to the non-resonant background) are varied. The fit parameters are 26 cm^{-1} for the line width and 25 for $\chi_R^{(3)} / \chi_{NR}^{(3)}$ (amplitude).

4.5.3 Line width and cross-section

As shown in the section 4.4.4, the line width for a single resonance can be examined by tweaking the width of the π-phase step at the vibrational band and comparing the integrated CARS spectra. However, a real molecule has

many resonances. Even in the case of acetone the weak resonances that are present near the strong resonance influence the measurement. This influence is shown in figure 4.21. Figure 4.21(a) shows measurement data on acetone with a fit that assumes only one vibrational resonance. Figure 4.21(b) shows the data where all five resonances in the vicinity are taken into account. On the horizontal axis the width of the π-phase step is plotted and the vertical axis shows the integrated CARS signals, normalized to the Fourier limited signal.
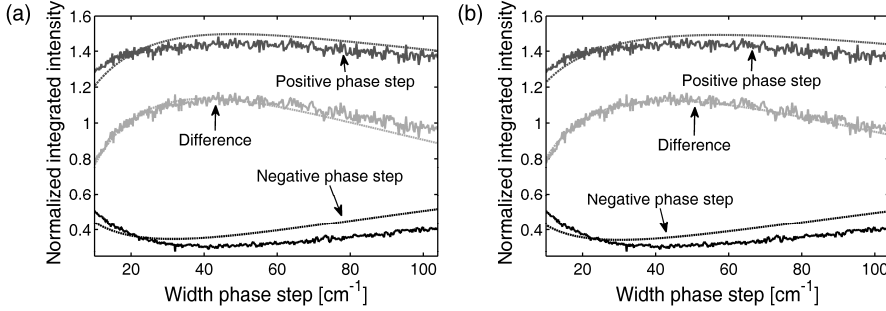
Figure 4.21: Effective line width estimation of acetone. a) Fitted to one transition. b) Fitted to five transitions.

The simulated lines in figure 4.21(a) correspond to a vibrational resonance at 2936 cm^{-1}, a value of 10 for the ratio $\chi_R^{(3)}/\chi_{NR}^{(3)}$ (amplitude), and a line width of 38 cm^{-1}. This line width is much broader than the one determined from the measurement shown in figure 8 (23 $\pm$ 2 cm^{-1}). This difference is attributed to the influence of the smaller resonances near the main resonance. Thus figure 4.21(a) yields an effective line width and effective line amplitude. Figure 4.21(b) shows the result when 5 lines are used with vibrational frequencies (2698 cm^{-1}, 2850 cm^{-1}, 2923 cm^{-1}, 2966 cm^{-1}, and 3004 cm^{-1}), free line amplitudes (8, 1, 27, 12, 12 for $\chi_R^{(3)}/\chi_{NR}^{(3)}$) and free line widths (17 cm^{-1}, 22 cm^{-1}, 16 cm^{-1}, 26 cm^{-1}, 11 cm^{-1}). The vibrational frequencies are taken from literature [112]). Fitting the measurements to five resonances improves the simulated difference line in comparison to the fit to a single resonance.

4.6 Summary and recommendations

In this chapter a new spectral phase shaping strategy is demonstrated for CARS spectroscopy. Vibrational transitions can be identified with a resolution limited by the resolution of the shaper (0.5 cm^{-1}). Furthermore a method is introduced for measuring the line width of isolated spectral lines and measuring an effective line width for a combination of lines. Relative

cross-sections can be extracted from the data on the spectral sweeps. Also the possibility is shown to remove the non-resonant contribution for materials which have no resonances in the frequency range covered by the energy difference of the pump and Stokes pulses.

Chapter 5

Chemically selective imaging using phase shaped CARS

5.1 Introduction

In this chapter, chemically selective imaging using broadband pump and probe pulses is presented. The chemical selectivity originates from the phase profiles applied to the pump and probe pulses. The difference in CARS signals for a positive phase profile and the inverse (negative) of that phase profile is used to reject non-resonant components. For the Stokes a narrowband pulse is used. A mixture of polystyrene (PS) and polymethylmethacrylate (PMMA) beads on a glass substrate is used to demonstrate this method.

This chapter starts with a short description of the setup (5.2). Then, explanation of the method used to achieve chemical contrast with phase shaped pump and probe pulses is provided, followed by simulation of spectra for one vibrational band and measurements on PS and PMMA beads (5.3). In the following section phase profiles are used to demonstrate chemical selective imaging (5.4). This section is followed by calculations to show the effect on the integrated CARS signal for more complex phase profiles (5.5).

5.2 Setup

The setup is similar to the setup described in section 4.3. A schematic of the setup is shown in figure 5.1.
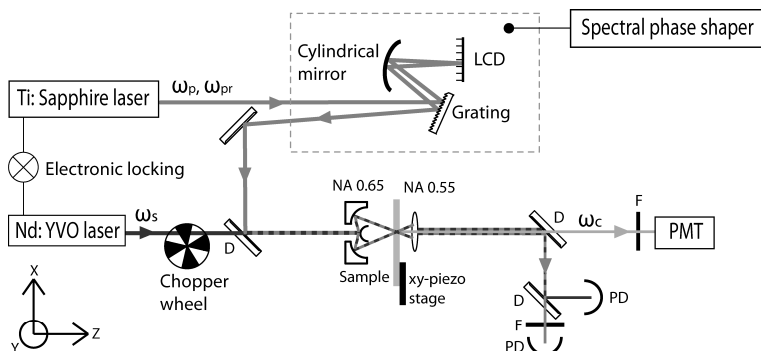
Figure 5.1: Schematic of the setup. LCD (liquid crystal device), D (dichroic), F (short pass filter), PD (photodiode), and PMT (photomultiplier tube).

A tunable Ti:Sapphire oscillator, with a center frequency of 372 THz (806 nm, 12409 cm^{-1}), intensity FWHM of 5.1 THz (11 nm, 170 cm^{-1}), and 0.44 nJ per pulse just before the reflective objective at a repetition rate of 80 MHz, is used for the pump and probe pulses of the CARS process. This laser is actively synchronized to a mode-locked Nd:YVO laser, which is used for the Stokes pulse. The Nd:YVO laser has a center frequency of 281.7 THz (1064.3 nm,), intensity FWHM of 30 GHz (1 cm^{-1}), and 1.75 nJ per pulse just before the reflective objective at a repetition rate of 80 MHz. The light of the Nd:YVO laser is modulated by a chopper, at 1.7 kHz. The modulation frequency is chosen such that DC signals are rejected and that imaging can be done with an integration time of 10 ms per pixel.

The spectral phase shaping of the pump and probe beams is done with a spectral phase shaper (described in chapter 2). The pulses of the Ti:Sapphire laser are pre-compressed by an external prism compressor and shaped to be transform limited (at the position of the sample) by the spectral phase shaper using an evolutionary learning algorithm discussed in section 2.7. The desired spectral phase functions for the experiments and the higher order dispersion correction are also applied by the spectral phase shaper.

A reflective objective of 0.65 NA is used to focus the light into the sample. A reflective objective has been chosen to prevent dispersion and chromatic aberration. The collection objective is a 0.55 NA regular glass objective. The sample is scanned using two piezoelectric devices in the xy-plane. A light emitting diode and a quadrant cell are used for position feedback of the sample. The collected light is detected on a photomultiplier tube (PMT). The PMT signal is pre-amplified and further amplified with a lock-in amplifier. The original laser pulses are split from the CARS signal after the collection objective and used to measure the transmission images of both laser sources independently. An extra short pass filter which passes light with a wavelength shorter than 1 μm is placed in front of the photodiode for the

transmission of the Ti:Sapphire laser. For the other photodiode an additional long pass filter is not required.

Note that the locking of both lasers is done only using the electronic locking scheme (see section 4.3). The optical locking scheme (see section 4.3) is not used because the optical locking scheme requires a constant amount of light, and the transmitted light level is not constant in these samples.

5.3 Phase scan method

This section starts with simulations of the integrated total CARS signal for positive and negative π-phase step sweeps. The resonances are chosen such that they match with the main vibrational resonance of PS and PMMA. The vibrational resonances of PS and PMMA are weaker than the vibrational resonance of acetone, therefore it is chosen to take the maximum value of $\chi_R^{(3)}$ 2.5 times the value of $\chi_{NR}^{(3)}$, which is 4 times weaker than the value used in the simulations of chapter 4. Note that the intensity of the resonant contribution is quadratically dependant on $\chi_R^{(3)}$. Further measured and fitted Raman spectra of PS and PMMA are shown. Furthermore traces are presented, where several resonances around 90 THz (3000 cm^{-1}) are taken into account. The last part of this section shows the results of phase step sweeps on 4 μm PS and PMMA beads. From these measurements the phase step frequency and the width of the phase step is determined for optimal chemical contrast. Furthermore the expected contrast between PS and PMMA is calculated for a double step which enhances the main vibrational band of PMMA and decreases the main vibrational band of PS.

5.3.1 Simulated traces

The integrated total CARS signal of a positive and negative π-phase step sweep are simulated for one vibrational resonance. The properties of this vibrational resonance are chosen to be similar to the main vibrational resonance of PS around 90 THz (3000 cm^{-1}). The intensity FWHM of this resonance is 35 cm^{-1} and its maximum is located at 91.56 THz (3054 cm^{-1}) [28]. The center of the vibrational resonance plus the Stokes frequency is at 373.24 THz; thus for positive π-phase steps sweeps the maximum of the resonant CARS signal is located at this frequency. The simulation is performed with the model described in section 4.4. The parameters of the simulated pump and probe are equal to settings of the Ti:Sapphire laser which is used to perform the chemically selective imaging (center frequency of 372 THz, intensity FWHM of 5.1 THz).

Figure 5.2(a) shows the integrated CARS signal for positive π-phase step sweeps for several phase step widths (5, 10, 20, 50, and 100 cm^{-1}). Figure 5.2(b) shows the integrated CARS signal for negative π-phase step sweeps for the same set of phase step widths as in figure 5.2(a). The horizontal axes represent the location of the π-phase step and the vertical axes represent the integrated CARS signal, normalized to the integrated CARS signal for a flat spectral phase.

Figure 5.2: Integrated CARS signal for sweeps with a π-phase step for phase step widths of 5, 10, 20, 50, and 100 cm^{-1}. a) For positive π-phase step sweeps. b) For negative sweeps. The vertical line indicates the position of the resonance.

The simulation for the positive phase step, shown in figure 5.2(a), shows that the local maximum shifts to lower frequencies for the positive π-phase step as the width of the phase step increases. This shift of the local maximum as function of the width is caused by the interference between the non-resonant and the resonant CARS contributions as explained in chapter 4. Furthermore the integrated total CARS signal at the local maximum increases with the bandwidth of the phase step. This increase of the maximum as function of the width of the π-phase step is caused by the increase of the non-resonant CARS signal due to the reduced steepness of the phase profiles for large widths of the π-phase step. According to other simulations the *resonant* CARS signal is maximized for the case where the width of the π-phase step matches with the width of the vibrational resonance, in this case 35 cm^{-1}.

The simulation for the negative π-phase step, figure 5.2(b), shows no local maxima in the vicinity of the vibrational resonance. Figure 5.3 shows the difference in integrated signal for a positive and a negative π-phase step. This difference is defined as the CARS signal for a positive π-phase step minus the CARS signal for a negative π-phase step. The horizontal axis represents the location of the π-phase step and the vertical axis represents the integrated difference CARS signal, normalized to the total CARS signal for a flat spectral phase.

Figure 5.3: The difference of the integrated CARS signal for a positive and a negative π-phase step sweep for phase step widths of 5, 10, 20, 50, and 100 cm⁻¹. The vertical line indicates the position of the resonance.

For one single resonance and for π-phase steps at a higher frequency than the vibrational resonance plus the Stokes frequency, the simulations show that the CARS difference signal has a negative value. The FWHM of the maximum of the integrated difference signal increases if the width of the phase steps increases. Furthermore the absolute value of the maximum integrated difference value increases if the width of the phase step increases until a certain optimum, which depends on the relative strengths of the resonant and non-resonant CARS signals. The higher this integrated difference value is, the higher the signal-to-noise ratio of the images will be. Therefore the choice of the width of the phase step depends on the spectral resolution of interest and the signal-to-noise ratio of the measurements.

The main vibrational resonance of PMMA is located at 88.41 THz (2949 cm⁻¹) [113]. For this vibrational resonance a similar simulation is performed. The same parameters are used as in the case of PS, except for the vibrational frequency, which is located at the red side of the pump minus Stokes spectrum. Figure 5.4(a) shows the integrated CARS signal for positive π-phase step sweeps for the following phase step widths (5, 10, 20, 50, and 100 cm⁻¹). Figure 5.2(b) shows the integrated CARS signal for negative π-phase step sweeps for the same phase step widths. Again the horizontal axes represent the location of the π-phase step and the vertical axes represent the integrated CARS signal, normalized to the total CARS signal for a flat spectral phase.
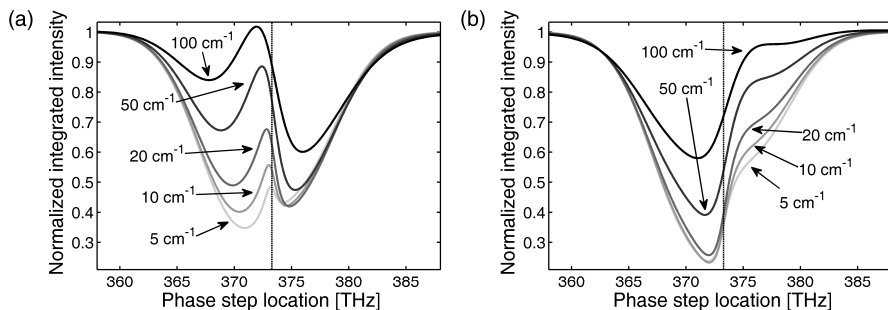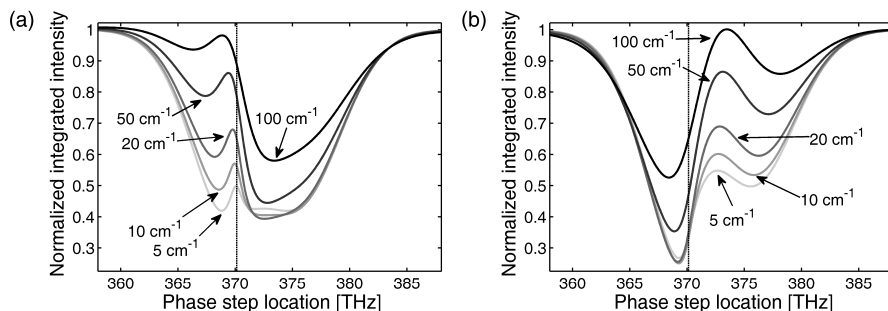
Figure 5.4: Integrated CARS signal for sweeps with a π-phase step for phase step widths of 5, 10, 20, 50, and 100 cm⁻¹. a) For positive π-phase step sweeps. b) For negative sweeps. The vertical line indicates the position of the resonance.

The behavior for different positive π-phase step sweeps is the same as in the calculated case for the vibrational resonance at 91.56 THz (3054 cm⁻¹), only it is shifted to lower frequencies, due to the lower vibrational frequency. For the negative π-phase step the enhancement on the blue side is more pronounced and exceeds even the signal levels for transform limited pulses for phase steps with a width of more than 100 cm⁻¹. This enhancement is due to the phase alignment of the non-resonant CARS and the resonant CARS contributions. Figure 5.5 shows the integrated difference signal for the set of positive and negative π-phase step sweeps. The horizontal axis represents the location of the π-phase step and the vertical axis represents the integrated difference CARS signal, normalized to the total CARS signal for a flat spectral phase.
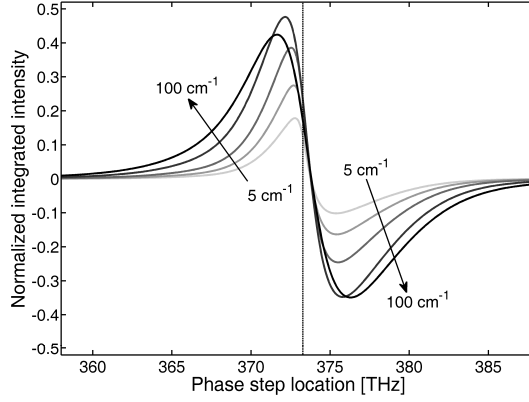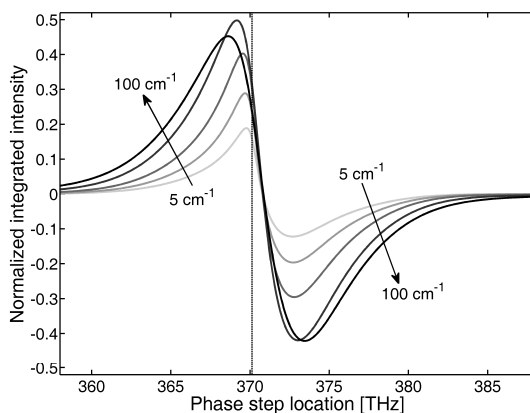

Figure 5.5: The difference of the integrated CARS signal for a positive and a negative π-phase step sweeps for phase step widths of 5, 10, 20, 50, and 100 cm⁻¹. The vertical dashed line indicates the position of the resonance.

The simulated difference signal shown for this resonance is similar to the simulated difference signal shown in figure 5.3. The main difference is the

shift in the zero crossing of the phase step location due to the change in vibrational frequency. The changes in the relative heights of the maxima and minima are caused by the spectral intensity of the pump and probe pulses at these spectral locations of the π-phase step.

From these simulations it can be concluded that a negative difference signal is expected for π-phase steps that have a higher frequency than the vibrational resonance frequency plus the Stokes frequency. A positive difference signal for π-phase steps is expected on or below the vibrational resonance frequency plus the Stokes frequency.

5.3.2   Raman spectra of PS and PMMA

The simulations shown in the first part of this section are for a single vibrational resonance but PS and PMMA have more resonances in the 80 – 100 THz range. The measured Raman spectra of PS and PMMA are fitted by eye with the model presented in section 4.4. Figure 5.6(a) shows a measured Raman trace of PS with a fit according to the model and the calculated phase of the vibrational resonances. Figure 5.6(b) shows the same for PMMA. The horizontal axes represent the frequency and the vertical axes represent the Raman strength divided by the maximum Raman strength in the shown region.
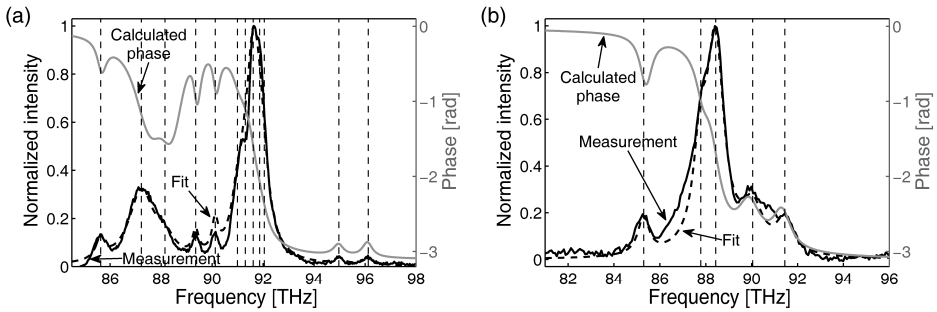
Figure 5.6: Raman spectra of PS (a) and PMMA (b), with calculated fit and phase.

The measured Raman spectrum of PS is fitted with twelve resonances and for PMMA it is fitted with five resonances. The frequencies, widths, and relative amplitudes of the resonances of PS and PMMA are presented in table 5.1.

	PS			PMMA		
#	Frequency [THz] ([cm^{-1}])	Width [cm^{-1}]	Ampli-tude	Frequency [THz] ([cm^{-1}])	Width [cm^{-1}]	Ampli-tude
1	85.62 (2856.0)	14	0.088	85.29 (2845.0)	20	0.115
2	87.22 (2909.5)	40	0.875	87.78 (2928.0)	24	0.359
3	88.14 (2940.0)	30	0.175	88.42 (2949.5)	30	1
4	89.35 (2980.5)	10	0.075	90.03 (3003.0)	38	0.282
5	90.12 (3006.0)	10	0.100	91.44 (3050.0)	30	0.167
6	90.99 (3035.0)	20	0.250			
7	91.29 (3045.0)	20	0.250			
8	91.60 (3055.5)	20	1			
9	91.86 (3064.0)	20	0.500			
10	92.04 (3070.0)	20	0.175			
11	94.97 (3168.0)	16	0.030			
12	96.11 (3206.0)	16	0.033			

Table 5.1: The fitted parameters of the resonance of PS and PMMA in the 80 – 100 THz range

5.3.3 Experimental π-phase step sweeps

The measurements are done on PS or PMMA beads, with a diameter of 4 μm, dried on a glass substrate. The phase scan sweeps with a positive and negative π-phase step for phase step widths of 10, 20, and 50 cm^{-1} are applied to the spectrum pump and probe beams. Here the beams are centered on a bead. Figure 5.6 shows the measured and simulated integrated CARS signals for π-phase step sweeps. Figure 5.7(a) shows the results for positive π-phase step sweeps and figure 5.7(b) shows the results for negative π-phase step sweeps. The horizontal axes represent the location of the π-phase step and the vertical axes represent the integrated CARS signal normalized to the total CARS signal for a flat spectral phase profile.

The measurements for the positive π-phase step show the enhancement of the main vibrational resonance of PS at 3054 cm^{-1} for π-phase steps located at 372-373 THz. Just as in the simulations the local maxima shift to lower frequencies for increasing the width of the positive π-phase steps. The sudden increase in signal at 369.5 THz in the measurements for the negative π-phase step sweep with a width of 50 cm^{-1} phase step might be caused by the broad vibrational resonance with its maximum at 2902 cm^{-1}, although that this increase is not visible in the simulated traces.

Figure 5.7: Integrated CARS signal from a PS bead for π-phase step sweeps with widths of 10, 20, and 50 cm^{-1}. a) For positive π-phase step sweeps. b) For negative sweeps. Solid lines are the measurements, dashed lines are the simulations. The vertical line indicates the position of the main resonance.

Figure 5.8 shows the measured and simulated integrated difference signal for the set of positive and negative π-phase step sweeps. The horizontal axis represents the location of the π-phase step and the vertical axis represents the integrated difference CARS signal, normalized to the total CARS signal for a flat spectral phase.

Figure 5.8: The difference of the integrated CARS signal from a PS bead for a positive and a negative π-phase step sweep for phase step widths of 10, 20, and 50 cm^{-1}. Solid lines are the measurements, dashed lines are the simulations. The vertical dashed line indicates the position of the main resonance.

The measured difference signal of the PS beads shows a negative slope at 373 THz for all three widths of the phase step that also appears in the simulations. For phase step locations at the blue side of the resonance plus Stokes frequency the measured difference signal is less negative than the simulations. The maximum at 368 THz for the 50 cm^{-1} phase step width is most likely caused by noise; this conclusion is based on the sudden decrease

in signal of the negative π-phase step sweep with a width of 50 cm⁻¹ (figure 5.8(b)).

Based on these traces the difference CARS signal between a positive and a negative π-phase step at 372.7 THz with a width of 20 cm⁻¹ is used as indicator for PS, for the imaging experiments in section 5.4.2.

The same measurement and simulation is performed on PMMA beads. PMMA has a lower cross-section than PS. A maximum value for $\chi_R^{(3)}$ of 2 times the value of $\chi_{NR}^{(3)}$ matches better the simulations and measurements. Figure 5.9 shows the measured sweeps. Figure 5.9(a) shows the measurements and simulations for a positive π-phase step sweeps and figure 5.9(b) for negative sweeps. The horizontal axes represent the location of the π-phase step and the vertical axes represent the integrated CARS signal divided by the CARS signal for a flat phase profile.
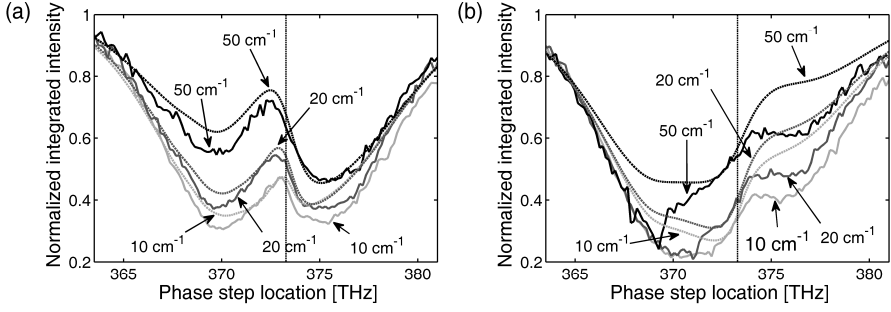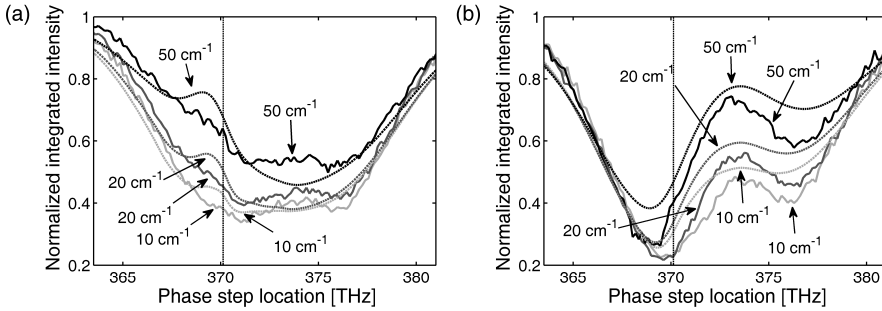

Figure 5.9: Integrated CARS signal from a PMMA bead for π-sweeps with widths of 10, 20, and 50 cm⁻¹. a) For positive π-phase step sweeps. b) For negative sweeps. Solid lines are the measurements, dashed lines are the simulations. The vertical line indicates the position of the main resonance.

PMMA lacks resonances of sufficient strength to generate a local maximum in the positive π-phase step sweeps. The local maxima for the negative π-phase step are broad. Figure 5.10 shows the measured and calculated integrated difference signal for the set of positive and negative π-phase step sweeps. The horizontal axis represents the location of the π-phase step and the vertical axis represents the integrated difference CARS signal, normalized to the total CARS signal for a flat spectral phase.
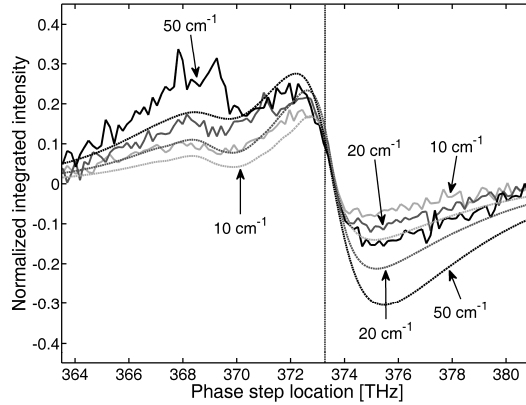
The measured difference signal shows a negative slope at 370 THz for all three widths of the phase step. This is also according to the simulations. For phase step locations at the blue side of the resonance plus Stokes frequency the difference signal is less negative than the simulations as was also the case for PS. There was no further investigation done to find the reason for this difference.
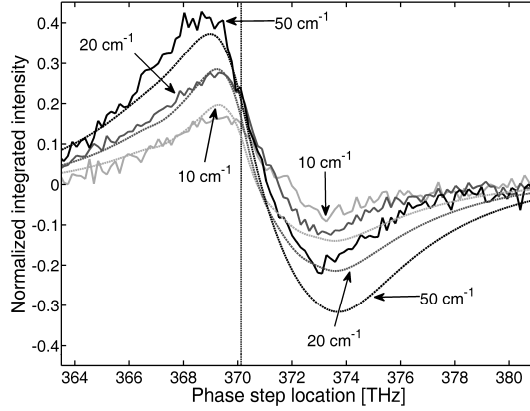
Figure 5.10: The difference in the integrated CARS signal from a PMMA bead for a positive and a negative π-phase step sweep for phase step widths of 10, 20, and 50 cm^{-1}. Solid lines are the measurements, dashed lines are the simulations. The vertical line indicates the position of the main resonance.

Based on these measurements the difference between a positive and a negative π-phase step at 369.0 THz with a width of 20 cm^{-1} is used as indicator for PMMA in the imaging experiment shown in section 5.4.2.

5.3.4   CARS imaging with a double phase step

If two opposite phase steps are applied it is for example possible to decrease the CARS signal from the main vibrational resonance of PS, and increase it for PMMA. Figure 5.11 shows the shape of the phase profiles for one phase step that compensates partly the phase of PMMA and a positive phase step at slightly lower frequency than the main resonance frequency of PS. These phase profiles are shown for three widths (10, 20, 50 cm^{-1}) of both of the phase steps. The locations are chosen such that they match with the maxima in figure 5.8 and 5.10. The horizontal axis represents frequency and the vertical axis represents phase.

The locations of the phase steps are 369.3 and 373.1 THz for phase steps with a width of 10 cm^{-1}, 369.0 and 372.7 THz for phase steps with a width of 20 cm^{-1}, and 368.7 and 372.5 THz for phase steps with a width of 50 cm^{-1}. The expected integrated CARS signal, of the phase steps shown in figure 5.11 with the phase steps for the different sign for the materials PS and PMMA, are calculated and presented in table 5.2. For the estimation of the integrated CARS signal the fitted spectra from the Raman measurements on PS and PMMA are used. The strength of the maximum value of $\chi_R^{(3)}$ is 2.5 for PS and 2 for PMMA times the value of $\chi_{NR}^{(3)}$.
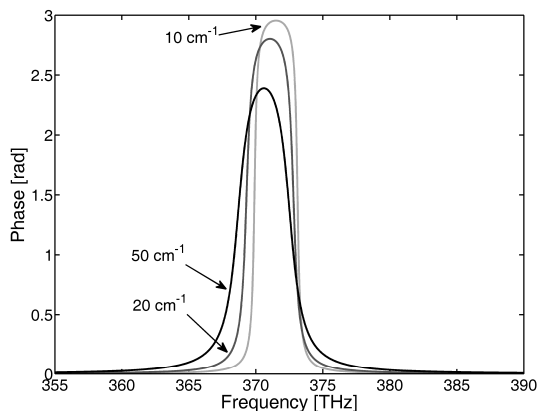
Figure 5.11: The phase profiles for three different widths of the π-phase steps.

Material (width phase steps [cm^{-1}])	Positive step and negative step	Negative step and positive step	Difference
PS (10)	0.1672	0.2413	-0.0741
PMMA (10)	0.2685	0.1945	0.0740
PS (20)	0.1714	0.2773	-0.1059
PMMA (20)	0.3094	0.1827	0.1267
PS (50)	0.2990	0.3974	-0.0984
PMMA (50)	0.5020	0.2311	0.2708

Table 5.2: The expected effect on the CARS signal of a π-phase step at the maximum difference for PMMA and an opposite π-phase step at the maximum difference for PS. In parentheses the width of the phase steps is given. The calculated CARS signals are divided by the CARS signal for a transform limited pulse.

As expected, the difference signal for PS has a negative value, and the difference signal for PMMA has a positive value. Based on these calculations the difference of the phase profiles with a width of 20 cm^{-1} is used in the imaging experiment shown in section 5.4.3.

5.4 Chemically selective imaging

This section starts with transmission images of PS and PMMA beads that show no contrast between the two types of beads. Further images are shown obtained by applying the phase steps that were explained in section 5.3.2. An image is also shown where the double phase step of section 5.3.4 is applied to the pump and probe pulses.

5.4.1 Transmission

Two photodiodes measure the transmitted light of the Ti:Sapphire laser (pump and probe pulses) and the Nd:YVO laser (Stokes pulse). Using the light from the Ti:Sapphire laser has the disadvantage that the beam profile of this light source is distorted due to the spectral phase shaper setup, as is discussed in chapter 2. There are however also two advantages; the shorter wavelength (thus smaller diffraction limited focal spot size) and this beam is not modulated by the chopper. For comparison, the transmission images of the same sample using both laser sources are presented. Figure 5.12 shows both measured transmission images (inverted) of the same mixture of PS and PMMA beads on a glass substrate. The scan range is 55 x 55 μm^2 (234 x 234 pixels). The color bars indicate the maximum transmission minus the local transmission, normalized to the maximum transmission. For the image of the Stokes pulse the chopper is turned off.
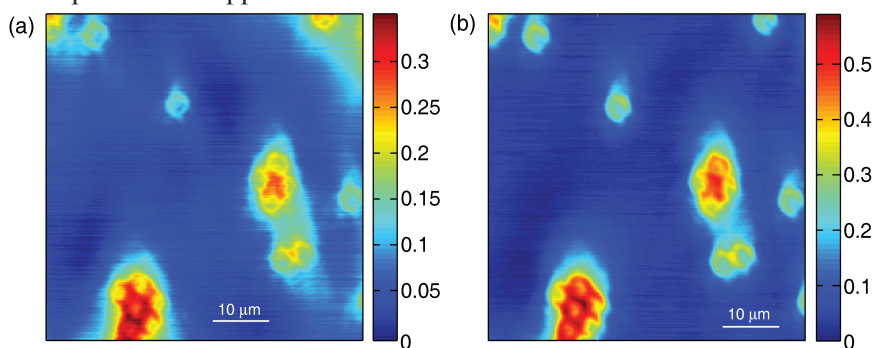
Figure 5.12: Inverted transmission images on a mixture of PS and PMMA beads (4 μm). a) For the pump and probe pulses. b) For the Stokes pulse.

The contrast of the Stokes pulse is better, because the spatial beam profile of this beam is closer to a Gaussian profile. The beads also scatter more light at the Stokes wavelength. It is not possible to identify which beads are PS or PMMA in these images.

5.4.2 CARS imaging with a single π-phase step

The first applied profile is a π-phase step at 372.7 THz with a width of 20 cm^{-1}. With this phase step, the difference signal for the PS beads is expected to be positive. Furthermore, the frequency of this phase step is located at the blue side of the main resonances of PMMA. This implies a negative difference signal for the PMMA beads.

Figure 5.13 shows the CARS images for (a) a positive π-phase step, (b) a negative π-phase step, (c) the difference, and (d) for a transform limited

phase profile. The color bars indicate the CARS signal strength divided by the maximum CARS signal for the transform limited pulse.

The contrast in figure 5.13 is better than that in figure 5.12, because the transmission image (figure 5.12) is not confocally measured, while CARS, results in inherently confocal images (figure 5.13). Furthermore the resolution increases due to the third order non-linearity [114]. A clear difference between different types of beads is visible in the difference image but also for the transform limited pump and probe pulses, because PS has a larger total cross-section than PMMA in this region. As expected, the PS beads have a positive difference signal, and the PMMA beads have a slightly negative signal.

The second applied profile is a π-phase step at 369.0 THz with a width of 20 cm^{-1}. With this phase step, the difference signal of the PMMA beads is expected to be positive. However PS has also a positive difference signal for this phase step, which causes limited contrast between these two materials. Figure 5.14 shows CARS images of the same mixture of PS and PMMA beads on a glass substrate with (a) a positive π-phase step, (b) a negative π-phase step, (c) the difference, and (d) for a transform limited phase profile. The color bars indicate the CARS signal strength divided by the maximum CARS signal for the transform limited pulse.

The applied phase step does not make a strong difference in the difference image signals. Although if figure 5.14(c) normalized to figure 5.14(d) in a pixel by pixel basis than the difference signal from the PMMA beads gets boosted compared to the difference signal from the PS beads.

(a) Positive π−step

(b) Negative π−step

(c) Positive − negative

(d) Transform limited
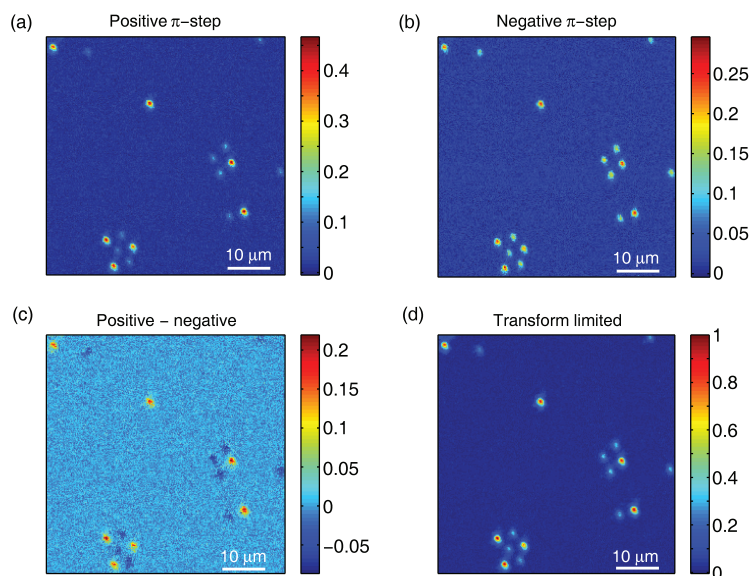
Figure 5.13: CARS images of PS and PMMA beads. a) For the positive π-phase step (at 372.7 THz, width of 20 cm^{-1}). b) For the negative π-phase step. c) Difference image of a) and b). d) For a flat phase profile.

(a) Positive π−step

(b) Negative π−step

(c) Positive − negative

(d) Transform limited
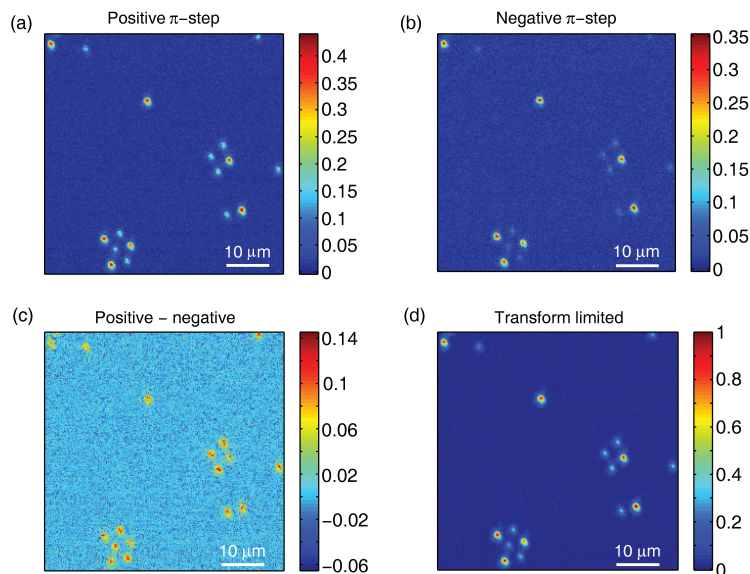
Figure 5.14: CARS images of PS and PMMA beads. a) For the positive π-phase step (at 369.0 THz, width of 20 cm^{-1}). b) For the negative π-phase step. c) Difference image of a) and b). d) For a flat phase profile.

5.4.3 CARS imaging with a double phase step

Figure 5.15 shows the measured CARS images for the double phase steps of section 5.3.4 with (a) a positive π-phase step, (b) a negative π-phase step, (c) the difference, and (d) for a transform limited phase profile. The color bars indicate the CARS signal strength divided by the maximum CARS signal for the transform limited pulse.
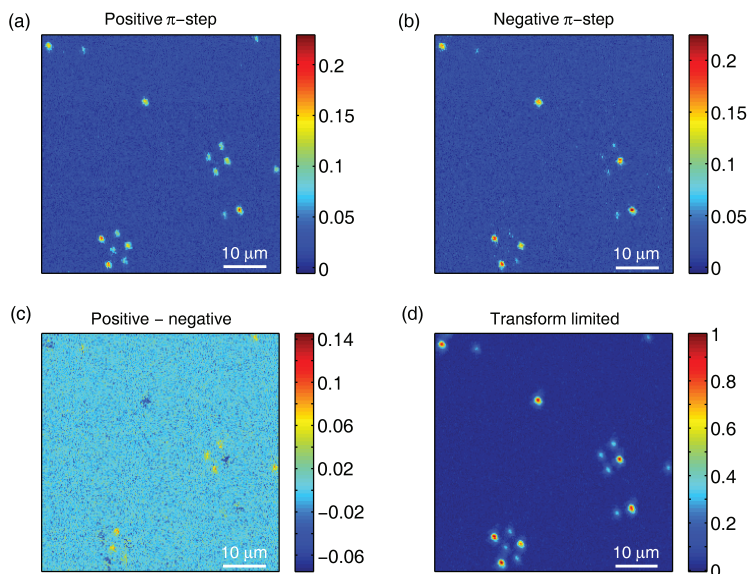
Figure 5.15: CARS images of PS and PMMA beads. a) For a positive π-phase step at 369.0 THz with a width of 20 cm^{-1} and a negative π-phase step at 372.7 THz, with a width of 20 cm^{-1}. b) for an opposite phase profile. c) Difference image of a) and b). d) For a flat phase profile.

Figure 5.15(c) shows that this relative simple phase profile creates a positive difference CARS signal for PMMA and a negative difference CARS signal for PS. The difference CARS signal for PS is low, as expected from the calculations presented in table 5.2. The difference image therefore shows the suppression of the PS signal and enhancement of the PMMA signal. With these results, the possibility to chemically selective imaging has been demonstrated.

5.5 Outlook, the use of molecular phase profiles

In this section a discussion is presented on the use of phase profiles that consist of the complete molecular response, rather than a single π-phase step. Two vibrational spectra of real molecules are used, namely PS and PMMA.

For these two molecules simulations are performed where the compensating phase profile is applied to the pump and probe pulses. However the concurrent phase profile in the probe pulse is not required for the compensation of the molecule. Therefore simulations are also performed where a phase profile is applied only to the pump pulse and where the probe remains transform limited.

PS and PMMA both have relatively simple molecular phase profiles in this range, therefore also calculations are shown for a richly structured profile of a virtual molecule. In this section the maximum value of $\chi_R^{(3)}$ is 2.5 times the value of $\chi_{NR}^{(3)}$ for PS and the virtual molecule and the maximum value of $\chi_R^{(3)}$ is 2 times the value of $\chi_{NR}^{(3)}$ for PMMA. The spectra of the pump, Stokes and probe pulses are in accordance with the experimental setup described in section 5.2 (center frequency of 372 THz, intensity FWHM of 5.1 THz).

5.5.1   Pump and probe shaped on PS and PMMA

The molecular phase profile of PS is shown in figure 5.6(a). The opposite phase profile, labeled as the positive profile before, is now referred to as the compensating phase profile. For a single phase step it has been shown in section 4.4 that the optimum frequency of the π-phase step for maximum discrimination in the difference signal is not at the frequency where it compensates the vibrational resonance, due to the interference between resonant and non-resonant CARS contributions. For compensating phase profiles of a fairly empty molecular response this behavior is likely the same. Therefore, the compensating phase profiles and the inverse of these profiles (equal of that of the molecule) are swept through the spectrum. The difference of the calculated CARS signals for these two phase profile sweeps is calculated and compared to the difference between a positive and negative single π-phase step sweep. Figure 5.16 shows the calculated integrated CARS signal on PS for phase profile sweeps. Figures 5.16(a, b) show sweeps with the compensating phase profiles, sweeps with phase profiles equal to the molecular phase and the difference of the two. Figures 5.16(c, d) show sweeps with a positive π-phase step, sweeps with a negative π-phase step and their difference. The width of the applied phase steps is 35 cm^{-1}. Figures 5.16(a, c) show only the resonant contribution and figures 5.16(b, d) show the total CARS signals. The horizontal axes represent the mismatch of the phase profiles applied to the pump and probe pulses with the molecular phase profile for the complete phase profiles. For the π-phase step sweeps the horizontal axes represent the frequency of the phase step. The vertical axes represent the strength of the CARS signals divided by the total CARS signal for a flat phase profile.

Figure 5.16: Calculated integrated CARS signals for phase profile sweeps on PS. a) Phase profile, only resonant CARS signal. b) Phase profile, total CARS signal. c) Single π-phase step, only resonant CARS signal. d) Single π-phase step, total CARS signal.

Several effects can be observed in figure 5.16:

A) the profile sweeps show more features than the single step sweeps. The different features in figure 5.16(a, b) are mainly caused by the major vibrational resonance of PS overlapping with the features in the applied phase profiles.

B) the smaller maxima (bumps) in the compensating phase profile sweep are caused by an overlap of a negative slope of the phase profile with a vibrational band of PS.

C) the maxima in figure 5.16 (a, c) are located at a phase profile mismatch of 0 THz, as expected for the resonant CARS contribution. These maxima are shifted in figure 5.16 (b, d) due to interference with the non-resonant CARS contribution also as expected.

D) the difference signal shows a deeper minimum for the phase profile, the single π-phase step. This larger negative value is caused by the positive slope in the phase profile of PS at 89 THz (figure 5.6(a)), which is located at the center of the main vibrational band of PS for a positive phase profile mismatch of 2.9 THz. This minimum shifts if the non-resonant CARS signal is also taken into account.

E) the enhancement of the CARS signal for the profile is almost the same as for the single π-phase step. The improved compensation by the more complex pump is negated by the more complex phase profile in the probe pulse.

F) for the resonant as well as the total CARS signal the maxima and minima of the difference CARS signals is increased by the use of the phase profiles in comparison with the single π-phase step profiles. The values of the maxima and minima are listed in table 5.3.

	Resonant CARS		Total CARS	
	Profile	π-step	Profile	π-step
Maximum	0.21	0.19	0.34	0.27
Minimum	-0.15	-0.05	-0.41	-0.27

Table 5.3: The maxima and minima of the calculated difference signals for an inverse phase profile sweep or a single π-phase step sweep for PS, with only the resonant CARS and the total CARS. The values are normalized to the total CARS signal for a flat phase profile.

The same calculations are performed on PMMA. The phase profile of PMMA is shown in figure 5.6(b). Figure 5.17 shows the calculated integrated CARS signal for different phase profile sweeps. Figures 5.17(a, b) show sweeps with the compensating phase profiles, sweeps with phase profiles equal to the molecule and the difference of both. Figures 5.17(c, d) show sweeps with a positive π-phase step, sweeps with a negative π-phase step and their difference. The width of the phase steps is 35 cm^{-1} (1.0 THz). Figures 5.17(a, c) show only the resonant contribution and figures 5.17(b, d) show the total CARS signals. The horizontal axes represent the mismatch of the phase profiles applied to the pump and probe pulses with the molecular phase profile for the complete phase profiles. For the π-phase step sweeps the horizontal axes represent the location of the phase step. The vertical axes represent the strength of the CARS signals divided by the total CARS signal for a flat phase profile.

The conclusions and trends of the calculations shown in figure 5.17 are similar to those described below figure 5.16. PMMA has less vibrational bands than PS in the frequency range covered by the applied pump and Stokes pulses. Therefore, the graphs in figure 5.17 have less local maxima and minima than the graphs in figure 5.16.
For the resonant as well as the total CARS signal the maxima and minima of the difference CARS signals are increased by the use of the complete phase profiles in comparison with the single π-phase step profiles. The values of the maxima and minima are listed in table 5.4.
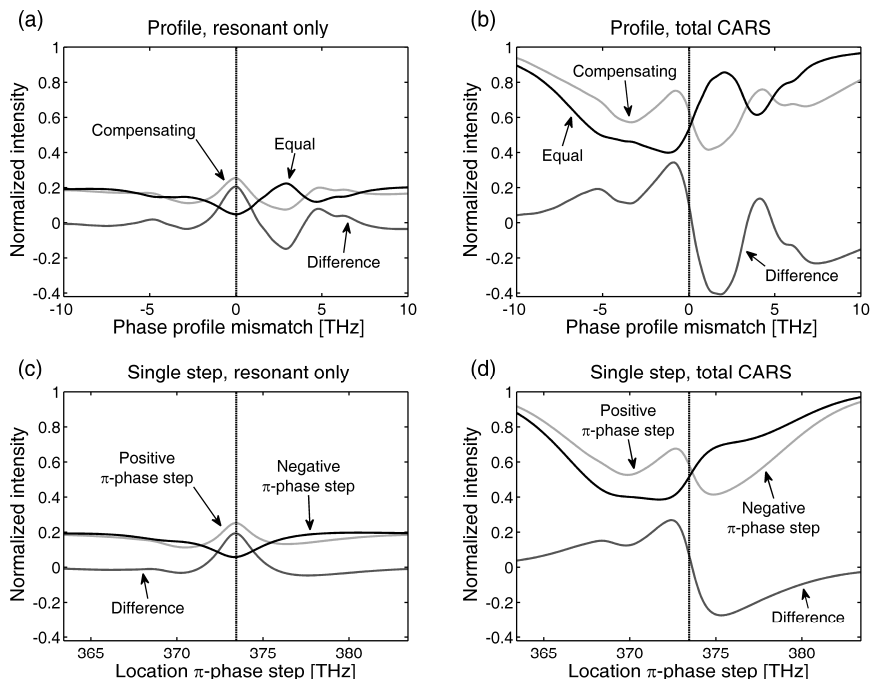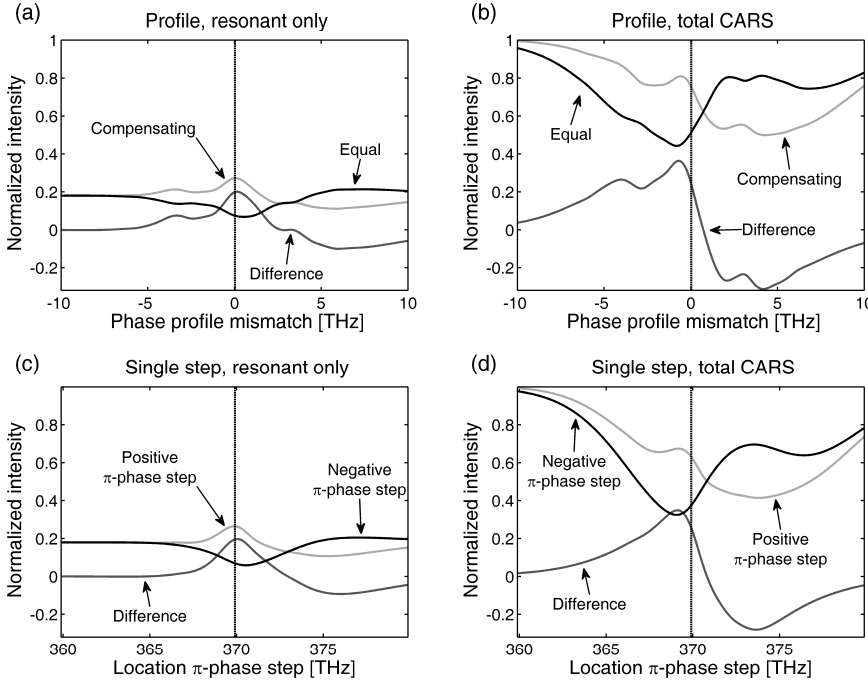
Figure 5.17: Calculated integrated CARS signal for phase profile sweeps on PMMA. a) Phase profile, only resonant CARS signal. b) Phase profile, total CARS signal. c) Single π-phase step, only resonant CARS signal. d) Single π-phase step, total CARS signal.

	Resonant CARS		Total CARS	
	Profile	π-step	Profile	π-step
Maximum	0.20	0.20	0.36	0.35
Minimum	-0.10	-0.09	-0.31	-0.28

Table 5.4: The maxima and minima of the calculated difference signals for an inverse phase profile sweep or a single π-phase step sweep for PMMA, with only the resonant CARS and the total CARS. The values are normalized to the total CARS signal for a flat phase profile.

The maxima and minima of the difference CARS signals for PS and PMMA have a higher absolute value for the phase profiles than for the single π-phase step profiles. The use of phase profiles gives a slight higher contrast ratio in comparison with the background for CARS imaging with PS and PMMA for spectral phase shaping of the pump and probe pulse.

5.5.2 Pump-only shaping on PS and PMMA

In this section calculations are performed where only the pump pulse is shaped. The probe pulse is transform limited. Again PS and PMMA are chosen as molecular sample. The single phase steps are not repeated here because it has already been shown that the phase profile has more effect than a single π-phase step, even if the effect is diminished by the multiple phase steps in the probe pulse. Figure 5.18 shows the calculated integrated CARS signal for phase profile sweeps, with (a) the resonant CARS signal for sweeps with the phase profiles of PS on PS, (b) the total CARS signal for the same sweeps, (c) the resonant CARS signal for sweeps with the complete phase profile for PMMA on PMMA, (d) the total CARS signal for the same sweeps. The horizontal axes represent the mismatch of the phase profiles with the molecular spectrum. The vertical axes represent the strength of the CARS signals divided by the total CARS signal for a flat phase profile.
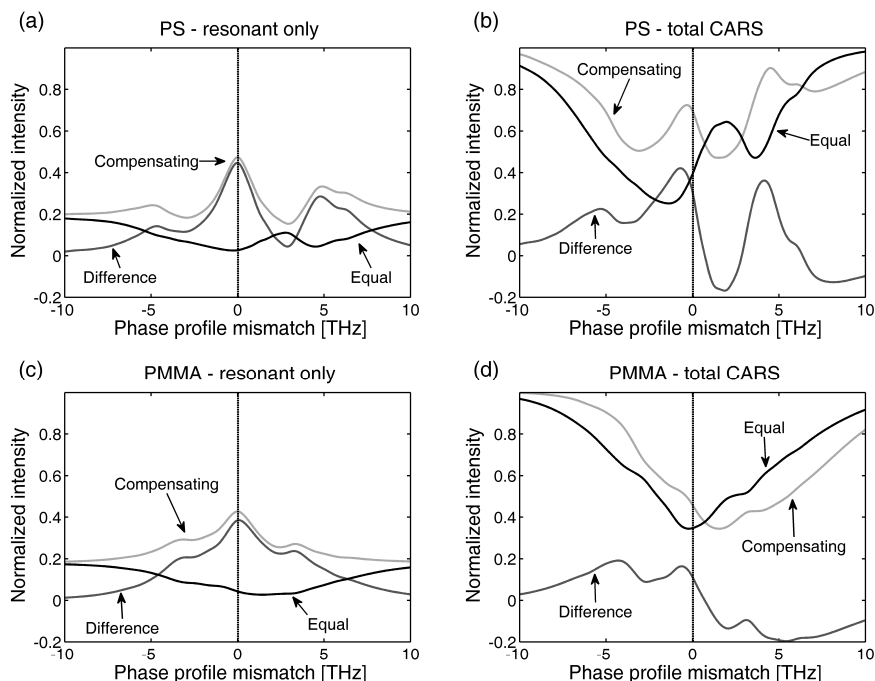
Figure 5.18: Calculated integrated CARS signal for phase profile sweeps, with a transform limited probe. a) For PS only resonant CARS signal. b) For PS total CARS signal. c) For PMMA only resonant CARS signal. d) For PMMA total CARS signal.

The enhancement of the resonant CARS signal for a complete phase profile only applied to the pump pulse is higher than when the probe is also shaped, which is in accordance with the expectations. For the compensating profile with no phase step mismatch the resonant CARS contribution is 0.47 for PS

and 0.43 for PMMA in comparison to the transform limited total CARS signal. For the pump and probe shaped case these values are 0.25 (figure 5.16(a)) and 0.27 (figure 5.17(a)). For pump and probe shaped the CARS signal for PS normalized to the transform limited total CARS signal is lower than the normalized CARS signal for PMMA due to the more complicated concurrent phase profile in the probe pulse. For the resonant CARS contribution the difference CARS signal is positive in the calculated range for PS and PMMA. For other molecules also negative values are possible.

For the total CARS signal the result is similar to the case where the probe is also shaped. For comparison the maximum and minimum values of the difference signal in figure 5.18(b) and 5.18(d) are given. In parentheses the normalized maximum and minimum values of the difference signal is given for the case that both the pump and probe pulses are shaped. The maximum difference value for PS is 0.42 (0.34) and the minimum is -0.17 (-0.41). The maximum difference value for PMMA is 0.19 (0.36) and the minimum is -0.20 (-0.31). As can be seen, the maximum value of PS has increased, while the maximum value for PMMA has decreased. The phase profile for PS is more complicated than that of PMMA; therefore the assumption is made that this method should work for complicated compensating phase profiles for molecules with a high number of vibrational bands in the applied spectrum, this assumption is validated in section 5.5.3.

5.5.3   Virtual molecule

For the virtual molecule a set of 21 vibrational bands is constructed where all the vibrational bands have the same amplitude and width. The maximum value of $\chi_R^{(3)}$ is 2.5 times the value of $\chi_{NR}^{(3)}$ for a single resonance, the width of the resonances is 5 cm^{-1} (0.15 THz). The spacing of the vibrational bands is chosen randomly with the first vibrational resonance at 80.9 THz (2700 cm^{-1}) and the resonances are random spaced with a maximum of 2.10 THz (70 cm^{-1}) between two resonances. An irregular spacing is used to avoid oscillations. Figure 5.19 shows the resonance intensity and phase profile of the virtual molecule. The horizontal axis represents the frequency and the vertical axes represent the intensity or the phase.

Due to the random spacing some vibrational resonances are overlapping, which is the reason that the maxima of the molecular profile in figure 5.19 are of different heights. The frequencies of the vibrational resonances are 80.9, 82.6, 83.4, 83.9, 84.8, 85.0, 85.2, 87.2, 89.2, 90.4, 90.6, 91.0, 91.8, 93.5, 93.5, 93.6, 94.0, 95.4, 96.9, 98.2, and 99.2 THz.
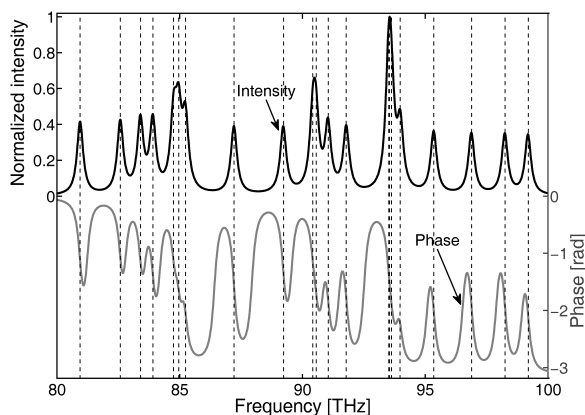
Figure 5.19: Vibrational spectrum and phase of the virtual molecule.

Figure 5.20 shows the calculated integrated CARS signal for the phase profile sweeps. Figures 5.20(a, b) show sweeps with phase profiles in the pump and probe pulses. Figures 5.20(c, d) show sweeps with phase profiles in the pump pulse only. Figures 5.20(a, c) show only the resonant contribution and figures 5.20(b, d) show the total CARS signals. The horizontal axes represent the mismatch of the phase profiles with the molecular phase profile. The vertical axes represent the strength of the CARS signals divided by the total CARS signal for a flat phase profile.

The oscillatory behavior of the results of the phase profile sweeps in figure 5.20 is due to periodic overlap of the phase profile with major vibrational resonances of the virtual molecule, for example the resonances around 93.6 THz (figure 5.19).

Figure 5.20 shows that the assumption is correct that it is useful to shape only the pump pulse, both for the resonant CARS contribution and the total CARS signal. The maximum of the normalized difference signal for the resonant CARS contribution for this particular virtual molecule is 0.57 for pump and probe shaped; for only probe shaped the maximum of the normalized difference signal is 1.32, which is significant higher. The maximum of the normalized total CARS signal is 0.61 for pump and probe shaped; for only probe shaped the maximum of the normalized difference signal is 1.35, which is also significantly higher. With this simulation the assumption that it is useful to use the complete molecular phase profiles for shaping in case of a dense molecular phase profile has been validated. The calculated results, on the relative simple molecular phase profiles such as PMMA, show that it is not useful to apply pump only shaping for molecular systems with relatively simple molecular phase profiles.

125
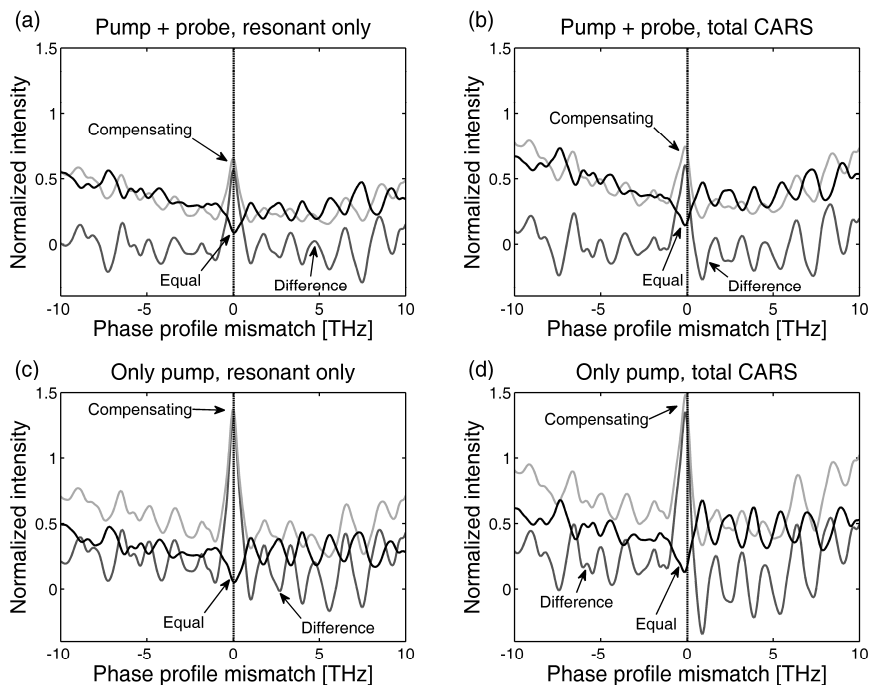
Figure 5.20: Calculated integrated CARS signal for complete phase profile sweeps on a virtual molecule. a) Pump and probe shaped, only resonant CARS signal. b) Pump and probe shaped, total CARS signal. c) Pump only shaped, only resonant CARS signal. d) Pump only shaped, total CARS signal.

5.6 Summary and recommendations

In this chapter a proof of principle has been presented for chemical selective imaging based on relatively simple phase profiles in broadband pump and probe pulses. This chemical selective imaging does not require a measurement of the CARS spectrum at each pixel; it is based on integrated CARS signals only. As demonstration of this method PS and PMMA beads on a glass substrate are imaged. The choice of an independent Stokes pulse source gives the possibility to extend this method to other vibrational energy regions. This method is promising for imaging with chemical contrast without the need to tune the laser while imaging. Furthermore it works on integrated CARS signals, which can 'easily' be measured with a PMT or photon counting device. The calculations, in section 5.5, show that the use of phase profiles which incorporate the complete molecular phase profile is useful for molecular systems with multiple lines in the applied spectrum. Here pump only shaping improves the response but complicates the

excitation. For simple molecular systems such as PMMA it is not useful, as the contrast there is slightly better with a simple π-phase step.

Summary

In this thesis, spectral phase shaping of broadband pulses is described for application in non-linear spectroscopy and imaging. The thesis starts with a description of a spectral phase shaper that was designed, built, calibrated and tested. The latter includes a series of experiments exploring two-photon fluorescence with a spectral phase shaped laser. The central application is Coherent Anti-Stokes Raman Scattering (CARS) spectroscopy, where the pump and probe pulses of the CARS process are spectrally phase shaped. The knowledge acquired in the CARS spectroscopy experiments is further applied to chemically selective imaging.

Chapter two begins by discussing the design of a spectral phase shaper setup, according to the design considerations given by the long-term goal of performing CARS spectroscopy and microscopy in the fingerprint region of proteins (330 – 1500 cm^{-1}). The shaper setup is based on a grating and a cylindrical mirror to map frequencies to different pixels of a liquid crystal device. The calibration of the liquid crystal device is demonstrated and evaluated. Three approaches are presented. Of these three methods, peak shaping in the second harmonic spectrum and dip shaping in the fundamental spectrum are shown to be superior. To measure the generated phase shaped pulses, a second-order intensity autocorrelator was built as well as an AJOLOTE, which is a frequency resolved optical gating type of device. The design of the AJOLOTE has a spectral resolution with a FWHM spread of 1.9 nm in the center of the pulse.

In chapter three, it is demonstrated that the sign of the spectral phase in the second harmonic field is of importance for the two-photon fluorescence yield in resonant transitions. This is shown for fluorescent protein, fluorescent dye (cascade blue), and quantum dot samples. For the cascade blue dye and the quantum dots, spectral phase profiles applied to the laser pulse show an enhancement of the two-photon fluorescence that exceeds the response for a transform-limited pulse. The dye cascade blue and the quantum dot have no

intermediate resonances, which suggest that the two-photon fluorescence can be enhanced even for systems without intermediate resonances. A non-resonant transition shows no such increase, and is insensitive to the sign of a phase step. Some questions remain on the precise definition of the phase profiles defined those experiments. No explanation is put forward for this effect.

In chapter four, a new spectral phase shaping strategy is demonstrated for CARS spectroscopy. Vibrational transitions can be identified with a resolution limited by the resolution of the spectral phase shaper (0.5 cm^{-1}). Furthermore, a method is introduced for measuring the line width of isolated spectral lines, and an effective line width for a combination of lines. Relative cross-sections can be extracted from spectral data. It is demonstrated that it is possible to remove the non-resonant contribution for materials that have no resonances in the frequency range covered by the energy difference of the pump and Stokes pulses.

In chapter five, chemically selective CARS imaging based on relatively simple phase profiles. The technique obviates the need for measuring a CARS spectrum at each pixel, because it is based on integrated CARS signals, which can 'easily' be measured on a photo- multiplier tube or a photon counting device. A sample consisting of polystyrene and polymethylmethacrylate beads on a glass substrate is imaged with these relatively simple phase profiles, showing a clear difference between the different types of beads depending on the chosen phase profiles. The choice of an independent Stokes pulse source makes it possible to extend the method to other vibrational energy regions. Furthermore theoretical insight is given for using more complex phase profiles incorporating the complete molecular structure.

Samenvatting

In dit proefschrift is het gebruik van spectrale fasevervorming van breedbandige pulsen beschreven in de toepassing van niet lineaire spectroscopie en het visualiseren van monsters met chemisch contrast. Het proefschrift begint met de beschrijving van een vervormer die de fase van het licht controleert in het spectrale domein. Het ontwerp, de bouw, de ijking en het testen van deze spectrale fase vervormer is beschreven. Het laatstgenoemde omvat tevens een serie twee-foton-fluorescentie experimenten met verschillende vormen van de spectrale fase van een breedbandige laser bron. De centrale toepassing is Coherente anti-Stokes Raman verstrooiing (CARS) spectroscopie, waarbij de pomp en meetpulsen van het CARS proces identieke spectrale fasevervormde laserpulsen zijn. De kennis die verworven is met de CARS spectroscopie-experimenten is verder toegepast voor het visualiseren van monsters met chemisch contrast.

Hoofdstuk twee begint met het bespreken van het ontwerp van de spectrale fase vervormer, volgens ontwerp overwegingen die zijn ingegeven door het lange termijn doel. Dat doel is het uitvoeren van CARS spectroscopie en microscopie in het spectrale "vingerafdruk"-gebied van eiwitten (330 – 1500 cm^{-1}). De spectrale fase vervormer is gebaseerd op een tralie en een cilindrische spiegel die de verschillende frequenties van breedbandige laser pulsen afbeelden op verschillende pixels van een apparaat gevuld met vloeibare kristallen. De ijking van het apparaat met de vloeibare kristallen wordt gedemonstreerd en geëvalueerd. Drie benaderingen worden voorgesteld. Van deze drie benaderingen zijn de creatie van een piek in het tweede harmonische spectrum en het spectrale amplitude vervorming in het fundamentele spectrum superieur. Om de gegenereerde fase vervormde pulsen te meten, wordt een tweedeorde intensiteitsautocorrelator en een AJOLOTE gebouwd. De AJOLOTE is een soort frequentie opgeloste optische poort apparaat. Het ontwerp van de AJOLOTE heeft een spectrale

resolutie van 1,9 nm (volledige breedte op halve hoogte) voor de middelste golflengte van de laserpulsen.

In hoofdstuk drie wordt gedemonstreerd dat het teken van de spectrale fase van het tweede harmonische veld van belang is voor de twee-foton-fluorescentie efficiency voor overgangen met resonanties. Dit is aangetoond voor een fluorescerend eiwit, fluorescerend kleurstof (cascade blue) en kwantumpunten. Voor de kleurstof en de kwantumpunten zijn spectrale fase vervormde pulsen toegepast op de laserpulsen die een twee-foton-fluorescentie efficiëntie vertonen die meer is dan de efficiëntie voor een Fourier gelimiteerde laserpuls. De kleurstof cascade blue en de kwantumpunten hebben geen tussenliggende resonanties, de suggestie is dan ook dat de twee-foton-fluorescentie efficiëntie kan worden verbeterd ten opzichte van Fourier gelimiteerde laserpuls zelfs voor systemen zonder tussenliggende resonanties. Een overgang zonder resonanties toont geen verhoging van de efficiëntie boven de Fourier gelimiteerde laserpulsen en is ook ongevoelig voor het teken van de fasestap. Sommige vragen blijven over naar aanleiding van de nauwkeurigheid van de faseprofielen die gebruikt zijn in deze experimenten. Geen verklaring is gegeven voor het beschreven effect.

In hoofdstuk vier is een nieuwe spectrale fase vervorming strategie gedemonstreerd voor CARS spectroscopie. Vibratieovergangen kunnen worden geïdentificeerd met een resolutie die beperkt wordt door de resolutie van de spectrale fase vervormer ($0,5$ cm^{-1}). Verder wordt een methode voor het meten van de lijnbreedte van geïsoleerde vibraties en een effectieve lijnbreedte voor een combinatie van lijnen voorgesteld. Relatieve dwarsdoorsneden van de lijnen kunnen uit de spectrale vervormde metingen geëxtraheerd worden. Hier wordt aangetoond dat het mogelijk is de niet-resonantie bijdrage voor materialen te verwijderen die geen resonanties in het toegepaste frequentiebereik hebben.

In hoofdstuk vijf zijn CARS visualisaties gemaakt van monsters, waar chemisch contrast is gebaseerd op betrekkelijk eenvoudige faseprofielen. De techniek ondervangt de noodzaak van het meten van een CARS spectrum op elk beeldpunt omdat het op geïntegreerde CARS signalen is gebaseerd, die "gemakkelijk" gemeten kunnen worden met een foton-vermenigvuldigerbuis of een apparaat dat fotonen telt. Een monster dat uit polystyreen en polymethylmethacrylate bollen op een glasondergrond bestaat is met deze betrekkelijk eenvoudige faseprofielen weergegeven en een helder verschil is aangetoond tussen de verschillende soorten bollen die afhangen van de gekozen faseprofielen. De keuze van onafhankelijke Stokes pulsen maakt het mogelijk om deze methode te gebruiken in een ander vibratie-energiegebied. Verder wordt er theoretisch inzicht gegeven voor het gebruik van faseprofielen die gebruik maken van de volledige moleculaire structuur.

Dankwoord

Voor jullie ligt nu een proefschrift waarin samengevat is wat ik de afgelopen vier jaar gedaan heb op wetenschappelijk terrein. Zonder hulp en steun van anderen was dit proefschrift nooit tot stand gekomen. Daarom wil ik alle mensen bedanken die mij hebben bijgestaan. Ik kan niet iedereen die op enigerlei wijze invloed heeft uitgeoefend op dit proefschrift afzonderlijk bedanken, maar ik wil er graag een paar uitlichten.

Allereerst mijn promotor Jennifer. Het laatste jaar heeft ze veel positieve invloed gehad op de promotie. Als een relatieve buitenstaander had ze zeer verfrissende ideeën.

Ten tweede mijn dagelijks begeleider Herman. Recht door zee, komt vaak met nieuwe ideeën en zijn precisie in de feedback bij het schrijven van het proefschrift heeft een belangrijke bijdrage geleverd om tot dit resultaat te komen.

Ten derde Niek van Hulst die me de mogelijkheid heeft gegeven om bij FOM en zijn vakgroep te promoveren. Met name in het begin hebben zijn steun en inzichten geholpen bij het project.

De technische ondersteuning van Frans en Jeroen heeft ervoor gezorgd dat het mogelijk bleef om met de opstelling te blijven werken en zonder hun kennis en praktische hulp was het niet zover gekomen.

Ward, Martin, Hinke en Alexander, het was erg leuk en leerzaam om met jullie samen te werken en te begeleiden. De verbreding die kwam door discussies en resultaten van de projecten die jullie uitvoerden verdiepten allerlei inzichten.

En natuurlijk de vakgroepgenoten van Optische Technieken / Optical Sciences, het zijn er teveel om op te noemen. Sommigen wil ik speciaal bedanken. Peter, bedankt voor de snelle start, helemaal terug in 2004 en voor de inhoudelijke discussies. Robert, bedankt voor je hulp met de meer geavanceerde computerprobleempjes en de vele al dan niet inhoudelijke gesprekken tijdens het fitnessen. Karen, bedankt voor het uit handen nemen

van allerlei organisatorische en bureaucratische taken, ik had er amper meer omkijken naar.

Verder bedank ik al mijn vrienden voor de steun en getoonde interesse voor mijn werk. Het sporten bij de Stretchers en de aansluitende derde ronde heeft er zeker toe bijgedragen dat ik niet continu met het proefschrift bezig was en ook eens mijn gedachten op iets anders kon richten, evenals de avondjes bridgen.

Mijn paranimfen, Rob en Wouter, jullie heel erg bedankt voor het uit handen nemen van organisatorische zaken rond de promotie en de steun en het vertrouwen die ik van jullie heb mogen ontvangen tijdens de toch niet altijd even gemakkelijke promotieperiode.

Tot slot wil ik graag mijn naaste familieleden bedanken voor hun eindeloze steun en vertrouwen tijdens de afgelopen vier jaar.

Sytse Postma
Augustus 2008

Publications and conferences

Papers

- S. Postma, A. C. W. van Rhijn, H. L. Offerhaus, and J. L. Herek, *"Chemical selective imaging using spectral phase shaped CARS"*, in preparation
- S. Postma, A. C. W. van Rhijn, H. L. Offerhaus, and J. L. Herek, *"Femtosecond spectral phase shaping for CARS spectroscopy and imaging"*, in Ultrafast Phenomena XVI, Springer Series in Chemical Physics, accepted for publication
- S. Postma, A. C. W. van Rhijn, J. P. Korterik, P. Gross, J. L. Herek, and H. L. Offerhaus, *"Application of spectral phase shaping to high resolution CARS spectroscopy"*, Optics Express **16**, 7985, 2008
- S. Postma, H. L. Offerhaus, V. Subramaniam, and N. F. van Hulst, *"Coherent control of two-photon fluorescence with a high-resolution spectral phase shaper"*, in Ultrafast Phenomena XV, Springer Series in Chemical Physics **88**, 208, 2007
- S. Postma, P. van der Walle, H. L. Offerhaus, and N. F. van Hulst, "*Compact high-resolution spectral phase shaper"*, Review of Scientific Instruments **76**, 123105, 2005

International conference contributions

- <u>S. Postma</u>, M. Jurna, A. C. W. van Rhijn, J. P. Korterik, J. L. Herek, and H. L. Offerhaus, *"Femtosecond spectral phase shaping for CARS spectroscopy and imaging"*, XVI International Conference on Ultrafast Phenomena, Stresa, Italy, poster contribution, 2008
- S. Postma, A. C. W. van Rhijn, J. P. Korterik, J. L. Herek, and <u>H. L. Offerhaus</u>, *"CARS spectroscopy and microscopy around 3000 cm^{-1} using spectral phase shaping of pump and probe pulses"*, microCARS conference, Igls, Austria, oral contribution, 2008

- S. Postma, A. C. W. van Rhijn, J. P. Korterik, J. L. Herek, and <u>H. L. Offerhaus</u>, *"Spectral Phase Shaping for High Resolution CARS Spectroscopy around 3000 cm^{-1}"*, Conference on Lasers and Electro-Optics (CLEO), San Jose, USA, oral contribution, 2008

- <u>S. Postma</u>, A. C. W. van Rhijn, J. P. Korterik, H. L. Offerhaus, and J. L. Herek, *"Spectral phase shaping for CARS spectroscopy and microscopy"*, EOS Topical Meeting on Photonic Devices, Utrecht, the Netherlands, oral contribution, 2008

- S. Postma, A. C. W. van Rhijn, J. P. Korterik, J. L. Herek, and <u>H. L. Offerhaus</u>, *"CARS spectroscopy around 3000 cm^{-1} using spectral phase shaping of pump and probe pulses"*, NMOC 2008, Münster, Germany, oral contribution, 2008

- <u>S. Postma</u>, H. L. Offerhaus, V. Subramaniam, and N. F. van Hulst, *"Coherent control of two-photon fluorescence with a high-resolution spectral phase shaper"*, XV International Conference on Ultrafast Phenomena, Pacific Grove, USA, Poster contribution, 2006

National conferences contributions

- <u>S. Postma</u>, M. Jurna, J. L. Herek, and H. L. Offerhaus, *"CARS spectroscopy and microscopy"*, Fotonica Evenement 2008, Nieuwegein, the Netherlands, oral contribution, 2008

- <u>S. Postma</u>, A. C. W. van Rhijn, J. P. Korterik, H. L. Offerhaus, and J. L. Herek, *"CARS spectroscopy with rejection of non-resonant background by spectral phase shaping"*, NWO CW Spectroscopie en Theorie, Lunteren, the Netherlands, oral contribution, 2008

- <u>S. Postma</u>, H. L. Offerhaus, and J. L. Herek, *"Improving CARS signal and selectivity by spectral phase shaping"*, Physics@FOM Veldhoven 2008, Veldhoven, the Netherlands, oral contribution, 2008

- <u>S. Postma</u>, J. P. Korterik, and H. L. Offerhaus, *"Timing stabilization of two mode locked lasers"*, 31st Meeting of the section Atomic Molecular and Optical Physics, Lunteren, the Netherlands, poster contribution, 2007

- <u>S. Postma</u> and H. L. Offerhaus, *"Compact high-resolution spectral phase shaper"*, 30th Fall meeting of the section Atomic Molecular and Optical Physics, Lunteren, the Netherlands, poster contribution, 2005

- <u>S. Postma</u>, P. van der Walle, W. van der Vecht, H. L. Offerhaus, and N. F. van Hulst, *"A compact femtosecond pulse shaper for dedicated pump-probe experiments"*, 29th Fall meeting of the section Atomic Molecular and Optical Physics, Lunteren, the Netherlands, poster contribution, 2004

References

[1]   C. V. Raman and K. S. Krishnan, *A New Type of Secondary Radiation*, Nature **121**, 501 (1928)

[2]   P. D. Maker and R. W. Terhune, *Study of Optical Effects Due to an Induced Polarization Third Order in the Electric Field Strength*, Phys. Rev. **137**, A801 (1965)

[3]   J. Cheng, A. Volkmer, and X. S. Xie, *Theoretical and experimental characterization of coherent anti-Stokes Raman scattering microscopy*, J. Opt. Soc. Am. B **19**, 1363 (2002)

[4]   M. Hashimoto, T. Araki, and S. Kawata, *Molecular vibration imaging in the fingerprint region by use of coherent anti-Stokes Raman scattering microscopy with a collinear configuration*, Opt. Lett. **25**, 1768 (2000)

[5]   J. Konradi, A. K. Singh, A. V. Scaria, and A. Materny, *Selective spectral filtering of molecular modes of β-carotene in solution using optimal control in four-wave-mixing spectroscopy*, J. Raman Spectrosc. **37**, 697 (2006)

[6]   J. Konradi, A. V. Scaria, V. Namboodiri, and A. Materny, *Application of feedback-controlled pulse shaping for control of CARS spectra: The role of phase and amplitude modulation*, J. Raman Spectrosc. **38**, 1006 (2007)

[7]   N. Dudovich, D. Oron, and Y. Silberberg, *Single-pulse coherently controlled nonlinear Raman spectroscopy and microscopy*, Nature, **418**, 512 (2002)

[8]   D. Oron, N. Dudovich, and Y. Silberberg, *Femtosecond Phase-and-Polarization Control for Background-Free Coherent Anti-Stokes Raman Spectroscopy*, Phys. Rev. Lett. **90**, 213902 (2003)

[9]   T. Polack, D. Oron, and Y. Silberberg, *Control and measurement of a non-resonant Raman wavepacket using a single ultrashort pulse*, Chem. Pys. **318**, 163 (2005)

[10]   A. M. Weiner, D. E. Leaird, G. P. Wiederrecht, and K. A. Nelson, *Femtosecond multiple-pulse impulsive stimulated Raman scattering spectroscopy*, J. Opt. Soc. Am. B **8**, 1264 (1991)

[11]   S. Lim. A. G. Caster, and S. R. Leone, *Single-pulse phase-control interferometric coherent anti-Stokes Raman scattering spectroscopy*, Phys. Rev A **72**, 0418303 (2005)

[12]   A. M. Weiner, *Femtosecond pulse shaping using spatial light modulators*, Rev. Sci. Instrum. **71**, 1929 (2000)

[13]   J. Savolainen, *Coherent control of biomolecules*, Ph.D. thesis, University of Twente, ISBN: 978-9036526715 (2008)

[14]   Y. Ding, R. M. Brubaker, D. D. Nolte, M. R. Melloch, and A. M. Weiner, *Femtosecond pulse shaping by dynamic holograms in photorefractive multiple quantum wells*, Opt. Lett. **22**, 718 (1997)

[15]   M. Haner and W. S. Warren, *Synthesis of crafted optical pulses by time domain modulation in a fiber-grating compressor*, Appl. Phys. Lett. **52**, 1458 (1988)

[16]   C. W. Hillegas, J. X. Tull, D. Goswami, D. Strickland, and W. S. Warren, *Femtosecond laser pulse shaping by use of a microsecond radio-frequency pulses*, Opt. Lett. **19**, 737 (1994)

[17]   H. Wang, Z. Zheng, D. E. Leaird, A. M. Weiner, T. A. Dorschner, J. J. Fijol, L. J. Friedman, H. Q. Nguyen, and L. A. Palmaccio, *20-fs pulse shaping with a 512-element phase-only liquid crystal modulator*, IEEE J. Quantum Electron. **7**, 718 (2001)

[18]   A. Präkelt, M. Wollenhaupt, A. Assion, Ch. Horn, C. Sarpe-Tudoran, M. Winter, and C. Baumert, *Compact, robust, and flexible setup for femtosecond pulse shaping*, Rev. Sci. Instrum. **74**, 4950 (2003)

[19]   G. Stobrawa1, M. Hacker, T. Feurer, D. Zeidler, M. Motzkus, and F. Reichel, *A new high-resolution femtosecond pulse shaper*, Appl. Phys. B **72**, 627 (2001)

[20]   T. Binhammer, E. Rittweger, R. Ell, and F. X. Kärtner, *Prism-Based Pulse Shaper for Octave Spanning Spectra*, IEEE J. Quantum Electron. **41**, 1552 (2005)

[21]   A. Präkelt, M. Wollenhaupt, A. Assion, Ch. Horn, C. Sarpe-Tudoran, M. Winter, and T. Baumert, *Compact, robust, and flexible setup for femtosecond pulse shaping*, Rev. Scien. Instrum. **74**, 4950 (2003)

[22]   A. F. Hill, M. Desbruslais, S. Joiner, K. C. L. Sidle, I. Gowland, and J. Collinge, *The same prion strain causes vCJD and BSE*, Nature **389**, 450 (1997)

[23]   J. M. Bakker, L. M. Aleese, G. Meijer, and G. von Helden, *Fingerprint IR Spectroscopy to Probe Amino Acid Conformations in the Gas Phase*, Phys. Rev. Lett. **91**, 203003 (2003)

[24]   E. M. Garmire and A. Yariv, *Laser Mode-Locking with Saturable Absorbers*, IEEE J. Quantum Electron. **3**, 222 (1967)

[25]   W. Denk, J. H. Strickler, and W. W. Webb, *Two-Photon Laser Scanning Fluorescence Microscopy*, Science **248**, 73 (1990)

[26]   I. Pastirk, J. M. Dela Cruz, K. A. Walowicz, V. V. Lozovoy, and M. Dantus, *Selective two-photon microscopy with shaped femtosecond pulses*, Opt. Express, **11**, 1695, (2003)

[27]   N. Dudovich, B. Dayan, S. M. G. Faeder, and Y. Silberberg, *Transform-Limited Pulses Are Not Optimal for Resonant Multiphoton Transitions*, Phys. Rev. Lett. **86**, 47 (2001)

[28]   A. Zumbusch, G. R. Holtom, and X. S. Xie, *Three-Dimensional Vibrational Imaging by Coherent Anti-Stokes Raman Scattering*, Phys. Rev. Lett. **82**, 4142 (1999)

[29]   M. D. Duncan, J. Reintjes, and T. J. Manuccia, *Scanning coherent anti-Stokes Raman microscope*, Opt. Lett. **7**, 350 (1982)

[30]   E. O. Potma, C. L. Evans, and X. S. Xie, *Heterodyne coherent anti-Stokes Raman scattering (CARS) imaging*, Opt. Lett. **31**, 241 (2006)

[31]   M. Müller and J. M. Schins, *Imaging the Thermodynamic State of Lipid Membranes with Multiplex CARS Microscopy*, J. Phys. Chem B. **106**, 3715 (2002)

[32]   B. von Vacano, L. Meyer, and M. Motzkus, *Rapid Polymer blend imaging with quantitative broadband multiplex CARS microscopy*, J. Raman Spectrosc. **38**, 916 (2007)

[33]   T. W. Kee and M. T. Cicerone, *Simple approach to one-laser, broadband coherent anti-Stokes Raman scattering microscopy*, Opt. Lett. **29**, 2701 (2004)

[34]   S. Zhang, L. Zhang, X. Zhang, L. Ding, G. Chen, Z. Sun, and Z. Wang, *Selective excitation of CARS by adaptive pulse shaping based on genetic algorithm*, Chem. Phys. Lett. **433**, 416 (2007)

[35]   J. R. Baena and B. Lendl, *Raman spectroscopy in chemical bioanalysis*, Chem. Bio. **8**, 534 (2004)

[36]   R. D. Schaller, J. Ziegelbauer, L. F. Lee, L. H. Haber, and R. J. Saykally, *Chemically Selective Imaging of Subcellular Structure in Human Hepatocytes with Coherent Anti-Stokes Raman Scattering (CARS) Near-Field Scanning Optical Microscopy (NSOM)*, J. Phys. Chem. B **106**, 8489 (2002)

[37]   J. Squier and M. Müller, *High resolution nonlinear microscopy: A review of sources and methods for achieving optimal imaging*, Rev. Scien. Instrum. **72**, 2855 (2001)

[38]   Y. Fu, H. Wang, R. Shi, and J. Cheng, *Characterization of photodamage in coherent anti-Stokes Raman scattering microscopy*, Opt. Express **14**, 3942 (2006)

[39]   J. Cheng and X. S. Xie, *Coherent Anti-Stokes Raman Scattering Microscopy: Instrumentation, Theory, and Applications*, J. Phys. Chem. B **108**, 827 (2004)

[40]   J. L. Herek, W. Wohlleben, R. J. Cogdell, D. Zeidler, and M. Motzkus, *Quantum control of energy flow in light harvesting*, Nature **417**, 533 (2002)

[41]   M. Dantus and V. V. Lozovoy, *Experimental Coherent Laser Control of Physicochemical Processes*, Chem. Rev. **104**, 1813 (2004)

[42]   F. Vetter, M. Plewicki, A. Lindinger, A. Merli, S. M. Weber, and L. Woste, *Optimized isotope-selective ionization of $^{23}Na^{39}K$ and $^{23}Na^{41}K$ by applying evolutionary strategies,* Phys. Chem. Chem. Phys. **7**, 1151 (2005)

[43]   P. F. Tian, D. Keusters, Y. Suzaki, and W. S. Warren, *Femtosecond Phase-Coherent Two-Dimensional Spectroscopy*, Science **300**, 1553 (2003)

[44]   E. M. H. P. van Dijk, J. Hernando, J. J. Garcia-Lopez, M. Crego-Calama, D. N. Reinhoudt, L. Kuipers, M. F. Garcia-Parajo, and N. F. van Hulst, *Single-Molecule Pump-Probe Detection Resolves Ultrafast Pathways in Individual and Coupled Quantum Systems*, Phys. Rev. Lett. **94**, 078302 (2005)

[45]   D. Meshulach and Y. Silberberg, *Coherent quantum control of two-photon transitions by a femtosecond laser pulse*, Nature 396, 239 (1998)

[46]   T. Brixner, N. H. Damrauer, P. Niklaus, and G. Gerber, *Photoselective adaptive femtosecond quatum control in the liquid phase*, Nature **414**, 57 (2001)

[47]   H. Rabitz, R. de Vivie-Riedle, M. Motzkus, and K. Kompa, *Whither the Future of Controlling Quatum Phenomena?*, Science **288**, 824 (2000)

[48]   Y. Silberberg, *Quantum control with a twist*, Nature **430**, 624 (2004)

[49]   D. Goswami, *Optical pulse shaping approaches to coherent control*, Phys. Rep. **374**, 385 (2003)

[50]   E. Hecht, *Optics*, 4^{ed} edition (Pearson Education, Inc., ISBN: 978-0805385663, 2002)

[51]   G. Ghosh, *Sellmeier coefficients and dispersion of thermo-optic coefficients for some optical glasses*, Appl. Opt. **36**, 1540 (1997)

[52]   H. Kogelnik and T. Li, *Laser Beams and Resonators*, Appl. Opt. **5**, 1550 (1966)

[53]   B. E. A. Saleh and M. C. Teich, *Fundamentals of photonics* (John Wiley & Sons, Inc., ISBN: 978-0471839651, 1991)

[54]   P. Baum, S. Lochbrunner, L. Gallmann, G. Steinmeyer, U. Keller, and E. Riedle, *Real-time characterization and optimal phase control of tunable visible pulses with a flexible compressor*, Appl. Phys. B 74, S219 (2002)

[55]   http://www.schott.com/optics_devices/german/download/... opticalglassdatasheetsv101007.xls (2008)

[56]   K. P. Birch and M. J. Downs, *An Updated Edlen Equation for the Refractive Index of Air*, Metrologia **30**, 155 (1993)

[57]   F. A. Jenkins and H. E. White, *Fundamentals of Optics*, 4^{ed} edition (McGraw-Hill Book Co., ISBN: 978-0072561913, 1981)

[58]   P. G. De Gennes, *The Physics of Liquid Crystals*, (Clarendon, ISBN: 978-0198517856, 1974)

[59]   J. Stockley and S. Serati, *Advances in liquid crystal based devices for wavefront control and beamsteering*, Proc. SPIE **5894**, 58940K-1 (2005)

[60]   J. J. Field, T. A. Planchon, W. Amir, C. G. Durfee, and J. A. Squier, *Characterization of a high efficiency, ultrashort pulse shaper incorporating a reflective 4096-element spatial light modulator*, Opt. Commun. **278**, 368 (2007)

[61]   J. Stockley and S. Serati, *Advances in liquid crystal beam steering*, Proc. SPIE **5550**, 32 (2004)

[62]   D. J. Griffiths, *Introduction to electrodynamics*, 2th edition, (Prentice-Hall Inc., ISBN: 978-0138053260, 1989)

[63]   M. Born and E. Wolf, *Principles of Optics*, 7th edition (Cambridge University Press, ISBN: 978-0521642224, 2001)

[64]   A. Savitzky and M. J. E. Golay, *Smoothing and Differentiation of Data by Simplified Least Squares Procedures*, Anal. Chem. **36**, 1627 (1964)

[65]   S. WU, *Birefringence dispersions of liquid crystals*, Phys. Rev. A **33**, 1270 (1986)

[66]   T. Tanabe, K. Ohno, T. Okamoto, M. Yamanaka, and F. Kannari, *Feedback Control for Accurate Shaping of Ultrashort Optical Pulses prior to Chirped Pulse Amplification*, Jap. J. Appl. Phys. **43**, 1366 (2004)

[67]   H. Karlsson, *Fabrication of periodically poled crystals from the KTP family and their application in nonlinear optics*, Ph.D. thesis, Universität Hannover, Germany (ISBN: 9930287507, 1999)

[68]   M. Ghotbi and M. Ebrahim-Zadeh, *Optical second harmonic generation properties of BiB_3O_6*, Opt. Express **12**, 6002 (2004)

[69]   Z. Wang, B. Teng, K. Fu, X. Xu, R. Song, C. Du, H. Jiang, J. Wang, Y. Liu, and Z. Shao, *Efficient second harmonic generation of pulsed laser radiation in BiB_3O_6 (BIBO) crystal with different phase matching directions*, Opt. Commun. **202**, 217 (2002)

[70]   H. Hellwig, J. Liebertz, and L. Bohatý, *Linear optical properties of the monoclinic bismuth borate BiB_3O_6*, J. Appl. Phys. **88**, 240 (2000)

[71]   K. A. Walowicz, I. Pastirk, V. V. Lozovoy, and M. Dantus, *Multiphoton Intrapulse Interference. 1. Control of Multiphoton Processes in Condensed Phases*, J. Phys. Chem. A **106**, 9370 (2002)

[72]   T. Baumert, T. Brixner, V. Seyfried, M. Strehle, and G. Gerber, *Femtosecond pulse shaping by an evolutionary algorithm with feedback*, Appl. Phys. B **65**, 779 (1997)

[73]   J. K. Ranka, A. L. Gaeta, A. Baltuska, M. S. Pshenichnikov, and D. A. Wiersma, *Autocorrelation measurement of 6-fs pulses based on the two-photon-induced photocurrent in a GaAsP photodiode*, Opt. Lett. **22**, 1344 (1997)

[74]   A. M. Weiner, *Effect of Group Velocity Mismatch on the Measurement of Ultrashort Optical Pulses via Second Harmonic Generation*, IEEE J. Quantum Electron. **19**, 1276 (1983)

[75]   J. M. Diels, J. J. Fontaine, I. C. McMichael, and F. Simoni, *Control and measurement of ultrashort pulse shapes (in amplitude and phase) with femtosecond accuracy*, Appl. Opt. **24**, 1270 (1985)

[76]   W. H. Press, S. A. Teukolskym W. T. Vetterling, and B. P. Flannery, *Numerical Recipes in C++*, 2th edition, (Cambridge University Press, ISBN: 978-0521880688, 2003)

[77]   R. Trebino, K. W. DeLong, D. N. Fittinghoff, J. N. Sweetser, M. A. Krumbügel, B. A. Richman, and D. J. Kane, *Measuring ultrashort laser pulses in the time-frequency domain using frequency-resolved optical gating*, Rev. Sci. Instrum. **68**, 3277 (1997)

[78]   R. Trebino, *Frequency-Resolved Optical Gating: The Measurement of Ultrashort Laser Pulses* (Kluwer Academic Publishers, ISBN: 978-1402070662, 2000)

[79]   P. O'Shea, M. Kimmel, X. Gu, and R. Trebino, *Highly simplified device for ultrashort-pulse measurement*, Opt. Lett. **26**, 932 (2001)

[80]   P. O'Shea, M. Kimmel, and R. Trebino, *Increased phase-matching bandwidth in simple ultrashort-laser-pulse measurements*, J. Opt. B: Quantum Semiclass. Opt. **4**, 44 (2002)

[81]   D. N. Nikogosyan, *Nonlinear Optical Crystals: A Complete Survey* (Springer-Verlag, ISBN: 978-0387220222, 2005)

[82]   H. Hellwig, J. Liebertz, and L. Bohatý, *Exceptional large nonlinear optical coefficients in the monoclinic bismuth borate BiB_3O_6 (BIBO)*, Solid State Commun. **109**, 249 (1999)

[83]   K. Kato, *Second-Harmonic Generation to 2048 Å in β-BaB_2O_4*, IEEE J. Quantum Electron. **22**, 1013 (1986)

[84]   C. Chen, Y. Wu, A. Jiang, B. Wu, G. You, R. Li, and S. Lin, *New nonlinear-optical crystal: LiB_3O_5*, J. Opt. Soc. Am. B **6**, 616 (1989)

[85]   S. Bourzeix, M. D. Plimmer, F. Nez, U Julien, and F. Biraben, *Efficient frequency doubling of a continuous wave titanium:sapphire laser in an external enhancement cavity*, Opt. Commun. **99**, 89 (1993)

[86]   K. Kato and E. Takaoka, *Sellmeier and thermo-optic dispersion formulas for KTP*, Appl. Opt. **41**, 5040 (2002)

[87]   R. C. Eckardt, H. Masuda, Y. X. Fan, and R. L. Byer, *Absolute and Relative Nonlinear Optical Coefficients of KDP, KD*P, BaB_2O_4, $LiIO_3$, MgO: $LiNbO_3$, and KTP Measured by Phase-Matched Second-Harmonic Generation*, IEEE J. Quantum Electron. **26**, 922 (1990)

[88]   K. W. DeLong, R. Trebino, and W. E. White, *Simultaneous recovery of two ultrashort laser pulses from a single spectrogram*, J. Opt. Soc. Am. B **12**, 2463 (1995)

[89]   J. H. Seldin and J. R. Fienup, *Iterative blind deconvolution algorithm applied to phase retrieval*, J. Opt. Soc. Am. A **7**, 428 (1990)

[90]   K. W. DeLong and R. Trebino, *Improved ultrashort pulse-retrieval algorithm for frequency-resolved optical gating*, J. Opt. Soc. Am. A **11**, 2429 (1994)

[91]   I. Amat-Roldán, I. G. Cormack, P. Loza-Alvarez, and D. Artigas, *Starch-based second-harmonic-generated collinear frequency-resolved optical gating pulse characterization at the focal plane of a high-numerical-aperture lens*, Opt. Lett. **29**, 2282 (2004)

[92]   R. Fanciulli, L. Willmes, J. Savolainen, P. van der Walle, T. Bäck, and J. L. Herek, *Evolution Strategies for Laser Pulse Compression*, 8th International Conference on Artificial Evolution, **4926** (2007)

[93]   D. Zeidler, T. Hornung, D. Proch, and M. Motzkus, *Adaptive compression of tunable pulses froma non-collinear-type OPA to below 16 fs by feedback-controlled pulse shaping*, Appl. Phys. B **70**, S125 (2000)

[94]   H. P. Schwefel, *Evolution and Optimum Seeking* (Wiley, ISBN: 978-0471571483, 1995)

[95]   T. Naganuma and Y. Kagawa, *Effect of particle size on light transmittance of glass particle dispersed epoxy matrix optical composites*, Acta mater. **47**, 4321 (1999)

[96]   C. Blum, V. Subramaniam, F. Schleifenbaum, F. Stracke, B. Angres, A. Terskikh, and A. J. Meixner, *Single molecule fluorescence spectroscopy of mutants of the Discosoma red fluorescent protein DsRed* , Chem. Phys. Lett., **362**, 355, (2002)

[97]   J. Cheng, L. D. Book, and X. S. Xie, *Polarization coherent anti-Stokes Raman scattering microscopy*, Opt. Lett. **26**, 1341 (2001)

[98]   T. A. H. M. Scholten, G. W. Lucassen, E. Koelewijn, F. F. M. De Mul, and J. Greve, *Non-resonant background suppression in preresonance CARS spectra of flavin adenine dinucleotide: Demonstration of a background suppression technique using phase mismatching and comparison with the polarization-sensitive CARS technique*, J. Raman Spectrosc. **20**, 503 (1989)

[99]   R. Porter, F. Shan, and T. Guo, *Coherent anti-Stokes Raman scattering microscopy with spectrally tailored ultrafast pulses*, Rev. Sci. Instrum. **76**, 043108 (2005)

[100]   D. Oron, N. Dudovich, D. Yelin, and Y. Silberberg, *Narrow-Band Coherent Anti-Stokes Raman Signals from Broad-Band Pulses*, Phys. Rev. Lett. **88**, 063004 (2002)

[101]   K. P. Knutsen, J. C. Johnson, A. E. Miller, P. B. Petersne, and R. J. Saykally, *High spectral resolution multiplex CARS spectroscopy using chirped pulses*, Chem. Phys. Lett. **387**, 436 (2004)

[102]   H.-S Tang and W. S. Warren, *Mid infrared pulse shaping by optical parametric amplification and its application to optical free induction decay measurement*, Opt. Express **11**, 1021 (2003)

[103]   D. Oron, N. Dudovich, and Y. Silberberg, *All-optical processing in coherent nonlinear spectroscopy*, Phys. Rev. A **70**, 023415 (2004)

[104]   D. J. Jones, E. O. Potma, J. Cheng, B. Burfeindt, Y. Pang, J. Ye, and X. S. Xie, *Synchronization of two passively mode-locked, picosecond lasers within 20 fs for coherent anti-Stokes Raman scattering microscopy*, Rev. Sci. Instrum. **73**, 2843 (2002)

[105]   L. Ma, R. K. Shelton, H. C. Kapteyn, M. M. Murnane, and J. Ye, *Sub-10-femtosecond active synchronization of two passively mode-locked Ti:sapphire oscillators*, Phys. Rev. A. **64**, 021802 (2001)

[106]   H. Yamagishi, Y. Suzuki, and A. Hiraide, *Precise Measurement of Photodiode Spectral Responses Using the Calorimetric Method*, IEEE Tr. Instrum. Meas. **38**, 579 (1989)

[107]   L. Werner, R. Friedrich, U. Johannsen, and A. Steiger, *Precise scale of spectral responsivity for InGaAs detectors based on a cryogenic radiometer and several laser sources*, Metrologia **37**, 523 (2000)

[108]   M. Schmitt, G. Knopp, A. Materny, and W. Kiefer, *Femtosecond time-resolved coherent anti-Stokes Raman scattering for the simultaneous study of ultrafast ground and excited state dynamics: iodine vapour*, Chem. Phys. Lett. **270**, 9 (1997)

[109]   R. K. Shelton, S. M. Foreman, L. Ma, J. L. Hall, H. C. Kapteyn, M. Murnane, M. Notcutt, and J. Ye, *Subfemtosecond timing jitter between two independent, actively synchronized, mode-locked lasers*, Opt. Lett. **27**, 312 (2002)

[110]   T. R. Schibli, J. Kim, O. Kuzucu, J. T. Gopinath, S. N. Tandon, G. S. Petrich, L. A. Kolodziejski, J. G. Fujimoto, E. P. Ippen, and F. X. Kaertner, *Attosecond active synchronization of passively mode-locked lasers by balanced cross correlation*, Opt. Lett. **28**, 947 (2003)

[111]   R. W. Boyd, *Nonlinear Optics*, 2th edition (Academic Press, ISBN: 978-0123694706, 2003)

[112]   J. Workman Jr., *Handbook of organic compounds: NIR, IR, Raman and UV-Vis spectra featuring polymers and surfaces*, (Academic Press, ISBN: 978-0127635606, 2001)

[113]   H. A. Willes, V. J. I. Zichy, and P. J. Hendra, *The Laser-Raman and Infra-red Spectra of Poly(Methyl Methacrylate)*, Polymer **10**, 737 (1969)

[114]   M. Gu and X. S. Gan, *Effect of the detector size and the fluorescence wavelength on the resolution of three- and two-photon confocal microscopy*, Bioimaging **4**, 129 (1996)